SISSA   **ISAS**

Modelling structure, phase transition, and vibrational spectroscopy of silica at extreme conditions

Thesis submitted for the degree of

Doctor Philosophiœ

Candidate:

Yunfeng Liang

Supervisor:

Prof. Sandro Scandolo

October 2007

Contents

Introduction

Understanding the behavior of materials subjected to elevated pressures of the order of 10^4 bar or 1 GPa has been the subject of considerable interests in the last decades [1]. High-pressure synthesis on an industrial scale is applied to obtain synthetic diamonds and cubic boron nitride (c-BN), which are the superhard abrasives of choice for cutting and shaping hard metals and ceramics. Recently, high-pressure sciences have undergone a renaissance with new techniques and instrumentation. For example, superconducting behaviour was previously known for only a few elements and compounds. Under high-pressure conditions, the "superconducting periodic table" now extends to all classes of the elements, including condensed rare gases, and ionic compounds such as CsI. Another surprising result is the newly discovered solid-state chemistry of the novel compounds such as nitrides and light-element gas molecules such as CO_2, N_2, O_2 and N_2O, which react to give polymerized covalently bonded or ionic mineral structures under conditions of high pressure and temperature. On the other hand, there are continuous interests in the properties of minerals found in the crust, proposed for mantle and the core of the Earth.

Silica is ubiquitous in the Earth's crust and mantle with many crystalline and amorphous forms or as a fundamental building block of many rock-forming minerals. With the invention of high-pressure apparatus (to 10 GPa) by P. W. Bridgman (Nobel prize 1946) and the introduction of the Mao-Bell diamond anvil cell (to 300 GPa) [2] and the the brightness of Sychrotron radiation, lots of experimental data have been collected about silica, which have in turn generated a number of open problems. Under pressure and room temperature, quartz and cristobalite are reported to transform into metastable phases, instead of the thermodynamically stable coesite and stishovite phases. Some of them, such as quartz-II and phase X-I are still unknown after 20 years [3,4]. Phase X-II has been assigned as isostructure to α-PbO_2 [5,6], however, previous simulations couldn't reproduce the experiments. The pathway is therefore unclear so far. There are a number of experiments, which reported quartz and coesite to become amorphous under pressure [7], a phenomenology first observed in ice [8]. The microscopic description of such pressure-induced amorphization is still debated [9,10].

Problem of predicting, a priori, the structure that a solid will adopt is even today (with powerful computer), extremely difficult. Faced with this problem one looks for approximate but general principles that serve both as aids to rationalizing crystal structures and as guides to predicting the structures of new compounds.

Silica glass is a prototypical example of a network-forming disordered material like water. The geometrical, topological, and coordination changes resulting from the application of pressure provide an ideal testing ground for atomistic models. Contrary to ordinary solids, which are normally known to harden by compression, the compressibility of silica glass has a maximum at about 2-4 GPa [10-15], and its mechanical strength shows a minimum around 10 GPa [16]. At this pressure, the compression of silica glass undergoes a change from purely elastic to plastic, and samples recovered from above 10 GPa are found to be permanently densified [17-22]. As first noted by Roy and Cohen [23,24], recent in situ measurements have confirmed that densification can also take place at lower pressures provided the glass is annealed to several hundred degrees [22,25-27]. There are plenty of theoretical studies though, no unified model exist for all above phenomena.

In spite of theoretical and computational advances, including the availability of increasingly efficient first-principles codes, addressing the above problems is still out of reach for state-of-art first principles methods due to the size and time scales. Classical molecular dynamics is of great help to have better statistics due to possibility of simulating the larger sizes and time scales. However, the results will be dependent on the quality of the force field. To combine classical molecular dynamics and first-principles calculations is therefore becoming a very important branch of computational physics and material sciences. One efficient way is to construct accurate and transferable potentials for atomic interactions from ab initio by so called "force matching method", initially developed for metals by F. Ercolessi and colleagues at SISSA [28]. My starting point is the availability of a polarizable potential for silica developed in our group [29]. Even though the potential has already been shown to yield better results than all the other potentials to which it has been compared so far, it is not obvious a priori that its validity can be extended to address all the above problems in silica, so part of my thesis focuses on the testing the reliability of the potential.

In this thesis, I'll use the silica potential [29] to understand:

1). What is phase X-I of silica? How does phase X-II (a-PbO$_2$-like phase) form?

2). What is quartz-II? What is the mechanism of the quartz pressure-induced amorphization and of the appearance of post-quartz crystalline phases?

3). What is the reason for yield strength minimum, compressibility maximum and densification in compressed silica glass?

4). Is it possible to use the polarizable potential to extract infrared and Raman spectra?

The outline of my thesis is the following: In Chapter 1, I present more details related to the motivation for studying silica. In Chapter 2, I mainly discuss the force matching method which has been used to construct the force field, and some methology. In Chapter 3, I show how the performance of the potential and how it can be used to calculate infrared and Raman spectra, focusing on the the calcuation of the spectra for high-temperature phase. Based on the calculated specta and the structural analysis, more profound understanding of the silica high-temperature phase is given. I will show in Chapters 4 and 5, pressure–induced changes in oxygen packing in quartz and cristobalite can be understood based on well-known transition paths for close-packing lattices. I will present in Chapter 6, a microscopic picture of the compression mechanisms of silica glass. In order to advance the understanding of pressure-induced amorphization, in Chapter 7 I also studied one example of the silica clathrate (type I) under pressure. I will then summarise the main results of my work in Chapter 8.

Chapter 1

Why Study Silica?

1.1 Silica in Earth and Material Sciences

Silica is one of the primary components of Earth. Based on the chondritic model, SiO_2 makes up 50 weight percent of Earth bulk [30]. Although it is generally accepted that SiO_2 component of Earth's lower mantle occurs as $(MgFe)SiO_3$-perovskite, experimental evidence for the breakdown of perovskite at about 80 GPa [31,32] suggests that free silica may exist in the lower mantle [30,33,34]. Silica is also of great technological importance in both its crystalline and glassy forms [35], such as frequency control by crystalline quartz, microelectronics on glass surface/interface, chemical processing and corrosion control in the confinement by the cages of clathrasis (zeolite) and versatile ceramics (hard-toughness). From the point of view of condensed matter physics [36,37], silica glass is an ideal analogue of network forming materials. The structure of silica at moderate pressures consists of rigid tetrahedral building blocks connected at their corners by soft "floppy" joints. Understanding of the response to pressure of such structures is of general interests due to the possible polyamorphism (first-order transition between two kinds of glasses) [9] and due to the anomalies [10-27] with respect to all the other solids found by experiments. The low-pressure crystalline phases under pressure presents an important system for investigating pressure-induced amorphization [7], and the existence of metastable phases and the transition mechanisms between them (reconstructive or displacive) [3,4,38,39].

1.2 Phase Diagram

Silica exists in many different polymorphs, quartz, cristobalite, tridymite, coesite, stishovite, $CaCl_2$-like form, α-PbO_2-like form and pyrite form (Fig.1.1)[40], each one thermodynamically stable in a different region of the phase diagram. The most stable phase of silica at ambient condition is α-quartz, which belongs to the class of silica structures with corner-sharing SiO_4 tetrahedral. Quartz is traditionally considered a nontrivial benchmark system for examining the accuracy of the theory [41,42]. Cristobalite belongs to the same class of structures, but has smaller

5

density, different symmetry, and a different medium- and long-range arrangement of the tetrahedral. Stishovite (rutile structure) and the $CaCl_2$-like phase of silica are also of considerable interest, not only because of their edge-sharing SiO_6 octahedral structures, with Si in six-fold coordination to O, but also because the pressure-induced rutile-to-$CaCl_2$ transitions is a typical example of a soft-mode-induced Laudau-type transition, as first found by Raman spectroscopy [43] and later confirmed by x-ray diffraction [44]. Since the discovery of stishovite [45], there have been significant progresses in the discovering of denser phases that are stable at higher pressure, for example, pyrite structure has been recently identified under pressures exceeding 200 GPa [26]. $CaCl_2$ phase [43,44] and α-PbO_2-like phase [46] are related to the properties of the silica under deep mantle conditions. Such a variety of phases offer an interesting stage for theoretical models. Moreover, despite decades of extensive work, a number of issues related to different aspects of silica phase diagram are still unclear. In this chapter, I will list several open issues covering both the low- and high-pressure regions of the phase diagram.
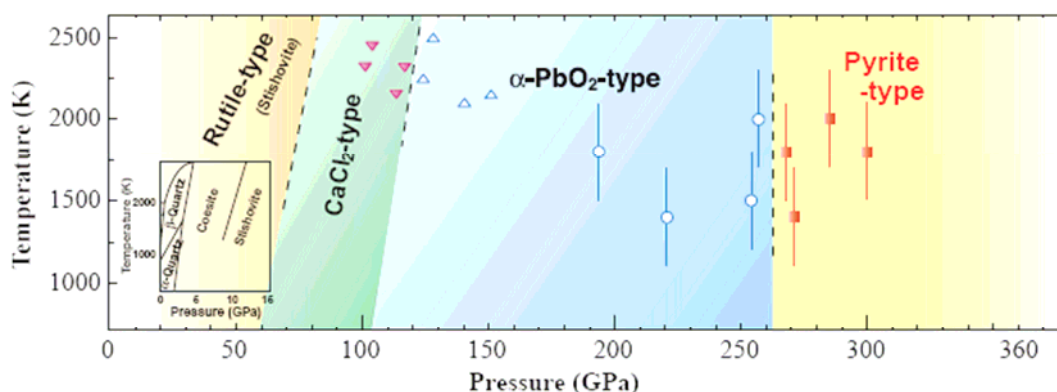
Fig.1.1 Phase diagram of silica after Kuwayama et al [40].

1.2.1 IR and Raman Spectra

I will start with the list by describing a methodological problem, the theoretical determination of the Raman and IR spectra of the low-pressure tetrahedral phases, which has so far hampered the theoretical investigation of the spectra particularly at high temperature. Besides their obvious relevance "per se", understanding the Raman and IR spectra of both quartz and cristobalite might set a basis for the interpretation of vibrational spectra in silica glass, the disordered counterpart of

the class of corner-sharing tetrahedral networks. By increasing temperature, quartz and cristobalite transform from a low temperature α phase, where the harmonic approximation is believed to be valid, into a β phase, whose dynamics is believed to be dominated by dynamical disorder, and hence to be completely anharmonic. Raman and IR experiments on quartz and cristobalite as a function of temperature show that the α -β transition is characterized by the sudden disappearance, in the high-temperature β phases, of some of the peaks of the low-temperature α phases [47-50]. In quartz, the Raman modes present at 128 and 207 cm^{-1} in the α phase merge and weaken, and only one major peak remains in the spectrum of β-quartz around 464 cm^{-1}, slightly left-shifted with respect to the same peak in α-quartz [48]. For cristobalite, all the strong Raman bands at 416, 230 cm^{-1} and 114 cm^{-1} disappear in the transition of α–cristobalite to β-cristobalite [49,50]. Theory has been unable so far to describe the IR and Raman spectra of the high temperature β phases, but the availability of accurate polarizable potentials brings this goal under reach.

1.2.2 Possible Post Stishovite Phases

The relative stability of $CaCl_2$ phase and α-PbO_2-like phase under higher pressure is still debated, typically because it is dependent on the starting materials [51]. Nevertheless, α-PbO_2-like phase is stable according to some experiments [46,52] and first-principles calculations [53-56], and overall the difference of the enthalpy is small [54]. The fact that α-PbO_2-like phase can be obtained at room temperature from cristobalite is one of the most interesting and debated topics [5,6,57-60], particularly because the Martian meteorite Shergotty, a shocked achondrite to ~29-45GPa, contains a dense orthorhombic SiO_2 phase with α-PbO_2 structure [33,34], and also because previous calculations didn't reproduce α-PbO_2-like phase as a resulting octahedral phase, starting from cristobalite [61-64].

1.3 Compressed Silica Glass

It is very interesting to study the structure of silica glass upon slight compression (between 0 and 10 GPa, approximately). Here there are a number of puzzling observations that await theoretical interpretation. The first observation is that SiO_2 glass is very compressible [65], much more compressible than quartz, with respect to which, glass becomes finally denser at about 12

GPa [7]. The reason for this has been highly debated. Meade et al [66] believe that compression is achieved by reducing the Si-O-Si angle, i.e. by tilting the tetrahedra, without any bond breaking and reforming. In ref. [65] a different mechanism is proposed whereby compression is achieved by changing the topology of the network (ring distribution). Changes in coordination (silicon increases its average coordination) cannot be ruled out either, as it is the case in liquid silica [67].
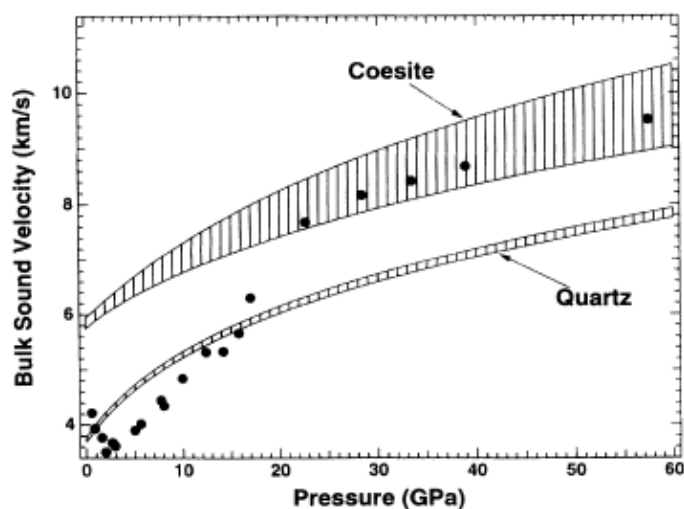
Fig.1.2 Bulk sound velocity obtained according to the measurement of the Brillouin scattering after Zha et al [14].

In connection with this, SiO_2 glass displays a very anomalous compressiblity versus pressure [11-15], with a maximum (minimum in the bulk modulus) around 2-4 GPa (Fig.1.2). This is typical of an underlying phase transition, or crossover, between two states, as argued for the case of GeO_2 glass [68]. Indeed, evidence for a first order phase transition in the glass has been proposed theoretically [69] and experimentally [70], although both results have been seriously questioned [22]. Notice that, at variance with GeO_2, where differences exist between the compressibility measured statically (derivative of the P(V) curve) and dynamically (measuring the sound velocity), due to the long time dynamics of the structural rearrangements when pressure is changed (see Ref [68] for an instructive discussion on this), the anomaly is present, in SiO_2, also in the sound velocity [14] indicating that silica glass is long-lived metastable state at each pressure. This implies that the acoustic branch is indeed becoming softer with pressure in SiO_2, up to about
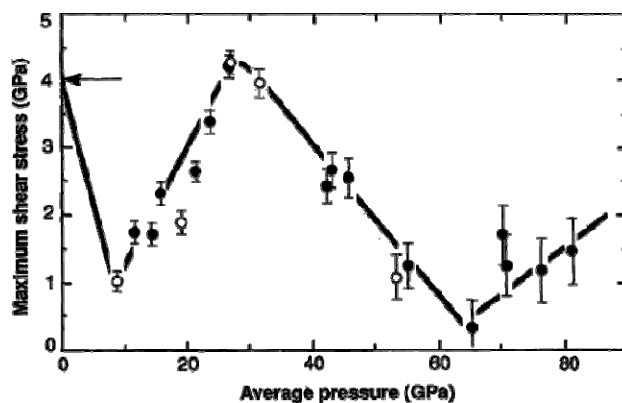
Fig. 1.3 The yield strength at different pressure after Meade & Jeanloz [16].
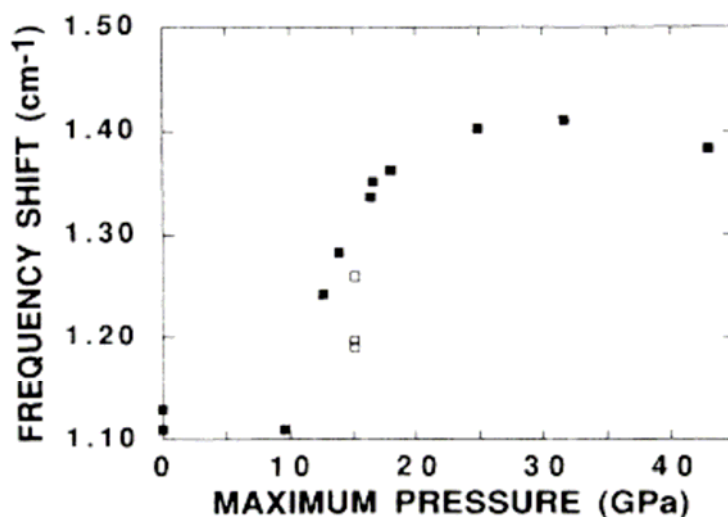
Fig. 1.4 The densification (indicated by the Brillouin frequency shift) for different subjected peak pressure after Polian & Grimsditch [19].

5 GPa, which is a very unusual phenomenon. In connection with such a "softening", the rheology of compressed glass is also becoming weaker. The yield strength decreases [16] and has minimum about 10 GPa (Fig.1.3). The crystal growth rates increase dramatically at higher temperature as well [70].

Notice that much has been discussed about the permanent densification of glass when compressed above 10 GPa, i.e. the recovered sample is denser than the starting one (Fig.1.4), however most of the models proposed so far for densified glass obtained from cold decompression at room temperature [71-74], contain sizable amounts of coordination defects, which are also not

seen in experiments [20, 75]. On the other hand, five-fold defects are known to be responsible for the diffusivity maximum in silicate melts [76,77], whether it exists and yields the anomalies in glass is still unknown.

The problem of studying compressed silica glass by simulations is complicated by the well-known difficulty of generating a good starting configuration at zero pressure. Generally speaking, there are two kinds of methods to prepare a model for study: one is from such as WWW model [78] as ideated for silicon glass; another one is more natural as it is prepared quenching from liquid [79]. The former is useful, however is limited, particularly we find it to contain no three member ring in the final configuration therefore the spectra generated from such model is generally in poor agreement with experiments, and it is not clear how far it is comparing with the natural glass. The second one will be perfect in principle, however the quality of the glass will be related to the quenching rate [79]. We will start our simulation based on the knowledge above and obtain an "ideal" glass at least from the view of the density (saturated with quenching rate) and then proceed with the study of the anomalies presented above.

1.4 Metastable Phases

1.4.1 Phase X-I and Phase X-II by Compressing Cristobalite

Experiments at low pressures show that a first-order transition from α-cristobalite to cristobalite-II (the space group symmetry $P2_1/c$) take place at around 2 GPa [80-85]. Dove et al. reproduced cristobalite-II from ideal cubic cristobalite [83]. So far cristobalite-II couldn't be reached directly by rigid unit mode (RUM) model as well [83,86] due to high-energy barrier. At pressure above 10 GPa, i.e. well within the stability domain of stishovite, cristobalite transforms into a new phase (phase X-I), and above 30 GPa a second new phase (phase X-II) is formed, both of which are crystalline [3] and metastable. As mentioned earlier in this chapter, the phase X-II has been established as α-PbO_2-like phase [5,6]. The finding is very interesting, because so far no theory could reproduce this phase starting from cristobalite [61-64]. Phase X-I remains mysterious as the diffraction peaks are not enough to extract the crystalline structure and earlier theories yield a different phase (CmCm) with 50% of 6-coordinated silicon [63], which is in contrast to the Raman and infrared spectra. Very recently, Huang et al [62], by using a combination of classical and first-principle simulations, have proposed hp-cristobalite with oxygen (hexagonal) close

packed lattice, which allows to reconcile the evidence, from X-ray diffraction, of a low compressibility for phase XI [3], with that of tetrahedral order within the same phase, as inferred from infrared and Raman spectroscopy [37,84,85]. However, hp-cristobalite is reported to transform, in the second step of the process described in Ref. [62], into stishovite, which has never been observed in experiments starting from cristobalite and phase X-I so far. Gratz et al. reported that amorphization could be obtained by compressing cristobalite particles (~30 nm) around 23-28 GPa [87], i.e. in the regime of phase X-I. However, the physical behavior under nano scales is beyond the scope of this study.

We will focus on the description of structural information of phase X-I and show how it is possible to obtain phase X-II from phase X-I.
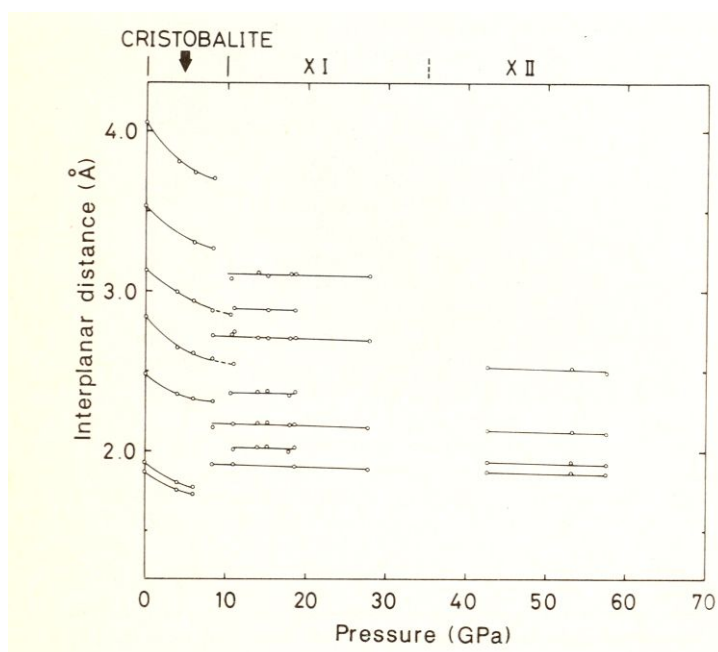
Fig. 1.5 Pressure dependence of interplanar spacings of cristobalite after Tsuchida and Yagi [3].

1.4.2 Quartz-II, P2$_1$/c (Z=6) and Pressure-induced Amorphization

A number of experimental studies have reported the pressure-induced amorphization in quartz and coesite at around ~30GPa [7]. Different mechanisms have been proposed to explain amorphization, including pressure induced melting. Theoretical studies have provided a deeper

understanding of metastable phase transition in quartz (and coesite as well), mainly from the view of the dynamic instability [88,89] or elastic instability [90,91]. The mechanism is still debated also because new experiments have shown that before or at amorphization there is evidence of new crystalline phase named quartz II [4, 39]. Experiences have also yielded evidence for additional phases above the amorphization pressure [39, 92]. Among them, the $P2_1/c$ (Z=6) is a denser phase similar to stishovite and has been clearly resolved by Haines et al using helium pressure medium [39]. Rationalizing such a complex behavior requires microscopic models for quartz-II, for amorphous phase, for the transition mechanisms (to at least three different phases), which have not been extracted from experiment yet.
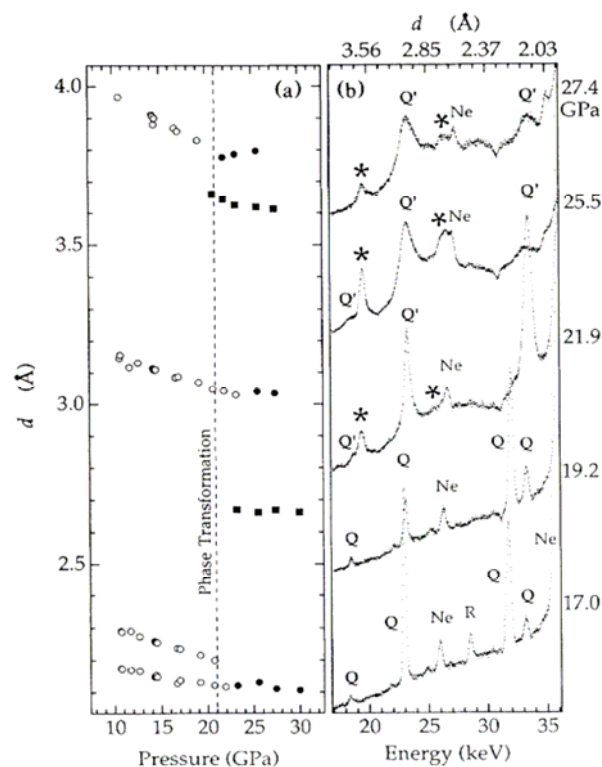
Fig. 1.6 The X-Ray diffraction pattern and the interpanar spacings as a function of pressure. The evidence for quartz-II is the convergence of the (110) and (102) peaks as discussed by Kingma et al [23,79].

Crystalline-amorphous transitions have been also documented in melanophlogite (type I clathrate) and dodecasil (type II clathrate) very recently, primarily through a broadening and drop in intensity of the X-ray diffraction lines [93-95]. Unlike quartz and coesite, the starting crystal (melanophlogite) is already less dense than glass, and with similiar Gibbs free energy at 0GPa,

which explain its lower amorphization pressure of ~ 8GPa [94]. The microscopic mechanisms have not been extracted from experiment however.

1.4.3 Effect of Non-hydrostaticity

Many transformations in minerals (such as quartz [7,39] and cristobalite [57, 96]) are sensitive to deviatoric or non-hydrostatic stresses, so it is of prime importance to consider the nature of pressure conditions generated by different types of pressure-transmitting media. Purely hydrostatic conditions prevail if the pressure medium, employed to compress the sample, remains liquid or gaseous under pressure. This is the case for 4:1 methanol:ethanol mixture up to 10 GPa and for the 16:3:1 methanol:ethanol:water mixture up to 15 GPa [97]. Above these pressures vitrification of mixtures occurs and non-hydrostatic conditions prevail, with typical pressure gradients on the order of 1-2 GPa over a 200-μm hole at 20-30 GPa. Helium and hydrogen remain the most hydrostatic and can be used into Mbar range, however, recent experiments show that helium and hydrogen can be absorbed in the materials and possibly change the properties of the sample [95]. As it is hard to achieve purely hydrostatic conditions above 20 GPa, it is very important from theoretical view to study the resulting phases at different stress conditions, in the hope that if the stress conditions in experiments are known, the measurements together with the theory can provide important additional information on material behavior. Characterizing the state of stress in a sample is possible by vibrational spectroscopy. For example, the pressure dependence of Raman mode in ^{13}C diamond has been used for calibration in high P-T experiments [97].

Chapter 2

Theoretical Methods

In spite of theoretical and computational advances, including the availability of increasingly efficient first-principles codes, most of the physical phenomena described in this thesis deal with time and size scales that are still out of reach for state-of-art first principles methods. It is thus desirable to construct accurate and transferable potentials for atomic interactions. The force matching method, initially developed by F. Ercolessi and colleagues at SISSA [28], which consists in parameterizing effective potentials from ab initio data, among all the other methods, is very appealing, due to its "first-principles" character (except for the functional form, no other information is from experiments). The many-body character of the atomic interactions is generally included in the most advanced force fields. The polarizable potential for silica developed by Tangney and Scandolo [29] is presented in this chapter. We start the introduction with a brief description of the first principles methods used to construct the TS potential. Some relevant theoretical techniques used throughout this thesis are also presented in the end of this chapter.

2.1 Quantum Mechanics Modeling

Molecular dynamics (MD) is a widely used technique for the simulation of a system of atomic nuclei (and electrons) at a microscopic level. In particular, the method ideated by Car and Parrinello [98] made feasible to perform MD simulations with a full quantum description of electrons within Density Functional Theory (DFT) [99]. Explicitly treating the electrons means that, in principle, one does not make assumptions about the bonding of the system and this allows surprises to occur. Spontaneous changes in bonding can take place without loss of accuracy, which means that one can simulate changes of phase with more confidence. Ab initio molecular dynamics (AIMD) can also allow one to model chemical reactions. This is something that effective force fields are unable to do because, by definition, chemical reactions involve changes in the bonding and when they occur it is the electrons, which play the dominant role. Unless the dependence of electrons on ionic positions is explicitly calculated, the reaction cannot be modeled.

2.1.1 Car-Parrinello Molecular Dynamics (CPMD) in NVE Ensemble

The Car-Parrinello (CP) method [98] approximates the exact adiabatic evolution of the electronic ground state during the ionic dynamics, by evolving electronic and ionic degrees of freedom according to the classical Lagrangian:

$$L_{CP} = \sum_i \frac{\mu_i}{2} \langle \dot{\psi_i} \dot{\psi_i} \rangle + \tfrac{1}{2} \sum_I M_I \dot{R}^2 - V[\{\psi_i\}, \{R_I\}] \tag{2.1}$$

the trajectories for the ionic and electronic degrees of freedom are generated through the coupled set of equations of motion

$$M_I \ddot{R}_{I,\alpha} = -\frac{\partial V[\{\psi_i\}, \{R_I\}]}{\partial R_{I,\alpha}}$$

$$\mu | \ddot{\psi_i} \rangle = -\frac{\delta V[\{\psi_i\}, \{R_I\}]}{\delta \langle \psi_i |}$$

where M_I and R_I are the mass and position of atom I, respectively. $\psi_i \rangle$ are the Kohn-Sham orbital which are allowed to evolve as classical degrees of freedom with parameters μ_i, driven to the ground state by the derivatives of $V[\{\psi_i\}, \{R_I\}]$, a functional of the electronic charge density according to Kohn-Sham theory.

Kohn-Sham DFT [99] allows the calculations of forces acting on the atoms according to Hellmann-Feynman theorem

$$F_{I,\alpha} = -\frac{\partial \langle \psi_i | V[\{\psi_i\}, \{R_I\}] | \psi_i \rangle}{\partial R_{I,\alpha}} = -\langle \psi_i | \frac{\partial V[\{\psi_i\}, \{R_I\}]}{\partial R_{I,\alpha}} | \psi_i \rangle \tag{2.2}$$

In the CP method, the forces are calculated on the instantaneous wave functions, which, in practice, closely approximate the exact adiabatic ones.

2.1.2 The Internal Stress Tensor in DFT

In principle, Kohn-Sham DFT [99] allows Hellmann-Feynman theorem works for the calculations of internal stress tensor acting on the cell

$$\pi_{\alpha,\beta} = -\frac{1}{\Omega} \frac{\partial \langle \psi_i \mid V[\{\psi_i\},\{S_I\},\{h_{\alpha,\beta}\}] \mid \psi_i \rangle}{\partial h_{\alpha,\beta}} = -\frac{1}{\Omega} \langle \psi_i \mid \frac{\partial V[\{\psi_i\},\{S_I\},\{h_{\alpha,\beta}\}]}{\partial h_{\alpha,\beta}} \mid \psi_i \rangle \quad (2.3)$$

2.2 Force Matching Method

In a molecular dynamics simulation the important quantities are the forces on each atom, and if one is performing simulations at constant pressure, the stress on the simulation cell. Ercolessi and Adams [28] have introduced the idea of fitting the parameters of an "empirical" force field to reproduce ab initio forces as well as possible. Laio et al. [91,92] were interested in simulating systems (iron) under high pressure and so have extended the method slightly by trying fit also the calculated stress. In the fitting potential for complex system such as silica (with many polymorphs), Tangney et al [86, 93, 94] also include in the function to be optimized, the energy differences between different configurations. As long as we are not interested in the chemical reactions or magnetism properties or other subtle changes in the electronic properties, the method should be valid. Details have been given in Tangey's PhD thesis [93], some necessary content is repeated here for completeness.

2.2.1 Why Effective Potentials in the Era of Ab Initio Calculations?

The computational expense involved in AIMD means that for most of the problems in which we are interested, an alternative solution is required. We would like to find a compromise between the accuracy in static calculations and the quality of thermodynamic sampling, thus can be computed with more confidence than has been done in the past. The approach was taken to finding this compromise was to look for force fields with functional forms (NOT a function), which capture phenomenologically more of the dynamical electronic effects, which contribute to interionic forces and which are therefore capable of providing more accuracy [29, 103-116]. The compromise lies in the fact that this capacity for improved accuracy is generally at the expense of computational efficiency. The improved accuracy was achieved with a given functional form by using data from density functional theory simulations in a general and well-controlled parametrization procedure. An obvious advantage is that the calculations by effective potential are much cheaper than AIMD, and therefore permit larger system sizes and run lengths, for example, the liquid silica at lower pressure and glass is highly viscous, as shown in Fig.2.1, AIMD (within
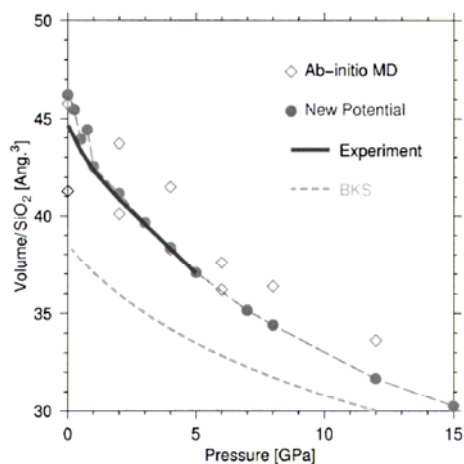
Fig.2.1 Equation of state of liquid silica [29] for the new potential compared to experiment, ab initio simulations and classical simulations using the BKS potential. Time and size constraints and the very high viscosity of liquid silica at low pressures mean that the ab initio system cannot diffuse enough to give meaningful averages of thermodynamic properties. Different initial configurations account for the different abinitio volumes at the same pressure.

short time scale and small size) can only give some scattered data at lower pressure [29], and only become meaningful [67] after the combination with the calculations by efficient potential. A number of properties, of viscous melts/glasses, interfaces or grain boundaries, solubility (with different percentage of components), fracture, defects extended in crystals, can only be addressed by classical potential so far. For example, the simulated silica glass quenching from liquid depends on the quenching rate [79] and convergence is reached for quenching rate, which are not feasible with AIMD in the present ages, however we can do it by classical MD. More examples will be found from our study: the resulting crystal structures are dependent on the compression rate (See in Chapters 4 and 5).

2.2.2 Parametrizing from Ab-initio Data

Given a form for the interatomic force-field, which depends on a set of parameters $\{\eta\}$, the following function was minimized:

$$\Gamma(\{\eta\}) = \omega_f \Delta F + \omega_S \Delta S + \omega_E \Delta E \tag{2.4}$$

with respect to the parameters $\{\eta\}$ where

$$\Delta F = \frac{\sqrt{\sum_{k=1}^{n_c} \sum_{I=1}^{N} \sum_{\alpha} |F_{cl,I}^{\alpha}(\{\eta\}) - F_{ai,I}^{\alpha}|^2}}{\sqrt{\sum_{k=1}^{n_c} \sum_{I=1}^{N} \sum_{\alpha} (F_{ai,I}^{\alpha})^2}}$$

$$\Delta S = \frac{\sqrt{\sum_{k=1}^{n_c} \sum |S_{cl}^{\alpha\beta}(\{\eta\}) - S_{ai}^{\alpha\beta}|^2}}{3B\sqrt{n_c}}$$

$$\Delta E = \frac{\sqrt{\sum_{k,l}^{n_c} ((U_{cl}^{k} - U_{cl}^{l}) - (U_{ai}^{k} - U_{ai}^{l}))^2}}{\sqrt{\sum_{k,l}^{n_c} (U_{ai}^{k} - U_{ai}^{l})^2}}$$

Here $F_{cl,I}^{\alpha}$ is the α-th component of the force on atom I as calculated with classical potential, $F_{ai,I}^{\alpha}$ is the force component as calculated ab initio, $S_{cl}^{\alpha\beta}$ is the stress tensor component as calculated with classical potential and $S_{cl}^{\alpha\beta}$ is the stress tensor component as calculated ab initio, B is the bulk modulus, U_{cl}^{k} and U_{cl}^{k} are the potential energy of configuration k as
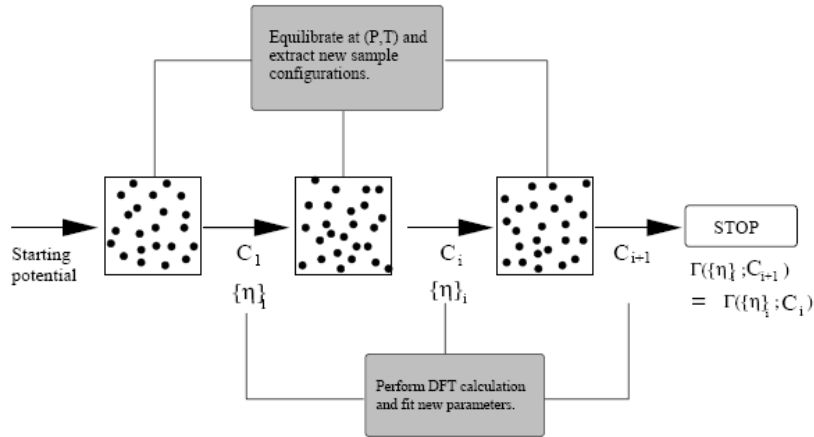
Fig.2.2 The sketch of force matching method [103]

calculated with classical potential and ab initio respectively, n_c is the number of the configurations for which the potential were fitted. The quantity $\omega_f > \omega_S > \omega_E$ were chosen to reflect the amount of available data. The final fit was insensitive to the values chosen as long as ω_E was relatively small. n_c was required to be reasonable large, e.g. 10, and another 5

configurations were retained for convergence (see Fig.2.2). Minimization of $\Gamma(\{\eta\})$ with respect to $\{\eta\}$ was performed using a combination of simulated annealing [119] and Powell minimization [120]. A basin in surface defined by $\Gamma(\{\eta\})$ in $\{\eta\}$ space was initially found using simulated annealing and, once found, further minimization was performed using the method Powell.

The requirement to fit also the ab initio stress and energy improved greatly the capability of the fitting routine to find the correct basin of attraction. This is partially because, for a system with many body forces, the stress is not a trivial function of the forces like in the two-body case; partially because, for an AIMD calculation, energy, forces and stresses are anticipated values of different operators with respect to the same ground state. Regarding the differences between quartz and stishovite at ambient conditions, the two structures differ substantially in their bulk modulus and energies, which strongly suggest the fit to the ab initio stress and energy.

2.3 Many-body Interactions of Simple Ionic Systems

The problem of simulating ionic materials has a long history. One of the oldest, and still the most widely used interaction potential for such systems treats the ions as though they are rigid particles which are undistorted by their environment. This is the Born-Mayer pair potential [121],

$$U_{IJ}(R_{IJ}) = \frac{q_I q_J}{R_{IJ}} + B_{IJ} \exp(-\alpha_{IJ} R_{IJ}) - \frac{C_{IJ}}{R_{IJ}^6} - \frac{D_{IJ}}{R_{IJ}^8} \tag{2.5}$$

where U_{IJ} and R_{IJ} is the interaction energy and the distance of particles I and J, respectively. q_I and q_J are charges on the ions and the first term (V^M) of the expression is electrostatic energy (Madelung potential)of the point charges and is generally evaluated by the method of Ewald summation [122]. The second term (V^{rep}) reflects the fact that an isolated electro distribution tails off exponentially and so the repulsion between ions at short range due to the Pauli exclusion principle can be approximated by a constant B_{IJ} times an exponential overlap of ionic charge distributions; the final two terms (V^{pol}) model the ion dispersion interactions which are always

attractive and which represented van der Waals, as a sum of dipole-induced dipole (R_{IJ}^6 term),

dipole-induced quadrupole (R_{IJ}^8 term) and higher order terms which are generally neglected.

This potential form has the advantage that it has a pairwise form and it is quick and easy to

evaluate, so that the relative large system sizes and long times may be simulated with relative ease.

However, it has been recognized for a long time that this form does not contain some of physics

relevant for many real ionic systems. q_I, α_{IJ}, B_{IJ}, C_{IJ} and D_{IJ} are parameters of the model

which may be determined by physical reasoning, empirical considerations or by fitting to data

obtained from ab initio calculations. But once determined, keep it fixed for simulations. The fact

that we can introduce functional (self-consistence) or environment-dependent (such as

coordination) so that those parameters are varied according to the configurations therefore make

the force field become a many body potential [29, 103-116].

2.3.1 Aspherically Compressible Anions

Many systems contain anions, which have an appreciable size relative to interionic distances

and which are not rigid, in the sense they become aspherically distorted and can change their size

in the condensed phase depending on their environments. This, in practice, can be realized by

slightly modifying the second term (V^{rep}) and the total Hamiltonian so that something as B_{IJ} is

variable. Details can be found in the work by Madden's group [108,112] and Tangney's thesis

[103]. Typically, we can write:

$$V^{rep} = \sum_{i\in A, j\in C}[A^{-+}\exp(-a^{-+}\rho^{ij}) + B^{-+}\exp(-b^{-+}\rho^{ij})] + \sum_{i,j\in A}A^{--}\exp(-a^{--}r^{ij}) +$$
$$\sum_{i,j\in C}A^{++}\exp(-a^{++}r^{ij}) + \tag{2.6}$$
$$\sum_{i\in A}\{D[\exp(\beta\delta\sigma^i) + \exp(-\beta\delta\sigma^i)] + [\exp(\xi^2\,|\,\upsilon^i\,|^2) - 1] + [\exp(\xi^2\,|\,\upsilon^i\,|^2) - 1]\}$$

where A and C stand for anion and cation respectively. And

$$\rho^{ij} = r^{ij} - \delta\sigma^i - \delta\sigma^j - S_\alpha^{(1)}(\upsilon_\alpha^i - \upsilon_\alpha^j) - S_{\alpha\beta}^{(2)}(\kappa_{\alpha\beta}^i - \kappa_{\alpha\beta}^j)$$

$$S_\alpha^{(1)} = r_\alpha^{ij}\,/\,r^{ij}$$

$$S_{\alpha\beta}^{(2)} = 3r_\alpha^{ij} r_\beta^{ij} / r^{ij2} - \delta_{\alpha\beta}$$

The first three summations represent short-range repulsions, while the last term represents the energy cost of deforming the charge density of an ion (anion). $\delta\sigma^i$ is variable which characterizes the deviation of the radius of ion i from its default value. v^i is a set of three variables describing the Caresian components of a dipolar deformation. $\kappa_{\alpha\beta}^i$ is a set of five variables describing the quadrupolar distortions.

2.3.2 Charge Transfer Model

Because electrostatics play an essential role in determining the structure and properties, more models about flexible point charges were reported in the past, which are realized by slightly modifying the first term and the total Hamiltonian so that something as q_I is variable. For a certain local configuration (coordination number) [115], the charge of each atom can be evaluated according to

$$q_i = q_i^0 - \sum_{j=1}^{Nc} \delta_{ij}\varepsilon_{ij} \tag{2.7}$$

where q_i^0 is the charge of the isolated atom and $\varepsilon_{ij} = [1 + \exp(b(r_{ij} - r_0))]^{-1}$ is the charge transfer function, which is only related to the distance of the tagged atom pairs.

For a variable local configuration (coordination number), one is refer to QEq method [116], in which the charges are determined by requiring that the chemical potential χ_A be equal on all the atoms, and χ_A is a function of the charges on all of the atoms of the systems

$$\chi_A = \chi_A^0 + \sum_B J_{AB}(R_{AB})q_{AB} \tag{2.8}$$

Where χ_A^0 and J_{AA}^0 correspond physically to the electronegativity and hardness of the atom and are obtained from the valence-averaged atomic ionization potential (IP) and electron affinity (EA) as $\chi_A^0 = (IP_A - EA_A)/2$ and $J_{AA}^0 = (IP_A + EA_A)$. $J_{AB}(R)$ is described as a shielded Coulomb potential for a normalized Slater orbital.

2.3.3 Polarizable Anions

A distorted ion is one with multipole moments, the most important of which is the lowest order or dipole moment. The induction, via electrostatic interactions, or short range Pauli exclusion-type interactions of dipole moments on ions can have a significant effect on the electrostatics of a system. The inclusion of polarizable part make the third (and fourth) part variable according to the configuration. The many body character is achieved by the self-consistence of the induced dipoles on each anion of every configuration. The effective potential for silica developed by Tangney et al. [29] includes the dipole polarization of oxygen ions, in which the induction of dipole moments both by electrostatic forces and the short-range repulsive forces between anion and cation. The short-range contribution to dipole moments is given by

$$p_i^{SR} = \alpha \sum_{j \neq i} \frac{q_j r_{ij}}{r_{ij}^3} f_{ij}(r_{ij}) \tag{2.9}$$

where

$$f_{ij}(r_{ij}) = c \sum_{k=0}^{4} \frac{(br_{ij})^k}{k!} \exp(-br_{ij}) \tag{2.10}$$

α is the polarizability of the dipoles, b and c are parameters of the model. The dipoles on each ion are found self-consistently at each time step (of MD) by iterating to self-consistency the equation

$$p_i^n = \alpha E(r_i; \{p_j^{n-1}\}_{j=1,N}, \{r_j\}_{j=1,N}) + p_i^{SR} \tag{2.11}$$

where the dipole moment on ion i, p_i depends on the electric field $E(r_i)$ at position r_i which in turn depends on the positions and dipole moments of all the other ions. At each MD step, the iteration begins using initial electric field strengths $\{E(r_j)\}_{j=1,N}$ which have been extrapolated from their values at the previous three MD time steps. The inclusion of polarizability to classical potential is considered "to be the single most significant development in the next generation of force fields for bio-molecular simulations"[123] and "as one of the most important and urgent improvements to be implemented in modern empirical potential models" [124].

2.3.4 Polarizability Variable

This is, however, even second order with respect to the total Hamiltonian (based on Item C). The potential allows the polarizability variable [112] according to the instaneous ionic radii ($r_0 + \delta_i$) and the Madelung potential (V_i^M),

$$\alpha_i = \alpha_0[\exp(\alpha_\delta \delta_i) + \exp(\alpha_V V_i^M)]$$ (2.12)

so that that anions of larger radii or under the action of a less intense Madelung potential have larger polarizaibility. More recently, Heaton et al. makes the calculation on individual ionic polarizability possible is a further development.

2.4 The Potential of Silica

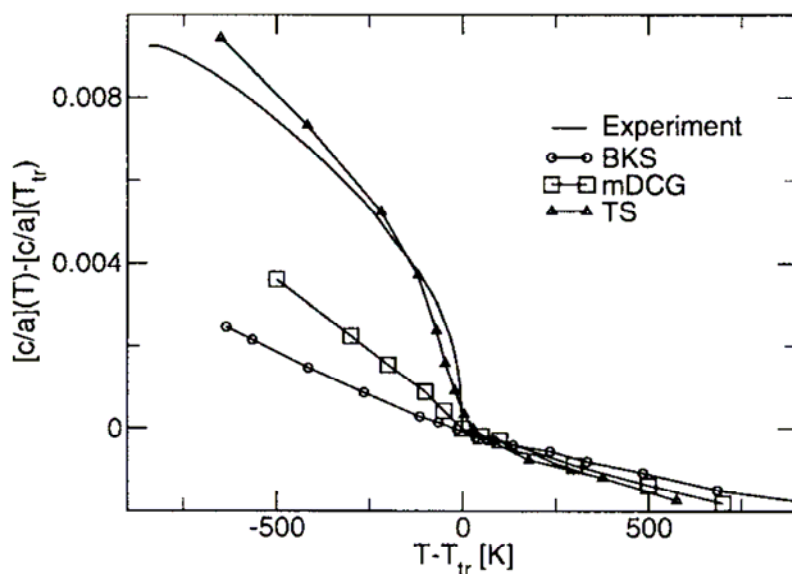The quest for a better potential for silica polymorphs has a long history, which started with

Fig.2.3 Temperature dependence of c/a ratio at α-β transition of quartz [129]

observation that an effective empirical pair potential could describe the relevant structural and dynamical features of silica liquid and glass [73]. Explicit inclusion of covalency in Si-O bonds was achieved by adding three body contributions [115,125]. The TTAM pair potential [126] was regarded as an important development, because its parameters were fitted to ab initio data (on small clusters) and because partial covalence was modeled by the use of partial charges and a

compensating short-range attraction. The BKS potential [127] went further along this line by re-parameterizing the TTAM potential on experimental data for quartz, an extended solid. The deficiencies of rigid-ionmodels have been neatly discussed by Wilson et al [128]. In particular, rigid-ion models were shown to be unable to reproduce the experimental gap between stretching and bending frequencies in the infrared spectra of silica glass. It was instead shown that by allowing oxygen ions to be polarizable, the infrared spectra could be substantially improved. The TS potential was developed starting from the ideas of Wilson et al, with the additional feature that its parameters were obtained by best fit to forces, stresses, and energies obtained by ab-initio methods on selected configurations in the liquid [29]. Previous simulations using the TS potential are in very good agreement with experimental data on the structural properties of most SiO_2 low-pressure crystalline polymorphs, liquid and glass [129]. The temperature dependence of the c/a ratio in α- and β- quartz (see Fig. 2.3), and pressure dependence of the lattice constant across the rutile-to-$CaCl_2$ transition (see Fig. 2.4) are just a few examples of the accuracy of the potential
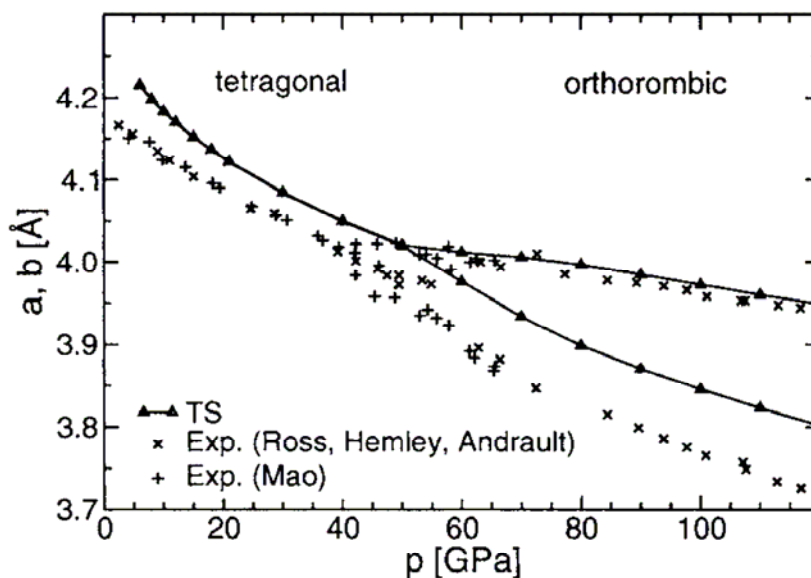

Fig. 2.4 Lattice constants a and b against pressure across the stishovite-$CaCl_2$ transition [129]

with respect to other existing force-fields for silica. The TS potential has been shown to reproduce the Si-O-Si angular distribution in the liquid and in all the low-pressure crystalline silica phases better than rigid-ion potentials. Recent work has shown that the TS potential agrees very well with ab-initio calculations on the vibrational density of states (VDOS) of quartz, indicating that the vibrational properties are also reproduced faithfully by the TS potential.

In the year of 2000, Stixrude [130] gave a serious review for all the classical potentials (existing at that moment), which have been used to study silica glass, i.e. none of the potentials can reproduce the thermodynamic stabilities for all the silica stable phase. This situation even extends to density functional theory calculations based on GGA approximation, where the cristobalite is predicted as the most stable phase instead of quartz [131]. And density functional theory calculations based on LDA approximation gives too low energy difference between stishovite and quartz as noted by Hamman [132]. The TS potential gives the right ordering among stable phases (as we will show it in Chapter 4). The energy difference between stishovite and quartz calculated by the TS potential is slightly higher than experiments. It is important to remark that the enthalpy of glass (at 0 GPa) is between quartz and stishovite [97], which makes the TS potential unique role in addressing the problems, treated in my thesis.

The discussion about the TS potential wouldn't be complete without mentioning some of its weakness. As far as the speed of the calculations is concerned, the TS potential is slower than two-body potentials with Coulomb terms by one or two orders magnitude, depending on the optimization of the codes. Compared to the force fields for metals, where no long-range forces are needed, the speed is slower by additional 2 orders of magnitudes. The TS potential occasionally (particularly in the liquid at high pressure) undergoes the polarization catastrophe, which can be easily treated by slightly modifying the electric response as [133]

$$\vec{p}_i = \alpha_i \vec{E}_0 \frac{\vec{E}}{E} \ln(1 + \frac{E}{E_0})$$ (2.13)

where E_0 is an adjustable parameter.

2.5 Parrinello-Rahman methods

The method introduced by Parrinello and Rahman [134] was firstly introduced to perform MD simulations with constant pressure conditions. MD simulations can be applied to finite number atoms with periodic boundary conditions. According to Parrinello and Rahman, the atomic configurations can be defined by a Bravais vectors and rescaled coordinates:

$$S_I = h^{-1} R_I$$ (2.14)

where $h = (\vec{a}, \vec{b}, \vec{c})$

The system can be described by the set of coordinates $\{h, S_I\}$ and its Lagrangian can be written as

$$L = \sum_I \tfrac{1}{2} M_I \dot{S}_{I,\alpha\beta} \Gamma_{\alpha\beta} \dot{S}_{I,\alpha\beta} - V[\{h, S_I\}] + \sum_{ij} \tfrac{1}{2} W \dot{h}_{ij}^2 - P\Omega \qquad (2.15)$$

where $\Gamma_{\alpha\beta} = h^t h$ is the metric tensor, W is a fictitious mass controlling the motion of the cell variables, P is the external pressure and $\Omega = |\det h|$ is the volume of the cell. From the Lagrangian (Eq. 2.14), we are able to derive the equation of motion for the system

$$\ddot{S}_{I,\alpha} = -\frac{1}{M_I} (h^{-1})_{\alpha\beta} \frac{\partial V}{\partial R_{I,\beta}} - (\Gamma^{-1})_{\alpha\gamma} \dot{\Gamma}_{\gamma\beta} \dot{S}_{I,\beta}$$

$$\ddot{h}_{\alpha\beta} = -\frac{1}{W} \frac{\partial V}{\partial h_{\alpha\beta}} + \frac{1}{W} \sum_I M_I h_{\alpha\gamma} S_{I,\gamma} S_{I,\beta} - \frac{1}{W} P\Omega (h^t)^{-1}_{\alpha\beta} = \frac{1}{W} (\Pi_{\alpha\gamma} - P\delta_{\alpha\gamma}) \Omega (h^t)^{-1}_{\gamma\beta}$$

where

$$\Pi_{\alpha\beta} = \frac{1}{\Omega} [-\frac{\partial V}{\partial h_{\alpha\beta}} (h^t)_{\alpha\beta} + \sum_I M_I h_{\alpha\beta} \dot{S}_\beta \dot{S}_\mu (h^t)_{\mu\nu}]$$

is the total stress tensor, the first term of Π is internal stress tensor $\pi_{\alpha\beta} = -(1/\Omega)\partial V/\partial \varepsilon_{\alpha\beta}$ and $\varepsilon = \tfrac{1}{2}(h_0^{t^{-1}} \Gamma h_0^{-1} - 1)$ is the strain tensor with reference to h_0 [135].

The mass parameter for the cell dynamics has no influence on the results obtained for static equilibrium properties, but is relevant when what is to be obtained are dynamical properties (such as phase transition). As W is the inertia, which accounts for all the infinitely replicated atoms in the periodically repeated cells, it has been suggested that its value be proportional to the total mass of the atoms in a single cell: $W = 3\sum_i M_i / 4\pi^2$ [136].

After the original work of Parrinello and Rahman several improvements of variable cell MD has been proposed. In particular constant pressure MD lends itself naturally to the introduction of

non-isotropic external stress [137], which may be used for simulations of uniaxial stress and more general non-isotropic pressure transformations (Chapters 4 and 5). The disentangled variables $\{h, S_I\}$ make it possible to calculate the component of elastic constant and yield strength (Chaper 6) [138], with time-dependent shear strains, increasing at a constant rate, at different pressures.

2.6 Some Structural Analysis Techniques

The main order parameters describing the local structure, or short-range order, in compressed glass are the Si-O bond length, the Si coordination number, and the Si-O-Si angle distribution [65, 67, 71, 72, 74, 139-145]. Changes in the intermediate range order are instead typically described by changes in the position and shape of the first sharp diffraction peak (FSDP) in neutron and X-Ray diffraction static structure factors [65,72,74, 139-146].   We calculate the neutron structure factor $S_n(\vec{q})$ as [146-148]

$$S_n(\vec{q}) = \frac{1}{N_{Si}b_{Si}^2 + N_O b_O^2} \left\langle \sum_k b_k \exp(i\vec{q} \cdot R_k) \sum_l b_l \exp(-i\vec{q} \cdot R_l) \right\rangle \quad (2.16)$$

where b_k, $k \in \{Si, O\}$, are the neutron scattering cross sections, with b_{Si} = 1.097 10^{-4} Bohr and b_O =7.840 10^{-5} Bohr [149]. R_k, R_l denote the position of atoms k and l, N is the total number of atoms, and $\langle...\rangle$ is the thermal average taken over a MD trajectory of at least 10 ps. The structure factor was then calculated for a discrete set of $\vec{q} = \{q_a, q_b, q_c\}$, fixed by the period boundary conditions as $q_a = 2\pi n_a (b \times c) / V$, $q_b = 2\pi n_b (c \times a) / V$, and $q_c = 2\pi n_c (a \times b) / V$, where the three vectors a, b and c define the simulation cell, V is the cell volume and n_a, n_b, n_c are integers, with $\mid n_{a,b,c} \mid < M$. The value of M determines the maximum q for which the structure factor is calculated. Because the glass is an isotropic system, $S(q)$ was expressed as a function of q=$\mid \vec{q} \mid$ only. Contributions at different q were convoluted with a Gaussian width of σ =0.1Å.

The X-ray structure factor $S_{X-Ray}(\vec{q})$ was calculated by replacing in (1) the neutron cross

sections with the q-dependent atomic form factors $f_k(q)$, with $k \in \{Si, O\}$:

$$S_{X-Ray}(\vec{q}) = \frac{1}{N_{Si} f_{Si}(q)^2 + N_O f_O(q)^2} \left\langle \sum_k f_k(q) \exp(i\vec{q} \cdot R_k) \sum_l f_l(q) \exp(-i\vec{q} \cdot R_l) \right\rangle \quad (2.17)$$

The form atomic factors were approximated by the general expression

$$f(s) = \sum_{n=1}^{4} a_n \exp(-b_n s) + c \quad (2.18)$$

where $s = \sin\theta / \lambda = q / 4\pi$. The parameters a_n, b_n, c relative to Si and O can be found in Ref. [150].

Changes in the position of the FSDP, which is generally located in the region $q_{FSDP} \sim 1.5\text{-}2$ Å^{-1}, are indicative of changes at length scales $2\pi / q_{FSDP} \sim 3\text{-}4$ Å. The intermediate range order at these length scales can also be described in terms of the so-called "ring statistics" [65,79,142-145], i.e. by the statistics of closed paths in the network. Closed paths, or rings, are defined here by the "shortest-path" criterion [151], and a Si-O pair is considered connected if the interatomic distance is less than 2 Å, which corresponds to the first minimum of the Si-O pair correlation function.

Chapter 3

Infrared and Raman Spectra of Silica Polymorphs

The general aim of this study is to test the reliability of polarizable model potentials for the prediction of vibrational (Infrared and Raman) spectra in highly anharmonic systems such as high temperature crystalline phases. By using an ab-initio parameterized interatomic potential for SiO_2 and molecular dynamic simulations, we calculate the infrared and Raman spectra for quartz, cristobalite and stishovite at various thermodynamic conditions. The model is found to perform very well in the prediction of infrared spectra. Raman peak positions are also reproduced very well by the model, however, Raman intensities calculated by explicitly taking the derivative of the polarizability with respect to the atomic displacements are found to be in poorer agreement than intensities calculated using a parameterized "bond polarizability" model. Calculated spectra for the high temperature β phases, where the role of dynamical disorder and anharmonicities is predominant, are found to be in excellent agreement with experiments. For the octahedral phases, our simulations are able to reproduce changes in the Raman spectra across the rutile-to-$CaCl_2$ transition around 50 GPa, including the observed phonon softening.

3.1 Introduction

Raman and infrared spectroscopies are routinely used as an experimental tool for the characterization of materials. By probing the vibrational dynamics of a material, they are very effective in providing information about its mechanical and elastic properties, as well as on the occurrence of structural phase transitions. In high-pressure physics, where alternative techniques are difficult to use in conjunction with diamond anvil cells, vibrational spectroscopies are instrumental to detect phase transitions. The theoretical determination of Raman and infrared (IR) spectra is a powerful complementary tool to experimental analysis, particularly at extreme conditions of pressure and temperature, where experiments are challenging. The theoretical analysis establishes a direct link between the peaks observed in the experimental spectra and the character of the underlying atomic dynamics and structure, and can be used to validate or dismiss structural models. Theoretical efforts to model the vibrational dynamics of solids have been to a

large extent limited to the harmonic approximation, whereby the vibrational density of states (VDOS) is obtained by direct diagonalization of the dynamical matrix obtained in the limit of small-amplitude harmonic oscillations of the atoms around their equilibrium positions. Theoretical models of IR and Raman Spectra require, in addition to the VDOS, the calculation of the derivative of the polarization vector or of the polarizability tensor with respect to atomic displacements, respectively. The derivatives can either be obtained from simple empirical models, or from an ab-initio quantum treatment of the electronic response [41,42,153,154]. The harmonic approximation holds well for most solids at low temperatures. However, a large number of materials, including ferroelectrics, ionic conductors and silicates, undergo phase transitions between ordered and disordered states (which are completely anharmonic) due to temperature and / or pressure changes. In addition, Raman spectra in various melts, especially, the liquid silicates in magmas, still lack a theoretical interpretation [154-156]. The harmonic approximation is obviously unable to describe such strongly anharmonic or fluid phases.

Attempts to go beyond the harmonic approximation normally range from the systematic calculation of higher-order contributions in terms of the atomic displacements from equilibrium, to the full time-dependent treatment of the atomic trajectories by means of molecular dynamics (MD), the latter being applicable also to fluids, where atomic displacements from the initial positions can be arbitrarily large and power expansions ill-defined. Within a molecular dynamics approach, the full VDOS can be calculated as the Fourier transform of the velocity-velocity autocorrelation function, and derivatives of the polarization and of the polarizability can be obtained "on the fly" at each instantaneous configuration of the system during its time evolution [157]. While this approach guarantees in principle a full treatment of the dynamics in anharmonic solids and in fluids, and can be extended to include an ab-initio calculation of the electronic polarization and polarizability, a full quantum mechanical approach to the determination of Raman and IR spectra has so far been severely limited by the computational overhead of the quantum mechanical response, and has been reported so far only for very simple systems [158,159]. In this context, it is clear that the development of simplified models for the calculation of Raman and IR spectra, which retain the accuracy of ab-initio treatments but at a much reduced computational cost, would be extremely useful.

In this chapter we present a model, based on molecular dynamics and on a polarizable force field parameterized on ab-initio calculations, which is able to reproduce the experimental spectra of various silica (SiO_2) polymorphs with good accuracy. The choice of silica was motivated by the availability of a polarizable force field from previous work, but also by the need to test the method on a large variety of phases with different degrees of anharmonicity and/or dynamical disorder.

Calculating infrared spectra from model potentials requires the knowledge of the polarization changes during the dynamics, which can be extracted from classical [79,115,128,160] or from ab initio simulations [159]. The results in the case of classical simulations depend on the potential employed, so the ability of a potential to reproduce infrared spectra has become an important criterion in determining the quality of a potential and in identifying the relevant interactions[79,115,128,160]. For example, the most widely used force fields for silica, such as the TTAM [126] and BKS [127] potentials, showed some difficulties in reproducing the infrared spectra of silica polymorphs [79,160]. Calculating Raman spectra requires, in addition to the polarization, also the knowledge of the electronic linear response to an electric field (i.e. the polarizability) of the system, during the vibrational dynamics. Ab-initio approaches can provide such a response, albeit with a substantial computational effort. On the other hand, empirical approaches based on rigid charges, such as the TTAM and BKS potentials are unable, by construction, to simulate the electronic response, which explains why no attempt has been made so far to provide a theoretical model for the vibrational spectra of the high-temperature β phases. we have recently developed a new polarizable force field for silica (the TS potential [29]), which describes experimental data on the structural properties of most SiO_2 low-pressure crystalline polymorphs, liquid and glass, better than any other empirical model [29,129], as detailed in Sec. II A. For the purpose of the present work however, the main advantage of the TS potential, with respect to rigid-ion models, is its fluctuating-dipole feature, which implies that the polarizability of the system (and thus its Raman spectra) can be extracted from the model itself, without further empirical and/or external assumptions. The reliability of the Raman spectra calculated with the TS potential is not obvious a priori, as the parameters of the potential were fitted to reproduce ab-initio forces, stresses and energies on selected configurations, while the electronic response was not included explicitly in the set of physical quantities to which the potential was fitted. So the

possibility exists that the parameters related to the induced fluctuating dipoles took effective values able to reproduce the structural properties, but perhaps not the electronic response, as recently shown in the case of the piezoelectrical constant [171].

The goal of this work is two-fold. On one hand we determine the accuracy of the TS potential in reproducing the Raman and IR spectra of selected silica polymorphs, including octahedral phases. On the other hand, we present a model, based on molecular dynamics, which is capable of simulating Raman and IR spectra at arbitrary temperatures, up to the fully anharmonic regime. This chapter is organized as follows: in Section 3.2, we give a brief overview of the calculation methods. In Section 3.3, we present the infrared spectra for the low-pressure phases (quartz and cristobalite) and the high-pressure phase stishovite, and compare them with the results of other potentials. In Section 3.4.1, we present Raman Spectra for quartz and cristobalite at low temperatures, and discuss the reliability of the Raman spectra calculated with the TS potential. In Section 3.4.2, we present Raman Spectra for quartz and cristobalite at high temperatures. In Sec. 3.4.3, we describe the Raman spectra of stishovite and how it changes across the rutile-to-$CaCl_2$ transition. We summarize our results in Section 3.5.

3.2 Computational Methods

3.2.1 Infrared and Raman Spectra

The infrared spectra have been calculated from the Fourier transform of the total polarization autocorrelation function, as already done for other potentials [79,115,128,160]:

$$I(\omega) = \frac{4\pi^2\omega}{3hcn}(1 - \exp(-h\omega/K_B T))\int_{-\infty}^{\infty} dt e^{-i\omega t} < \bar{P}(t) \cdot \bar{P}(0) > \tag{3.1}$$

where n is the refractive index of the medium, which for practical purposes can be treated as a constant in the calculation, h is Planck constant, c is the speed of light, K_B is the Boltzman constant, T is the temperature, and $\bar{P}(t)$ is the total polarization vector at time t, which includes rigid charges, and induced and short-range dipoles [29], and angular brackets indicate the statistical average.

Raman spectra reported in this work have been calculated by Fourier transforming the dynamical autocorrelation functions of the electronic contribution to the polarizability tensor $\vec{\alpha}$ [157,158]. Following the procedure in Ref. [158], we divide $\vec{\alpha}$ into its scalar part α and anisotropic part $\vec{\vec{\beta}}$ so that

$$\vec{\alpha}(t) = \alpha(t)I + \vec{\vec{\beta}}(t) \tag{3.2}$$

where $\alpha(t) = \frac{1}{3} Tr \vec{\alpha}(t)$ and I is the identity matrix. Then it can be shown that the polarized component of Raman intensity is given by

$$I_{VV}(\omega) = I_{ISO}(\omega) + \frac{4}{3} I_{VH}(\omega) \tag{3.3}$$

where ω is the frequency of the Raman spectra, with the isotropic scattering component given by

$$I_{ISO}(\omega) = \frac{1}{2\pi} \int dt e^{-i\omega t} <\alpha(0)\alpha(t)> \tag{3.4}$$

and the depolarized (or anisotropic) component by

$$I_{VH}(\omega) = \frac{1}{2\pi} \int dt e^{-i\omega t} \frac{1}{10} <Tr[\vec{\vec{\beta}}(0) \cdot \vec{\vec{\beta}}(t)]> \tag{3.5}$$

Because the correlation functions are computed classically, quantum effect corrections [144] are taken into account by multiplying Eq. (3.4) and (3.5) a factor $\frac{(1 - e^{-\hbar\omega/KT})}{2}$.

We calculated the tensor $\vec{\alpha}$ with two different approaches. In the "direct" approach, $\vec{\alpha}$ was calculated as the derivative of the instantaneous electronic polarization with respect to an external electric field. The polarizability tensor was also calculated at each step using the bond polarizability model [42], as discussed below.

3.2.2 The Direct Approach

In the direct approach, $\vec{\alpha}$ was calculated as:

$$\alpha_{\mu\nu} = -\frac{\partial P_\mu}{\partial E_\nu} \tag{3.6}$$

where $\vec{P}$ is the polarization vector, $\vec{E}$ is the applied electric field, μ and ν are x, y, z in Cartesian coordinates. The derivative on (3.6) was calculated by finite differences at each MD step, by keeping atoms fixed. We found that E = 0.001 atomic units guarantees that it is still in the linear regime, with negligible numerical noise. As a test of the accuracy of the method, we computed the electronic contribution (ε^{∞}) to the dielectric tensor of α-quartz as $\varepsilon^{\infty}_{\mu\nu} = \delta_{\mu\nu} + 4\pi\langle\alpha_{\mu\nu}\rangle$, where the average is taken over a MD trajectory at 0GPa and 300K. we obtained similar values for the parallel ($\varepsilon_{\parallel} = 2.295$) and perpendicular ($\varepsilon_{\perp} = 2.290$) directions to the optical axis (z axis), which is in excellent agreement with the experiments ($\varepsilon_{\parallel} = 2.383$ and $\varepsilon_{\perp} = 2.356$) [164].

3.2.3 The Bond Polarizability Model

The polarizability tensor $\vec{\vec{\alpha}}$ was also calculated, at each MD step, with the so-called bond polarizability model (BP model) [42], in which the polarizability is parameterized in terms of bond contributions as follows:

$$\alpha_{\mu\nu} = \frac{1}{3}(2\alpha_p + \alpha_l)\delta_{\mu\nu} + (\alpha_l - \alpha_p)(\frac{R_\mu R_\nu}{|\vec{R}|^2} - \frac{1}{3}\delta_{\mu\nu}) \tag{3.7}$$

where $\vec{R} = \vec{R}_O - \vec{R}_{Si}$ is the vector connecting a bonded pair of oxygen and silicon atoms located at $\vec{R}_O$ and $\vec{R}_{Si}$, respectively. The parameters α_l and α_p define the longitudinal and perpendicular contributions to the bond polarizability, respectively, and depend on the length of the Si-O bond with the following derivative:

$$\frac{\partial\alpha_{\mu\nu}}{\partial R_\kappa} = \frac{1}{3}(2\alpha'_p + \alpha'_l)\delta_{\mu\nu}\hat{R}_\kappa + (\alpha'_l - \alpha'_p)(\hat{R}_\mu\hat{R}_\nu - \frac{1}{3}\delta_{\mu\nu})\hat{R}_\kappa$$
$$+ \frac{(\alpha_l - \alpha_p)}{|\vec{R}|}(\delta_{\mu\kappa}\hat{R}_\nu + \delta_{\nu\kappa}\hat{R}_\mu - 2\hat{R}_\mu\hat{R}_\nu\hat{R}_\kappa) \tag{3.8}$$

where $\hat{R}$ is a unit vector along $\vec{R}$ and α'_l and α'_p are the derivatives of the bond polarizabilities with respect to the bond length. Notice that only the derivative of the bond polarizability is needed, as only its time-dependent changes, and not its absolute values, enter in

the construction of the Raman intensity. The derivative of the polarizability is thus completely defined, in the BP model, by three parameters:

$$\alpha = 2\alpha'_p + \alpha'_l$$

$$\beta = \alpha'_l - \alpha'_p \tag{3.9}$$

$$\gamma = \frac{\alpha_l - \alpha_p}{R}$$

Here we used the parameters of Ref. [42], which were determined by ab-initio density functional methods. In order to calculate Raman intensities with the BP model we generated a MD trajectory with the TS potential, and extracted the fluctuating part of the bond lengths by substracting from their instantaneous values the average value of the individual Si-O bonds averaged along the full trajectory. The total polarizability at each MD time step was finally determined by means of Eq.(3.6), by summing over all the Si-O bonds.

We will use both the direct method and the BP model to construct the polarizability of α-cristobalite and quartz. For the octahedral phases however no bond-polarizability model exists to our knowledge, so the polarizability was determined exclusively using the direct method. It is important to remark that while the BP model has been widely employed so far to construct Raman spectra for silica polymorphs [165], most of the calculations reported in the literature so far have been obtained in the harmonic approximation, and no calculation has been thus reported for high temperature β phases.

3.2.4 Details of the Molecular Dynamics

The MD trajectories were obtained in the microcanonical (NVE) ensemble. For quartz we used a simulation cell containing $2 \times 2 \times 2$ α-quartz unit cells, for a total of 24 SiO_2 formula units; for cristobalite a cell with $2 \times 2 \times 2$ α-cristobalite unit cells (32 SiO_2 formula units); for stishovite a cell with $2 \times 2 \times 4$ stishovite unit cells (32 SiO_2 formula units). The Verlet algorithm was used to integrate Newton's equations of motion and the time step was set to 0.72 fs throughout this work. The initial atomic configurations at low temperature were taken from the ideal crystal structures [166], and the initial velocities were taken from a Gaussian random distribution. Simulations of the

high temperature and high-pressure phases were either started from the structures of Ref. [129], or obtained with the TS potential in the NPT ensemble by increasing temperature/or pressure very slowly. Equilibration times were of the order of 200 ps for the NPT runs, which were followed by about 200 ps in the NVT ensemble. Finally, runs longer than 200 ps were performed in the microcanonical ensemble to construct the correlation functions. The finite length of the runs introduces a 2-3 cm^{-1} broadening in the spectra, which was convoluted with an additional empirical broadening of 4 cm^{-1}.

3.3 Infrared Spectra

In this Section we compare infrared spectra for quartz , cristobalite and stishovite with experiments, as well as with spectra obtained with other force fields, such as TTAM [126], BKS [127], and three-body potentials [115]. Infrared spectra for low-pressure and low-temperature crystalline phases, α- quartz and cristobalite, are in excellent agreement with experimental data [47,167], as shown in Figs. (3.1) and (3.2), respectively. Calculated frequencies are systematically underestimated, but differences are below 7-8 %. Intensities are also in fair agreement with experiments, if one considers that experimental spectra are obtained from powders and are generally broad, as a consequence of grain shape heterogeneity (see also Appendix of this thesis) [167]. A comparison with the infrared spectra obtained with the BKS potential [64] shows that the addition of polarization effects can greatly improve the quality of simulated infrared spectra, particularly for what concerns intensities, as already noted for silica glass by Wilson et al. [128].
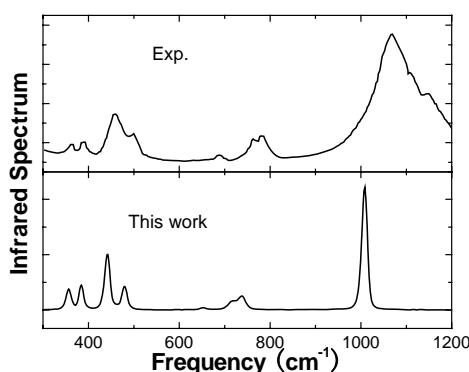

Fig.3.1 Infrared spectra for α-quartz at 0GPa and 300K. The upper panel is experiments [167]; the lower panel is our calculation.

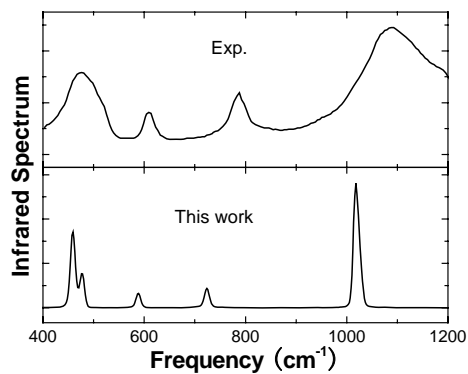Fig.3.2 Infrared spectra for α-cristobalite at 0GPa and 100K. The upper panel is experiments [47]; the lower panel is our calculations.
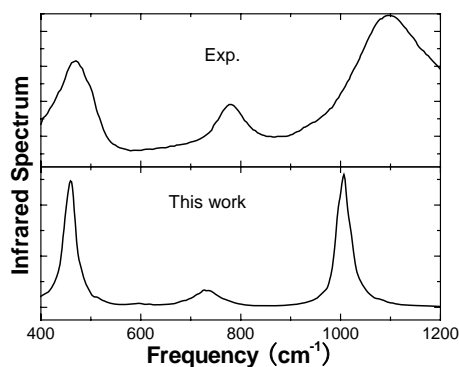

Fig.3.3 Infrared spectra for β-cristobalite at 0GPa and 600K. The upper panel is experiments [47]; the lower panel is our calculations. Note the disappearance of the 590 cm^{-1} band (609 cm^{-1} in experiments [47]) as a result of the α to β transition.

Comparison of our results for cristobalite with those obtained with a charge-transfer three-body potential [115], shows that the two models have similar intensity ratios, and that both compare well with experiments. However, peak positions with the three-body potential are in worse agreement with experiments than those obtained with the TS potential. In addition, the α to β transition is estimated to take place around 1000 K with the three-body potential [115], in contrast with experimental values ranging from 393 to 545 K [168], while the TS potential gives a value within the experimental range [129]. In Fig.3.3, we show the calculated infrared spectrum of high-temperature β-cristobalite, together with the experimental data [47]. The peak at around 600

39

cm^{-1} in the α phase, disappears in the β phase, in agreement with experiments and with the results obtained with the three-body potential [115].

The TS potential employed in this work was obtained by best fit to ab-initio data in liquid silica at low pressure, i.e. in a regime where the Si-O coordination is close to four, but for a few coordination defects. The applicability of the TS potential to 6-fold coordinated, octahedral phases, such as stishovite is thus not straightforward. However, the TS potential was recently shown to reproduce very well the c/a ratio [129] during the rutile-to-$CaCl_2$ transitions in stishovite. The lattice constants *a* and *b* predicted by the TS potential are also in excellent agreement with experiments,
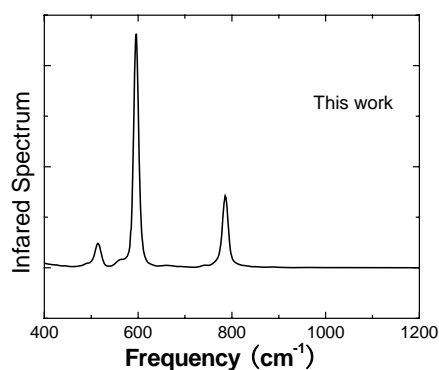

Fig.3.4 Infrared spectra for stishovite at 9GPa and 300K. The upper panel is experiments at 1 atm and room temperature (see text for explanation) [169]; the lower panel is our calculations.

and show a clear Landau-type transition around 50 GPa [129]. The only discrepancy with experiment is that the lattice constant is systematically overestimated in the simulation. While we believe that the problem might be solved by modifying the potential so as to allow the ion size and shape to vary, similarly to MgO [104], we also believe that it is important to assess whether the accuracy of the potential in its present form can be extended to octahedral phases also for what concerns the Raman and IR spectra. We show in Fig.3.4, the calculated IR spectra of stishovite at 9 GPa with experimental spectra obtained at ambient pressure [169], since we could not stabilize stishovite at ambient pressure and no experimental spectra with intensities are available at finite pressure. The position of the peaks in the calculated spectra is in fair agreement with the position of the main experimental peaks [169]. Consistent with experiments, the peak corresponding to the octahedral Si-O stretching mode lies around 800 cm^{-1}. Our results are in much better agreement

with experiments than those obtained with the BKS model [64], where all peaks lie in the 500-620 cm^{-1} range, and those obtained with a charge-transfer three body potential [62], where only two peaks were reported around 800-1000 cm^{-1}.

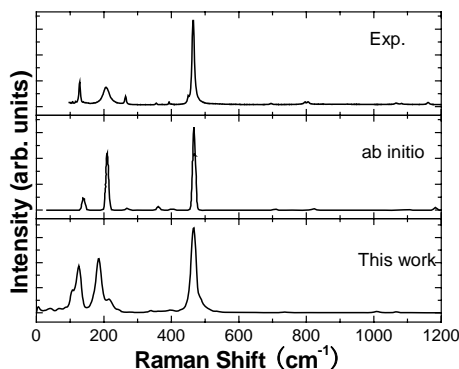## 3.4 Raman Spectra

3.4.1 Low Temperature Tetrahedral Phases

Fig. 3. 5 Raman spectra for α-quartz at 0GPa and 300K. the top panel is experiments [162], the middle panel is ab initio calculations [153], the bottom panel is our calculations, based on the bond polarizibility model (seen in Sec. 3.2.3) and the trajectory generated by MD simulations with the TS potential. Theoretical data are convoluted with a uniform Gaussian broadening with width $\sigma = 4cm^{-1}$.
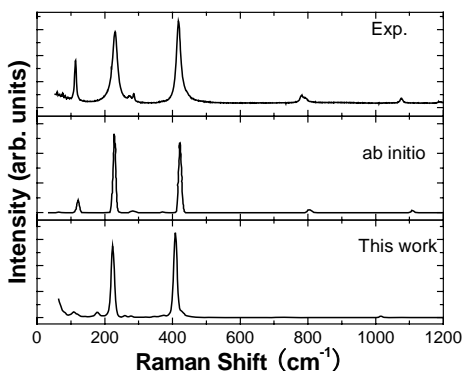

Fig.3.6 Raman spectra for α-cristobalite at 0GPa and 100K. Panels are the same as in Fig. 3. 5.

We first compare the Raman spectra calculated using the BP model (Section 3.2.3) with experiments and ab initio calculations. Raman spectra for the low-pressure and low-temperature crystalline phases, α-quartz and α-cristobalite, are presented in Figs. (3.5) and (3.6), respectively. The spectra are in excellent agreement with experimental data [48,49,162,170] and with ab initio calculations [153], especially concerning the Raman peak positions. The three main peaks for α-quartz are found at 129, 205 and 467 cm^{-1} in our simulations, compared with 128, 207(6) and 464 cm^{-1} in experiments, respectively [48,162]. The two main peaks for α-cristobalite are at 223 and 409 cm^{-1} in our simulations, compared with 230 and 416 cm^{-1} in experiments [49]. A weaker peak at around 114 cm^{-1} for α-cristobalite is found both in ab initio and our calculations. Such accuracy in the peak positions is beyond expectations, and is probably due to a compensation of errors. The ab-initio frequencies of Ref. [153], shown in Figs. 3.5 and 3.6, were in fact rescaled by 5% to match the experimental spectra. The TS potential was constructed to match the ab-initio potential, so a similar error (5%) would be expected, with respect to experimental data, in case of perfect fit. Therefore, the accuracy of the TS results (<3%) must be the consequence of a compensation between the ab-initio intrinsic error and the residual fit error.
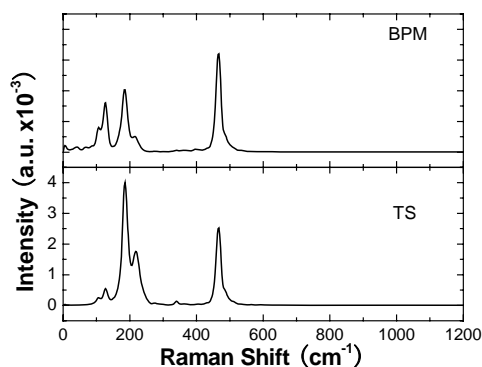

Fig.3.7 Isotropic part of the Raman spectra for α-quartz at 300K and 0GPa. In the upper panel, the intensity is obtained by the BP model (see Sec. 3.2.3); in the lower panel it is obtained with the direct approach (see Sec. 3.2.2).
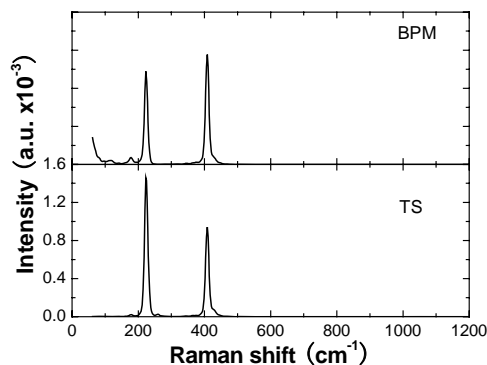
Fig.3.8 Isotropic part of the Raman spectra for α-cristobalite at 100K and 0GPa. Panels are the same as in Fig.3.7.

Intensities calculated with BP model are known to be accurate [41,42], so the agreement between theoretical and experimental intensities in Figs. 3.5 and 3.6 is not surprising. Intensities calculated with the direct approach (Section 3.2.2) turns out to be in worse agreement with experiments than those obtained with the BP model. In Figs.3.7-3.9, we compare isotropic and anisotropic parts (as defined in Eqs. 3.4 and 3.5), calculated with the two approaches for α-quartz and α-cristobalite. The peak positions are obviously the same in the two approaches, as the same MD trajectory was employed. The intensities of the isotropic parts calculated with the two approaches are also in good agreement. However, regarding the anisotropic part, the direct approach seems to perform rather badly for what concerns intensities, which are about one order of magnitude larger than with the BP model. Because the spectra obtained with BP model are in good agreement with experiment, we conclude that the current implementation of the polarizability in the TS model serves very well the purpose of providing accurate force on the atoms and first derivatives of the polarization (such as effective charges and dielectric constant), but needs further improvement in order to match the accuracy of BP model in the calculation of higher order derivatives such as Raman intensities. For this reason, Raman spectra for the tetrahedral phases at high temperature will be calculated using the BP model only.
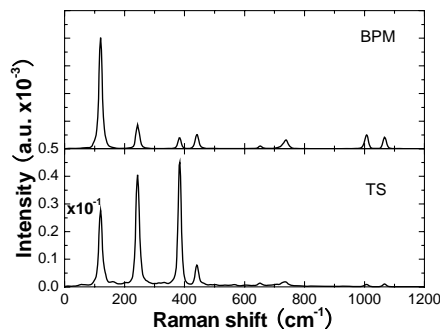
Fig.3.9 Anisotropic part of the Raman spectra for α-quartz. Panels are the same as in Fig. 3. 7.

3.4.2 High Temperature Tetrahedral Phases

Raman spectra calculated using the BP model (Section 3.2.3) for the high-temperature and low-pressure crystalline phases, β-quartz and cristobalite are compared with experimental data [48,49] in Figs. (3.10) and (3.11), respectively. we find an excellent agreement with experiments in both cases. For quartz, the modes at 129 and 205 cm^{-1} merge and are drastically attenuated; the peak around 467 cm^{-1} in α-quartz is left-shifted to 458 cm^{-1}, to be compared with a peak position at 459 cm^{-1} in experiments [48]. For cristobalite all major bands (at 110, 223 and 409 cm^{-1}) merge into a structureless bump, in agreement with experiments [49,50]. It is important to notice that Raman spectra at high temperature differ substantially with respect to the low temperature phases. In cristobalite no clear peak is observed above the transition temperature, and in quartz only one sharp peak around 460cm^{-1} remains. The capability of our theoretical approach to reproduce the
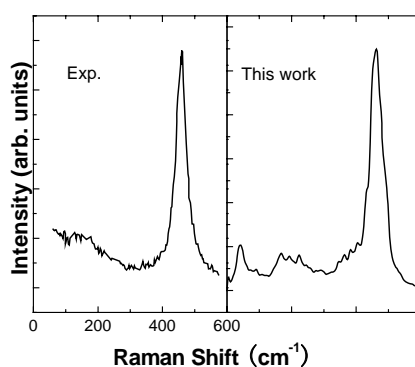

Fig.3.10 Raman spectra for β-quartz at 0GPa and 750 K. The left panel is experimental data from Ref. [48]; the right panel is our calculations based on BP model. The simulated data are convoluted with a uniform Gaussian broadening with width $\sigma = 4cm^{-1}$ as Fig. 3. 5.
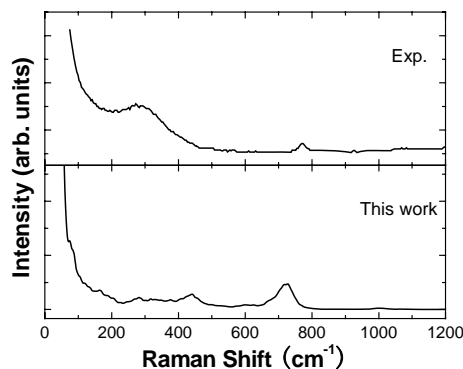
Fig.3.11 Raman spectra for β-cristobalite at 0GPa and 600K. The upper panel is experimental data from Ref. [49]; the bottom panel is our calculations based on BP model.

changes in the experimental spectra across the α-β transition suggests that the method can be applied with confidence in the study of temperature-induced transitions where the role of dynamical disorder and anharmonicities is predominant. we also remark that this is the first theoretical attempt to model Raman spectra in high temperature silica phases.

The atomistic mechanisms of the α-β transformations and the nature of the high temperature phases are still a subject of debate [50,171-178], and the correct interpretation of Raman and IR spectra may provide important hints to the solution of the debate. For example, the disappearance of the Raman and IR peaks in cristobalite has been used to rule out domain models of the transition [50]. The mode around 400-600 cm^{-1} are particularly interesting because they are connected with the displacement of oxygen atoms along the bisector direction of the Si-O-Si bond angle [41,125,162,163]. In the high-temperature (β) phases, the Si-O-Si plane normal undergoes reversals, as shown by Huang and Kieffer [115,173]. In β cristobalite, the distribution of the Si-O-Si plane normals is such that for any direction of the plane normal there is an equal probability of finding its opposite. Because in a simple bond polarization picture the plane reversals change the sign of their individual contributions to the total Raman signal, the Raman intensity around 400-600 cm^{-1} in β cristobalite is very weak. On the contrary, in quartz, the α-β transition is characterized, on average, by a 45° flip of the Si-O-Si plane normal [173], which breaks the "inversion" symmetry discussed above for β-cristobalite, and preserves the finite intensity of this mode at around 460 cm^{-1}.
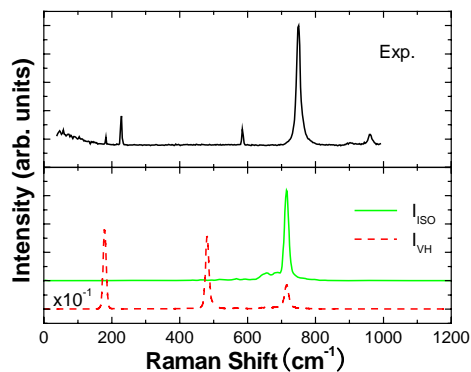
Fig.3.12 Raman spectra for stishovite at 9 GPa and 300K. The upper panel is experimental data at 1 atm from Ref. [48]; the bottom panel is our calculations using the direct approach (see Sec. 3.2.2).

3.4.3 Octahedral Phases

We focus here on the rutile-to-CaCl$_2$ transition reported to take place in experiments around 50 GPa. We notice that no BP model parametrization exists for octahedral silica, so we are forced to use the direct method (Sec. 3.2.2). In Fig. 3.12, we compare calculated and experimental Raman spectra for stishovite. Calculations were performed again at 9 GPa, as we could not stabilize stishovite at ambient pressure. No clean experimental spectra with intensities are available at finite pressure, so we report in Fig. 3.12 experimental spectra obtained at ambient pressure [48,170,179]. Pressure corrections in the Raman peak positions amount to less than 30 cm^{-1} between 0 and 9 GPa [43]. The results are in qualitative agreement with the experimental spectra, however the peak positions are systematically underestimated and, like in quartz, the intensity of the anisotropic part is overestimated. Nevertheless, it is instructive to notice the peaks at 180 and 480 cm^{-1} only come from the anisotropic part.

The pressure-induced rutile-to-CaCl$_2$ transitions is a typical example of a soft-mode-induced Laudau-type transition, as first found by Raman spectroscopy [43] and later confirmed by x-ray diffraction [44]. A detailed theoretical study of this subtle transition is potentially useful in the modeling of silica at high pressure. In Fig. 3.13, we show the pressure dependence of the vibrational modes for the stishovite, and compare it with experiments [43]. In spite of the poor accuracy in the absolute positions of the peaks, their pressure dependence appears to be correctly

46

captured by the model. In particular, the lowest peak shows a softening behavior below 51 GPa, which is consistent with experiments [43,180] and simulations [43,53,181]. Our simulations also reproduce the subsequent increase in the peak position after the transition. Considering that the TS potential was optimized for tetrahedral, low-pressure phases, the present results are quite encouraging and confirm that its range of applicability could be substantially larger, and include octahedral phases, even though with a reduced accuracy.
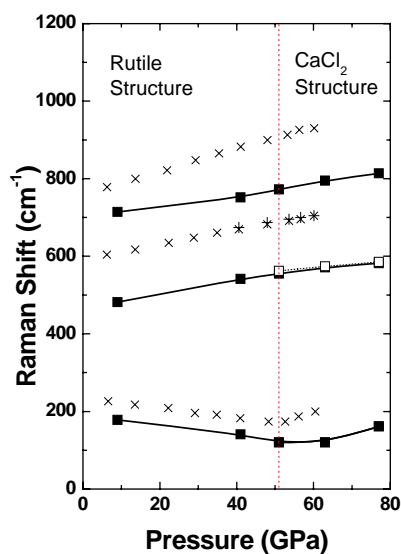

Fig.3.13 Raman shifts with pressure during the rutile-to-CaCl$_2$ transition. Crosses are experimental data from Ref. [43]; squares are our calculations, lines are guide for eyes. The lowest frequency mode clearly shows a softening around 50 GPa.

3.5 Conclusions

By using an improved, ab-initio parameterized interatomic potential for SiO$_2$, we first calculated infrared and Raman spectra for quartz , cristobalite and stishovite and compared them with experiments, as well as with spectra obtained with other force fields, such as TTAM, BKS and an improved three-body potential. The reliability of the interaction potential in the calculation of IR spectra is validated by the excellent agreement with experimental IR data both in the peak positions and in the relative intensities. In particular, we were able to reproduce the relevant spectral changes mode in the α-β transition of cristobalite. For the octahedral phases, even though

the agreement with experiments is worse than for the low-pressure phases, the potential reproduces the three main modes with reasonable accuracy.

In the case of Raman spectra, peak positions turned out to be in good agreement with experimental and ab initio calculations. However, intensities determined by explicitly calculating the derivatives of the polarizability with respect to atomic displacements turned out to be in worse agreement with experiments than those obtained when a parametrized bond polarizability model was employed. Raman spectra calculated using the bond polarizability model for the high-temperature and low-pressure crystalline phases, β-quartz and β-cristobalite were found to be in excellent agreement with experiments. It is important to remark that the atomic dynamics in the proximity of α-β transitions and in the high temperature β phases is generally considered to be highly non-harmonic. Our results suggest that the present method can be extended to the study of other temperature-induced transitions where the role of dynamical disorder and anharmonicities is predominant. The performance of the potential in octahedral structures was evaluated by calculating Raman spectra across the rutile-to-CaCl$_2$ transition at around 50GPa. In spite of the poor accuracy in the absolute positions of the peaks and the relative intensities, their pressure dependence appears to be correctly captured by the model. In particular, the lowest frequency peak shows a softening behavior below ~50 GPa, which is consistent with experiments and other calculations.

Polarizable model potentials are increasingly used in the simulation of water and bio-molecular systems [169,113,114], where vibrational spectroscopy is still a primary source of information about microscopic structure and dynamics. Our study highlights virtues and deficiencies of a polarizable model in the determination of Raman and IR spectra in the highly anharmonic regime in the specific case of silica. The study shows that the silica model performs very well for IR spectra, but suggests that improvements are required in the polarization part before a satisfactory agreement with experiments can be reached on Raman intensities. On the other hand, combining the MD trajectories obtained with the polarizable potential with a parameterized model for the polarizability yields results in very good agreement with experiments for Raman intensities.

Chapter 4

Pressure-induced Collapse of Cristobalite

The transformation of SiO_2 cristobalite into denser phases with octahedral coordination has been recently proposed to follow a two step process consisting of a collapse of the oxygen sublattice into a close packed arrangement, followed by the transformation of tetrahedral units into octahedral. The result of the transformation is also known to show a strong dependence on the presence of non-hydrostatic conditions. The present (atomistic) simulations shown in this chapter show that the collapse of the oxygen sublattice is concomitant with the disappearance of tetrahedral units and that the collapse is strongly affected by non-hydrostatic conditions. Different non hydrostatic stresses yield phases with different oxygen close packed sublattices, including the observed α-PbO_2-like phase, for which a microscopic formation path is provided, and phases with a cubic close packing, like anatase, not seen in experiments yet.

4.1 Introduction

Understanding the structural response of silica to the application of elevated pressures has wide-ranging implications in fundamental physics, Earth and material sciences. The structural collapse of the tetrahedral network, typical of the ambient pressure phases, into denser lattices with silicon in octahedral (six-fold) coordination has attracted considerable interest in recent years. Following the discovery of stishovite [40], a number of other octahedral or even denser phases of silica have been synthesized in the laboratory, or discovered as extraterrestrial minerals [33,34,40,43,44,46]. The structural collapse of cristobalite from its tetrahedral form into denser forms has been difficult to characterize, due to the strong dependence of the structure of the denser forms on the experimental procedures. Room temperature experiments have reported the appearance of new phase (phase XI) between 10 GPa and 26-30 GPa [3,5,6,37, 51,57-60,96], but attempts to index the structure have so far failed due to the poor quality of the diffraction patterns. By further compression, a number of metastable/or stable octahedral silica phases have been reported below 120 GPa at room temperature [3,5,6,37, 51,57-60,96]. Nonhydrostatic components

have been shown to affect the experimental outcomes substantially [34,51,96]. Experiments at high temperature, with laser-heated diamond anvil cells, have described the direct transition of cristobalite into a α-PbO$_2$-like octahedral phase around 45-64 GPa [46,51]. A similar phase has been detected in the martian meterorite Shergotty, a shocked achondrite probably subjected to pressures of ~30-45GPa [33]. Experiments and theories however show that the α-PbO$_2$ structure becomes thermodynamically stable only above ~98GPa [52-56]. The occurrence of a transition from cristobalite to metastable α-PbO$_2$-like within the thermodynamical range of stability of stishovite or of the CaCl$_2$-like phase can be explained in terms of kinetics arguments, which require the existence of a microscopic path way connecting the two phases. First principles and classical molecular dynamics studies would in principle be ideally suited to study the microscopic details of the collapse of cristobalite. However simulations have only obtained stishovite as the first octahedral phase below 50 GPa [61-64] and stishovite has never been reported so far in experiments starting from cristobalite. Moreover, simulations have never addressed so far the role of non hydrostatic conditions, which are instead known to play an important role in the transformation.

In a recent attempt to clarify the microscopic nature of the structural collapse of cristobalite, Huang et al [62], based on a combination of classical and first-principle simulations, have proposed a two-step mechanism whereby the formation of the octahedral units is pre-empted by a continuous transition of the oxygen sublattice, within a tetrahedral phase (phase X-I), into a (hexagonal) close packed lattice. The concept of a two-step transition allows to reconcile the evidence, from X-ray diffraction, of a low compressibility for phase X-I [3], with that of tetrahedral order within the same phase, as inferred from infrared and Raman spectroscopy [37,84,85]. However, the behaviour of cristobalite would then have to be clearly distinct from that of quartz, where the oxygen sublattice approaches continuously a body-centered cubic (bcc) structure and the collapse into a close packed arrangement is only observed as a result of a sharp transition into post-quartz phases. Moreover, phase X-I is reported to transform, in the second step of the process described in Ref. [62], into stishovite, which has never been observed in experiments starting from cristobalite so far.

To summarize, while the dominant role of the oxygen sublattice and of nonhydrostatic stresses have been recognized as central in driving the transformation of cristobalite into denser phases, the two aspects have been so far treated independently, and no attempt has been made to rationalize the diversity of experimental outcomes.

4.2 Description of Oxygen Packing

The problem of predicting, a priori, the structure that a crystal will adopt is even today (with powerful computer), very difficult. Faced with this problem one looks for approximate but general principles that serves both as aids to rationalizing crystal structures and as guides to predicting the structures of new compounds. An example from the crystal chemistry of metals is the space principle, which states that atoms of an element or alloy pack together to fill space as well as possible. The wide occurrence of hexagonal closest packing (hcp) or cubic closest packing (ccp) is rationalized on this basis.

It has been shown in some examples that observed ionic crystal structures (with partially covalence) are close to those for both a maximum in volume and a minimum in electrostatic energy subject to the constraint of fixed nearest neighbor distance [182]. It is instructive to consider examples where the requirements of maximum volume (Madelung constant) and covalence (bond lengths and angles) are in conflict. Not surprisingly the structure represents a compromise. Often the structure at low pressure is one, which is favorable for directional bonding (so that e.g. Si is tetrahedrally surrounded by anions). For example, in silica case, such as quartz, crystalbalite, coesite and clathrate structure can be well described by rigid unit model (RUM) [176].

The oxygen packing is becoming more predominant, as the "rigid" tetrahedral unit is highly distorted under pressure as suggested by many experiments [183,184]. It is the case in quartz, where it is well accepted that the quartz at high pressure can be described by oxygen bcc sublattice [183-185]. The way of looking at the structure in terms of oxygen packing has a wider application, including the case of high-pressure forms [186]. For instance, stishovite and α-PbO_2 silica obtained in high pressure has closely packed sheets of oxygen atoms, for which the arrangement

of SiO$_6$ octohedra differs. Furthermore, Teter et al [54] have found that a large class of energetically competitive phases can be generated from hcp arrays of oxygen with silicon occupying one-half of octahedral sites by first principles total energy calculations. Fcc is also possible in terms of eutaxy [182]. The next subsection describes an efficient way to distinguish among them.

4.2.1 Analyzing Oxygen Packing by Pair Analysis—HA index

The local coordination structure around oxygen has been described by the pair analysis technique. The pair analysis technique, which is first used by Blaisten-Farojas [187] for decomposing the first two peaks of the pair correlation function and generalized by Honeycutt and Andersen [188] has been widely used to monitor liquid, glass and crystalline structure [189-192]. In this technique pairs of atoms can be classified by the relationship among their neighbors with four indices of integer (for short, HA index). The first integer indicates whether the pair of atoms is bonded or not: 1 if the pair is bonded and 2 otherwise. The second integer represents the number of neighbors shared by the pair atoms. The third integer represents the number of bonds among the shared neighbors. The fourth integer is used to distinguish the pair atoms when the first three integers are not sufficient. As an example, Fig.4.1 shows how to define the type of bonded pairs within ideal bcc lattice.

The local structure of polyhedron is obtained based on HA index. We define a bcc-type atom/polyhedron, which has 6 pairs of 1441 bonds and 8 pairs of 1661 bonds; and define a fcc-type atom/polyhedron, which has 12 pairs of 1421 bonds; and define a hcp-type atom/polyhedron, which has 6 pairs of 1421 bonds and 6 pairs of 1422 bonds. The equal bonding number is chosen for the pair analysis in order to reduce the arbitrariness coming from different cutoff distances. Fcc/and hcp is 0 percentage when 14-coordinated oxygen is assumed; bcc is 0 percentage when 12-coordinated oxygen is assumed.
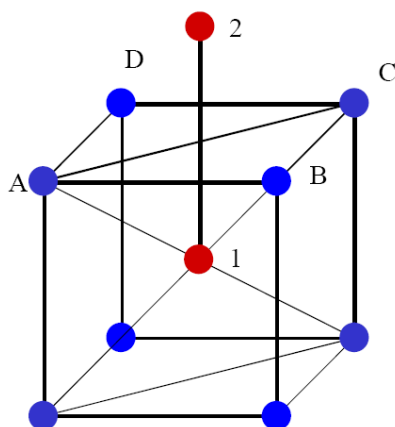
Fig.4.1 Sketch of pair analysis. 1441 and 1661 in bcc lattice, as examples to show how to define HA index: bonded "atom 1" and "atom 2" is an example of 1441, bonded "atom 1" and any of "atoms A/B/C/D" is the example of 1661. We define a "atom 1" is bcc-type atom/polyhedron, only if "atom 1" has 6 pairs of 1441 bonds and 8 pairs of 1661 bonds.

4.3 Transformation Between Packings

In this section I will briefly describe two transformation paths, between fcc and bcc, and between bcc and hcp, which will be described in the context of oxygen packing in silica at high pressure. The bcc-hcp transition [193] and bcc-fcc transition [194] happen, where the shear modulus $C' = (C_{11} - C_{12})/2$ approaches zero.

4.3.1 Bain Path

Bain path is a microscopic mechanism in the transition from bcc to fcc and vice versa [195]. Let us consider a bcc lattice in a cube whose side is of length a (Fig.4.2). The plane $ABCD$ perpendicular to a face diagonal is a rectangle of sides of a and $\sqrt{2}a$. If we stretch the bcc cube along the edge BC so as to make $A'B' = B'C'$, we can easily recognize in the diagonal $A'B'C'D'$ of the tetragonal body centered cell one of the cubic faces of the fcc lattice. The reverse is also true since by compressing an fcc lattice it is possible to generate a bcc structure.
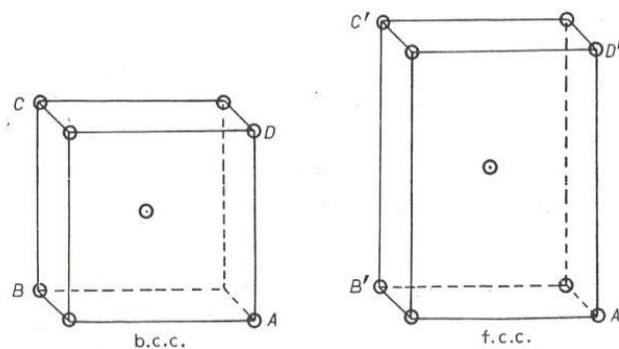
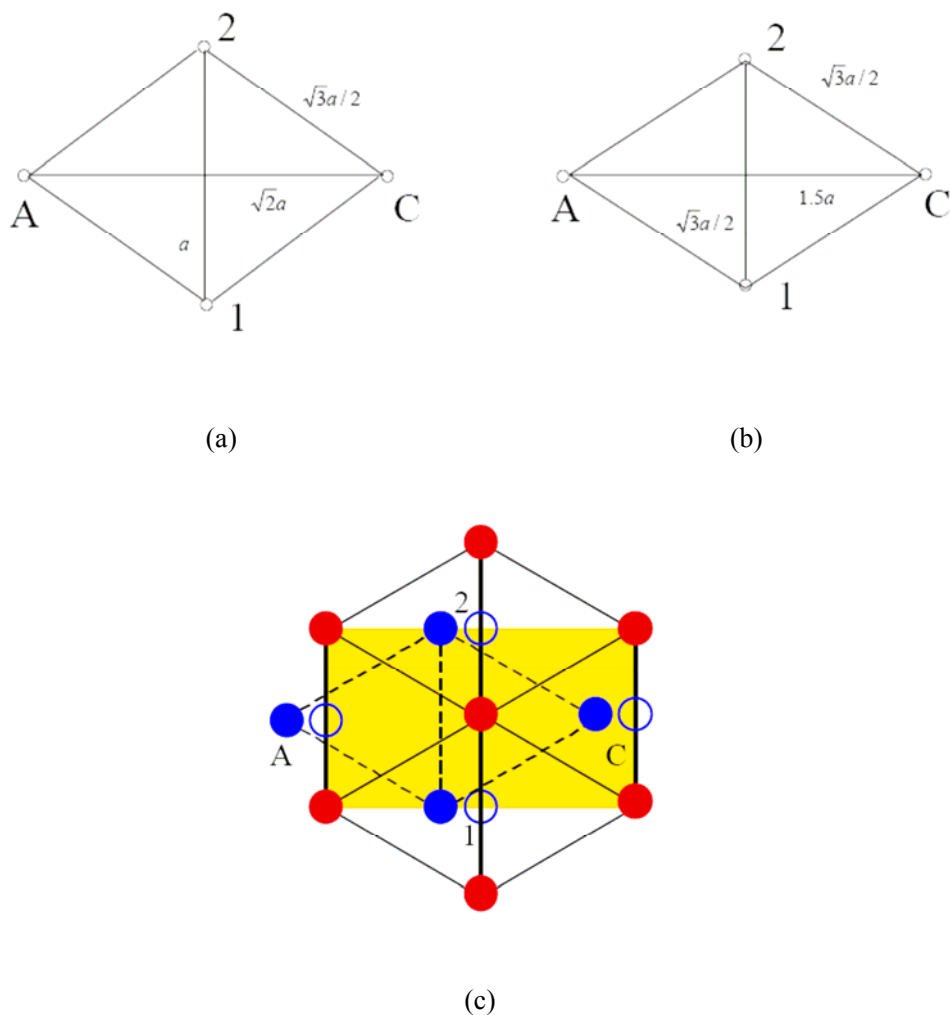Fig. 4.2 The sketch of Bain path after Parrinello [136], see text.

(a)   (b)

(c)

Fig. 4.3 The sketch of Burgers path, point 1 is denoted as P_1 and point 2 denoted as P_2 in text, the

plane AP_1CP_2 is the same as in Fig. 4.1.

4.3.2 Burgers Path

Burgers path is a microscopic mechanism in the transition from bcc to hcp and vice versa [196]. Let us consider a bcc lattice in a cube whose side is of length a (Fig.4.1). The plane AP_1CP_2 perpendicular to a face diagonal is a rhombus of side of $\sqrt{3}a/2$ (Fig.4.3a). If we compress the bcc cube along the edge P_1P_2 so as to make $P_1P_2 = \sqrt{3}a/2$, we can easily recognize the diagonal plane AP_1CP_2 (Fig.4.3b) as basal plane of "hcp". A subsequent shuffle of the basal plane results in the ideal hcp structure (Fig. 4.3c). The reverse is also true since by stretching an hcp lattice it is possible to generate a bcc structure.

4.4 Results and Discussions

Here, I present the results of simulations of the pressure-induced collapse of cristobalite done for different combinations of non hydrostatic stress. The simulations were carried out using TS potential [29]. As mentioned in Chapter 2, the force field describes the structural and vibrational properties of most SiO_2 crystalline polymorphs, liquid and glass [29,129] better than all the available force fields to which it has been compared so far. In particular, it describes the thermodynamic stability of the crystalline polymorphs of silica (Fig.4.4), at the same level of ab-initio simulations [131,132], including the pressure dependence of the lattice constant and the phonon softening across the rutile-to-$CaCl_2$ transition (see Chapter 3) [129].

Molecular dynamics (MD) simulations are started from a α-cristobalite cell consisting of 256 SiO_2 formula units (4×4×4 unit cells). The MD time step was set to 0.72 fs. A stepwise hydrostatic compression at 300 K is then applied, with pressure increments of 2 GPa, followed, at each pressure, by an equilibration time of 20 ps. A clear volume collapse can be identified in the equation of state, at a pressure of about 25 GPa (see Fig. 4.5), with a negligible dependence on the compression rate. Before the collapse, the phase is tetrahedral, shows tetragonal symmetry ($P4_12_12$) and parameters at 24 GPa (a=4.2767, c=6.1021, u=0.3596, x=0.2294, y=0.2228, z=0.2256) [197], in reasonable agreement with the d-spacings obtained by x-ray diffraction at 3.46 Å, 2.94 Å, 2.67 Å, 2.49 Å and 2.14 Å at the same pressure [3,5,58,96]. Infrared spectra (Fig.4.6) calculated at 0 and 18 GPa, are in better agreement with experiments [84] than the spectra calculated in ref. [62],
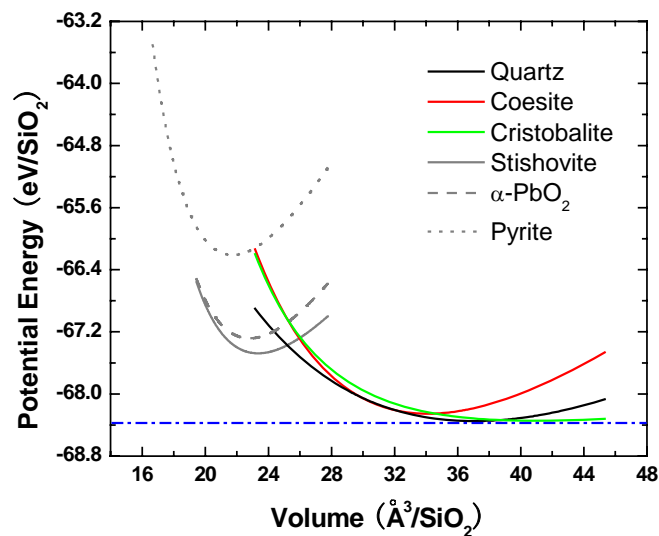
(a)
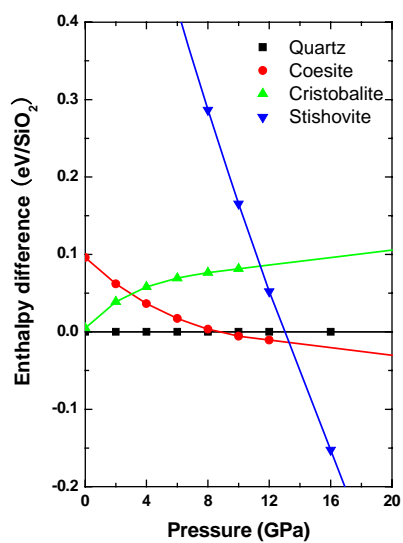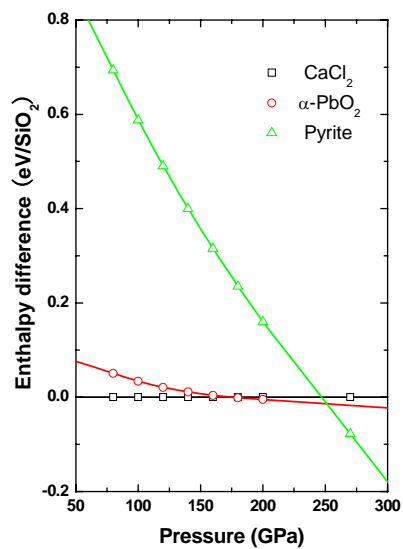
(b)   (c)

Fig.4.4 Equation of state of silica polymorphs (a), enthalpies versus pressure for a set of SiO_2 polymorphs (b) and (c), calculated with our force field.

Structure type	Space group (no.)	Oxygen Packing	Initial Structure	Stress Condition (xx,yy,zz)	Transition Pressure
Hp-cristobalite	92	BCC	α-Cristobalite	$xx, yy, zz = 0$	~10 GPa
Anatase	141	FCC	Hp-cristobalite	$xx, yy \leq 10\%; zz \leq 4\%$	28 GPa
PbCl$_2$	62	FCC	Hp-cristobalite	$xx, yy > 10\%, zz = 0$	28 GPa
α-PbO$_2$	60	HCP	P2$_1$(z=4)	$xx, yy, zz = 0$	58 GPa
P2$_1$(Z=4)	4	-	Hp-cristobalite	$6\% < xx, yy, zz \leq 20\%$	36-50GPa
P2$_1$(Z=4)	4	-	Hp-cristobalite	$xx = 0, yy = -6\%, zz = 6\%$	50 GPa
Stishovite	136	HCP	Hp-cristobalite	$xx, yy = -3\%; zz = 6\%$	32GPa
Stishovite	136	HCP	Hp-cristobalite	$xx, yy = -2.5 \pm 0.5\%; zz = 5\%$	34 GPa
CaCl$_2$	58	HCP	Stishovite	$xx, yy, zz = 0$	50 GPa
P2$_1$/c (Z=8)	14	CP[a]	Hp-cristobalite	$xx = 5\%, yy = -10\%, zz = 5\%$	48 GPa
P2$_1$(Z=4)	4	-	Hp-cristobalite	$xx = -5\%, yy = 0, zz = 5\%$	52 GPa
Pyrite	205	FCC[b]	P2$_1$(z=4)	$xx = -10\%, yy = -10\%, zz = 20\%$	74 GPa

[a]close packing different from hcp and fcc.
[b]silicon packing.

Table 4.1 Dependence of the resulting structures and oxygen packing geometry on the differential stresses (expressed in percentage of the average of the diagonal values of the stress tensor).

a likely consequence of the improved model used in this work to calculate infrared intensities. The present work also agrees with the simulations of Ref. [62], both in terms of space group and internal parameters. However, it disagrees on the structure of the oxygen sublattice, a crucial point in the analysis of Ref. [62]. To this aim, carried out a detailed pair analysis [188]. The analysis shows (Fig. 4.7) that the oxygen sublattice before the volume collapse is still bcc-like, and transforms to close-packed only after the collapse, in concomitance with the transition to octahedral coordination. This is confirmed also by the integral of the O-O pair distribution function (PDF), which reaches a plateau value of 14, typical of bcc local coordination, in correspondence to the first minimum of the PDF (see the insets of Fig. 4.7). A gradual approach of the oxygen sublattice to a bcc-like structure has been first reported for quartz [183], where it is believed to lead to the structural instability responsible for amorphization [184,185].
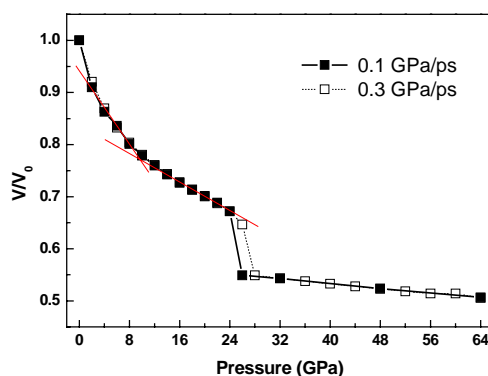

Fig.4.5 Scaled volume versus pressure for compressed cristobalite.

Further compression leads to volume collapse (Fig. 4.5) and to the transition to structures with silicon in higher coordination than four. At variance with the results of Ref. [62], changes in silicon coordination and oxygen close packing take place in a single step. It is crucially important to find that the structure resulting from the collapse depends strongly on the stress conditions. Table 4.1 reports the results of compression of cristobalite at zero temperature by subjecting the sample to anisotropic stresses along different directions. Simulations were performed with 32 SiO_2 formula units. Tests with larger (up to 576 SiO_2 formula units) and smaller (down to 16 formula units) cells yielded identical results. Identical results were also obtained by replacing the use of the MD time evolution with a structural optimization (i.e. quenching the structures to zero temperature)

at each pressure, indicating that temperature effects are negligible at least at 300 K. As shown in Table 4.1, stishovite could be obtained by applying a small (about 5-6%) uniaxial compressive component along the bcc *[100]* axis (or *c* axis in our setting). Of particular interest is a phase of symmetry $P2_1$ (z=4) obtained for compressive uniaxial components larger than 6%. The phase has silicon in five-fold coordination, and transforms, under further hydrostatic compression to 58 GPa, into the α-PbO_2 phase. The existence of a microscopic path connecting cristobalite to α-PbO_2
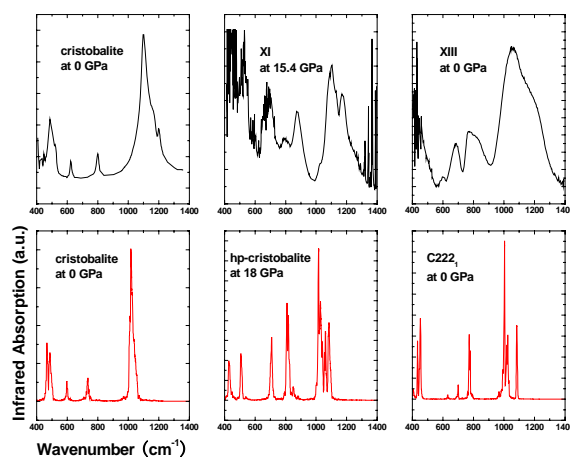

Fig. 4.6 Calculated IR spectra (lower panels) compared with experimental data [84] (upper panels) at different pressures. Phase $C222_1$ was recovered from phase $P2_1$ at 44 GPa (see text).

explains the observation of α-PbO_2 from the compression of cristobalite at pressures much below the thermodynamic range of stability of the α-PbO_2 phase. The existence of an intermediate phase in the transformation of cristobalite to α-PbO_2 is consistent with the evidence that samples recovered from 40 GPa display an infrared spectrum which does not match neither that of cristobalite nor that of α-PbO_2 [84]. Quenching the intermediate $P2_1$ monoclinic phase to 0 GPa results in a new tetrahedral phase with $C222_1$ (Z=8) space group, whose infrared spectrum (Fig. 4.6) is in very good agreement with the spectrum measured for the phase recovered from compression of cristobalite to 40 GPa [84]. On the other hand the α-PbO_2-like phase obtained at 58 GPa could be recovered to 0GPa in our simulations, without further transitions. It can therefore be concluded that the transformation from cristobalite to α-PbO_2-like, proceeds through the formation of an unquenchable intermediate phase and it can be confirmed that the phase recovered from 60-64 GPa in Refs. [5,6], and from 53.1GPa in Ref. [3] is predominantly α-PbO_2-like.

Finally, anisotropic compression of the $P2_1$ phase leads to the pyrite structure at 74 GPa. Pyrite-like SiO_2 has been reported to form in hydrostatic conditions at about 268 GPa [40] and becomes thermodynamically stable with our force field at 250 GPa. Our results indicates that anisotropic compression lowers the transition pressure to pyrite considerably. A new octahedral monoclinic phase $P2_1/c$ (z=8) was also obtained, with a close-packed oxygen lattice that is neither hcp nor fcc. Prokopenko et al. have suggested a structure with the same space group [57,60] in order to reproduce a small but unexplained Bragg peak at 3.5 Å in their X-ray diffraction patterns, which our new monoclininc phase also displays. Their number of SiO_2 formula units per unit cell (Z=6) differs from ours (Z=8), so it is not clear whether it is the same structure.
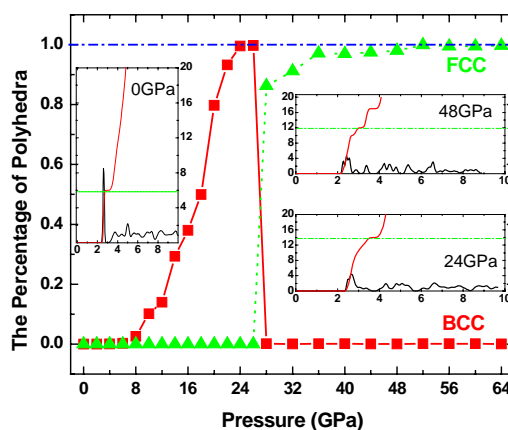

Fig.4.7 Calculated polyhedral changes for hydrostatically compressed cristobalite. Insets show pair distribution functions and average coordination numbers at selected pressures. The y-axis in the insets refers to coordination numbers.

For ideal hydrostatic conditions the structure resulting from the volume collapse is, in our simulation, isostructural to anatase [197]. The phase can be recovered to ambient pressure and the analysis of the structure factor at 0GPa shows peaks at 3.2 Å, 2.15 Å, 2.05 Å, 1.74 Å and 1.48 Å, which coincide with the peaks observed for the recovered α-PbO_2-like phase, except for an additional peak that the latter has around 2.5 Å [5,6]. The discrepancy between our simulations and those based on ab-initio MD, which reported stishovite as an outcome of the collapse, can be explained by the difference in time scales in the two simulations. A simulation with our force field at a much higher compression rate, comparable to that of ab-initio MD, yielded in fact a much higher pressure for the volume collapse (40-50 GPa), and stishovite as a product. Neither the

anatase nor the stishovite structure have been seen in experiments from cristobalite yet. Whether this discrepancy is due to difficulties in reaching perfect hydrostatic conditions in experiments, or to a systematic error in the calculation of stresses in ab-initio and classical simulations, or, finally, to kinetic arguments, is difficult to say at this point. Interestingly however, anatase differs with respect to all octahedral forms reported so far by its cubic close packed (fcc) arrangement for the oxygen sublattice, as opposed to the hexagonal close packed arrangement found in all other forms. Monitoring the atomic trajectories of the oxygen sublattice during the collapse to anatase shows
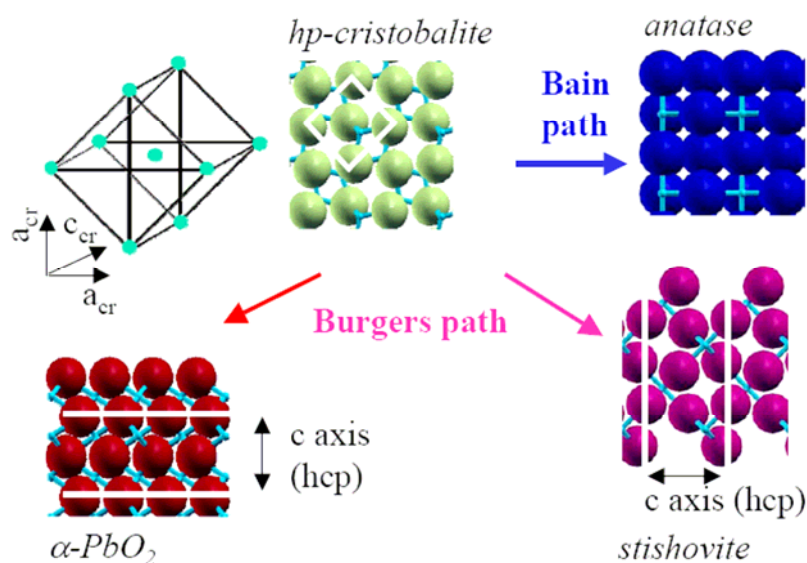

Fig.4.8 Crystallographic orientations of the oxygen quasi-bcc sublattice in the initial phase (hp-cristobalite) and after transformation to octahedral phases. Axes with "cr" subscripts refer to the principal axes of hp-crystobalite. Notice that the hcp basal planes in α-PbO$_2$ and stishovite are orthogonal. For simplicity, P2$_1$ is not shown here.

that the transition from a bcc to a fcc arrangement follows the Bain path [181], which proceeds through the elongation of one of the bcc *[100]* axes. Similarly, the collapse into the hcp oxygen sublattice in stishovite proceeds through the compression of the bcc *[100]* axis, i.e. along the so-called Burgers path [182]. The above transition path analysis and in particular the finding that ccp or hcp sublattice formation proceeds through opposite strains along the original bcc *[100]* axis (Fig. 4.8), explains the sensitivity of the resulting oxygen sublattice on the residual anisotropic

components of the microscopic stress tensor in the sample, and may therefore explain the large diversity of results reported in the literature.

This observation also explains why the transition between $CaCl_2$ and α-PbO_2-like phases is very sluggish even at very high temperature [51]. Stishovite and the α-PbO_2-like phase share the same hcp oxygen sublattice, but the two hexagonal basal planes are orthogonal (Fig.4.8), if seen from the perspective of the bcc sublattice from which they both originate, therefore a large structural reorganization is required to transform them into one another. Different paths (besides Bain and Burgers) can also be activated through particular stress configurations, leading to more complex close packing arrangements. For example, oxygen packing in the octahedral monoclinic phase with space group $P2_1/c$ (Z=8) is neither hcp nor fcc. A complete exploration stress configurations with off-diagonal terms has not been attempted, as the results obtained with diagonal stresses are already richer than expected.

4.5 Conclusions

To summarize, the present work shows that the collapse of the tetrahedral network in cristobalite is concomitant with the collapse of the oxygen sublattice from a bcc-like to a close packed arrangement, and does not take place in two steps, as recently proposed. The current analysis explains the large amount of conflicting experimental evidence regarding the dense phases of silica by invoking the important role of non hydrostatic stresses in driving the formation of different oxygen packing arrangements, including the appearance of the α-PbO_2-like phase which, so far, lacked a microscopic connection with the original cristobalite phase, and the suggestion that a phase with a cubic close packed arrangement for the oxygen sublattice may be synthesized under appropriate stress conditions. Controlling the amount and geometry of non hydrostatic components in DAC experiments is challenging, but the present results suggest that efforts in that direction may prove fruitful.

Chapter 5

Pressure-induced Collapse of Quartz

The present results, based on extensive molecular dynamic simulations, confirm that quartz between 20 GPa and 30 GPa can be described by oxygen bcc sublattice. Under further hydrostatic compression, or slightly non-hydrostatic loading, a bifurcation in its stress-strain relation has been found, which follows either dynamic instability leading to a phase with $P3_2$ ($Z=9$) space group, or a shear instability leading to phases with C2 and $P2_1/c$ space group via Bain and Burgers paths, respectively. Raman spectra based on density functional perturbation theory and X-Ray structure factor calculated for various phases indicate that features reported experimentally as evidence for quartz-II are consistent instead with the features calculated for quartz. We suggest that the close packing of the oxygen sublattice induced by stress inhomogeneities is the cause of bulk amorphization.

5.1 Introduction

Large energy barriers hinder the transition of compressed SiO_2 quartz to the high-pressure phases coesite and stishovite. At 21 GPa quartz collapses into quartz-II, a poorly crystallized metastable phase with undetermined structure [4], followed either by amorphization [7,179] or by transition to metastable high-density crystalline polymorphs [39,92]. Rationalizing such a complex behavior requires microscopic models for quartz-II, for the amorphous phase, and for the transition mechanisms, which have not been extracted from experiment yet. The pressure-induced amorphization of quartz has been examined either from a thermodynamical point of view (as a density-driven transition to the reentrant highly viscous liquid [7,198], a phenomenology first observed in ice [8]) or from a mechanical standpoint (as an elastic/dynamic instability of the quartz lattice [88-91]). None of these scenarios accounts for the observation of quartz-II, or for the crystalline sequence found in some experiments [39,92], or all together.

Atomistic simulations can in principle provide microscopic models [88-91,199,200], which can help rationalizing the observed phenomenology. To date simulations with empirical potentials have confirmed the experimental evidence that nonhydrostatic stresses play an important role [7],

but simulations under nonhydrostatic conditions yield a crystalline structure with 100% Si(V) atoms (V stands for five-fold coordination with oxygen) [201], which is not consistent with
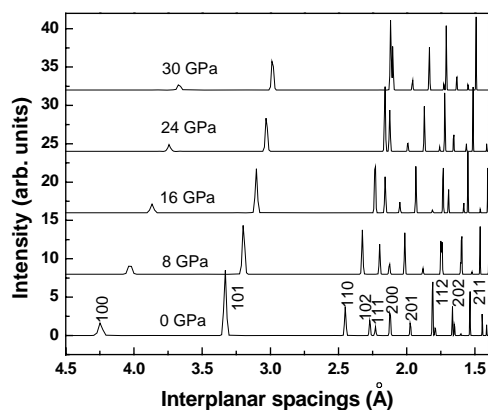

Fig.5.1 Calculated X-Ray diffraction pattern at different pressures, which is showing the two Bragg peaks (110) and (102) converge together above ~20GPa.

experiments. On the basis of first-principles simulations, where the interatomic potential is generated from a quantum mechanical solution of the electronic ground state, a structure with $P3_2$ (Z=9) space group has been proposed for quartz-II [202], however, another ab initio simulations, under non-isotropic pressure, obtained a C2 structure [203] as many previous classical calculations under hydrostatic pressure [200]. The comparison of calculated diffraction patterns for these model structures with the experimental patterns does not yield a unique solution. On the other hand, Raman and IR measurements suggest only a minor structural change between quartz and quartz-II [36,38,97]. No vibrational calculations have been reported so far for the quartz-II theoretical candidates, however. Moreover, no evidence for an amorphous phase has emerged from previous ab initio calculations [202,203].

In Chapter 4, I have presented the structural transformations for compressed cristobalite. Analysis of the atomic pathways reveals the crucial role played by the oxygen sublattice in the interpretation of the transition sequence. Cristobalite (hp-cristobalite) between 10GPa and 26 GPa can be explained as oxygen bcc sublattice, followed by fcc sublatiice phases (anatase or $PbCl_2$) or hcp sublattice phases (stishovite or α-PbO_2 phase) controlled by different stress conditions. The transformation mechanism is rationalized by following Bain path or Burgers path. As the

experimental results for quartz have been reported mainly under quasi-hydrostatic conditions, here we will only concentrate the situation with low non-isotropic stress components up to 10 %(which is 2-3 GPa between 20 and 30 GPa relevant to most of pressure media [97]). The simulations were carried out using the TS potential [29].
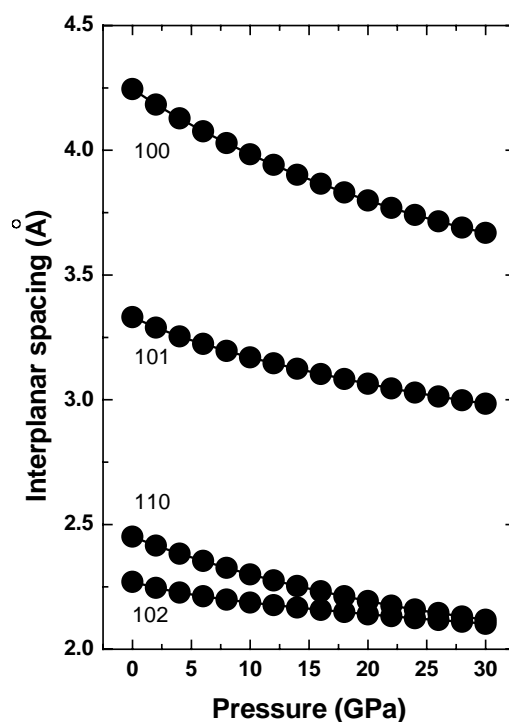

Fig.5.2 Calculated inter-planar distance as a function of pressure, which is showing the two Bragg peaks (110) and (102) converge together above ~20GPa.

5.2 Results

The simulations are started by repeating a recent ab initio calculations by Trave et al [204], pressure was increased in steps of 10 GPa every 0.4 picosecond on a sample of 24 SiO_2 formula units, under hydrostatic conditions, and found a first order transition at 40 GPa. At 60 GPa, an oxygen hcp sublattice was obtained, which contains 2/3 5-fold and 1/3 6-fold coordination for Si atoms. Further hydrostatic compression of this new phase to 90 GPa led to a dramatic rearrangement of the oxygen sublattice (temporally losing the hcp order), which allows for an increased ordering of the Si sublattice so that the resulting structure is entirely composed of octahedrally coordinated Si, and coincides with the $P2_1/c$ crystal structure first proposed for SiO_2

in [54] and recently observed in [39]. Such results are in excellent agreement with ab initio calculations [204] and with available X-ray diffraction data on post-quartz structures [39]. However, when pressure was instead increased in steps of 10 GPa every 2 picoseconds, up to 90 GPa, under hydrostatic conditions, the C2 phase was obtained. The pair analysis [188] shows that the P2$_1$/c crystal structure is with oxygen hcp sublatttice and C2 crystal structure is with oxygen fcc sublatttice.
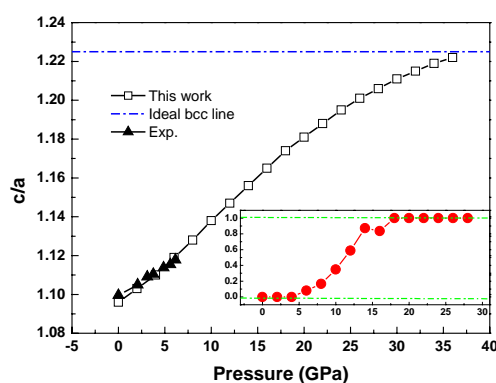

Fig.5.3 Calculated c/a ratios compared with the experiments [208], when c/a equals to $\sqrt{3/2}$ (≈ 1.225) an ideal oxygen bcc sublattice is formed (around 38 GPa). Inset: polyhedral changes for hydrostatically compressed quartz up to 30 GPa. We define a bcc-type atom/polyhedron, which has 6 pairs of 1441 bonds and 8 pairs of 1661 bonds. The equal bonding number is chosen for the pair analysis in order to reduce the arbitrariness coming from different cutoff distances. All the data are obtained assuming oxygen is 14-coordinated (see Sec. 4.2.1).

In order to rationalize the findings of MD simulations, we carried an enthalpy minimization procedure with pressure increasement of 2 GPa up to ~120 GPa. We were monitoring X-ray structure factor, the c/a ratios by symmetry analysis and the polyhedra distributions by so called HA index (pair analysis technique) [41]. First we noted that the calculated X-Ray structure factor, which is showing the two Bragg peaks (110) and (102) converge together above ~20GPa (see Figs. 5.1 and 5.2), which is in good agreement with experimental reports [4]. As c/a serves as an order parameter for bcc sublattice in literature [184], we presents c/a ratio as a function of pressure in Fig. 5.3. The ideal bcc sublattice is reached at 38 GPa, when c/a equals to 1.225. The inset of Fig.5.3 shows that according to the pair analysis, the quasi bcc sublattice has an onset at 6-8 GPa

and increases continuously up to 18 GPa [209], which coincides with the pressure where the Bragg peaks (110) and (102) converge. For short, we will call "hp-quartz" the structure of quartz in the regime of pressure where oxygen is in a bcc sublattice. It is important to note that in Fig. 5.4, where we show a calculation of the diffraction pattern of the oxygen sublattice alone, the line merged by (110) and (102) peaks above 20 GPa can be understood as diffraction line (110) of oxygen bcc sublattice. The peak around 1.48 Å corresponds instead as (002) peak of the oxygen bcc sublattice. Further compression with enthalpy minimization procedure leads to a monoclinic crystalline structure $P2_1$ (Z=12) with a mixture of 50% fcc and 50% hcp oxygen sublattice at 36 GPa and a mixture of 1/3 4-fold coordination and 2/3 6-fold coordination for Si atoms. Imposing a non-isotropic stress component up to 10% along the quartz c-axis simply lowers the transition pressure but yields the same $P2_1$ (Z=12) phase. We failed to obtain the $P2_1/c$ crystal structure (with oxygen hcp sublattice) with this choice of the non-isotropic stress component. The reason we couldn't generate a crystalline phase with oxygen hcp sublattice from hp-quartz may be related to the fact that the orientation of the original quartz cell is not compatible with Burgers path for the oxygen sublattice, as we will discuss it later. Moreover, as the size and shape of this simulation cell (which was chosen as identical to that used in [204]) is not compatible with the predicted K point (1/3,1/3,0) instability [88,89,202].
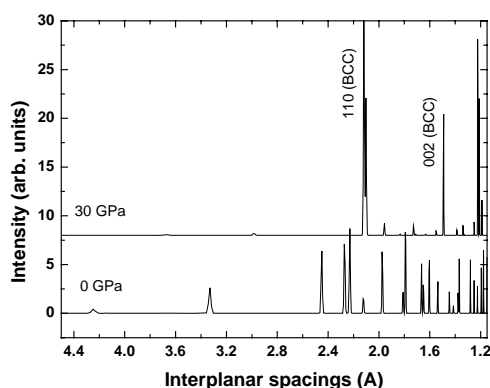

Fig.5.4 Calculated X-Ray structure factors for oxygen atoms only at 0 GPa and 30 GPa, respectively. The converged peak (Figs.5.1 and 5.2) is (110) peak of new bcc cell. The 1.48 Å is (002) peak of new bcc cell.

We therefore decided to repeat the simulation with a new supercell that is compatible with the

K point instability and with all the three post-quartz crystalline phases reported so far (C2, P3$_2$ and P2$_1$/c). A natural option is to follow Binggeli et al. [91, 185] and generate a preliminary supercell with 27 SiO$_2$ formula units based on the bcc conventional unit cell (for short, Binggeli Cell, i.e. see Fig. 5.5). Such a choice makes it easy to control orientation of the non-isotropic stress with respect to the oxygen sublattice (the difference between hp-quartz and hp-cristobalite is shown in Fig. 5.6). For clarity, the relationship between the unit cells of the Binggeli cubic supercell and the primitive unit cell vectors of quartz can be represented by the transformation matrix equation:

$$\begin{pmatrix} 3\vec{e}_x \\ 3\vec{e}_y \\ 3\vec{e}_z \end{pmatrix} = \begin{pmatrix} -2 & -1 & -1 \\ 1 & 2 & -1 \\ 1 & -1 & -1 \end{pmatrix} \begin{pmatrix} \vec{a} \\ \vec{b} \\ \vec{c} \end{pmatrix}$$

where $\vec{e}_x$, $\vec{e}_y$ and $\vec{e}_z$ are unit cell vectors of the underlining conventional bcc sublattice, $\vec{a}$, $\vec{b}$ and $\vec{c}$ are the primitive unit cell vectors of α-quartz, i.e. $\vec{a} = \left(a/2, \ -\sqrt{3}a/2, \ 0 \right), \vec{b} = \left(a/2, \ \sqrt{3}a/2, \ 0 \right)$ and $\vec{c} = \left(0, \ 0, \ c \right)$.

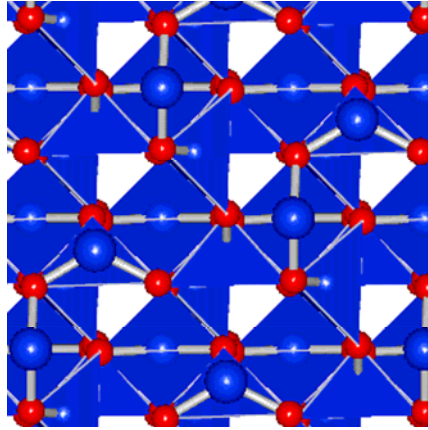Fig.5.5 Binggeli cubic cell relaxed at 36 GPa by the new developed potential.

The supercell is compatible with C2 and P3$_2$, but not yet with P2$_1$/c (Z=6). In order to be compatible with the possible resulting P2$_1$/c (Z=6), we employed a larger supercell consisting 216 SiO$_2$ formula units (2×2×2 Binggeli Cell) and applied an enthalpy minization procedure up to ~50 GPa. With this cell, we found that quartz transformed into two phases with the same space group (P3$_2$), but with different silicon coordinations at 38 GPa and at 46 GPa, which is consistent

with what Wentzcovitch et al. [202] found with ab initio methods at 33 GPa and 40 GPa, respectively. The structural parameters, as well as the coordination, of the two phases are in excellent agreement with first-principles calculations. We tested the stability of the relaxed phases (quartz and $P3_2$) by heating the samples to room temperature at all pressures. We found that quartz remains up to 30 GPa. From 32 GPa to 36 GPa we found the $P3_2$ (Z=9), and then between 38 GPa and 44 GPa we found that the system transforms into an amorphous phase (we define a phase as amorphous if the space group analysis yields a P1 space group with Z=216, with tolerance ~0.1 Å). Heating the $P3_2$ phase to 1000K also yields an amorphous. It is important to realize that the oxygen sublattice in $P3_2$ phase is neither fcc nor hcp, thus it seems that this phase is the result of the dynamical instability at K point (1/3,1/3,0) [202], and not of a concomitant shear instability of the oxygen sublattice similar to the one discussed for cristobalite in the previous chapter. The structure factor of the resulting amorphous obtained at 300 K and 40 GPa is shown in Fig. 5.7. The spectrum is very similar to the one observed experimentally for compressed glass at the same pressure [66]. The coordination analysis shows the amorphous is a mixture 4-fold and 6-fold coordinated silicon with a small amount of 5-fold silicon. The pair analysis shows that the amorphous is a mixture of fcc and hcp oxygen sublattice.
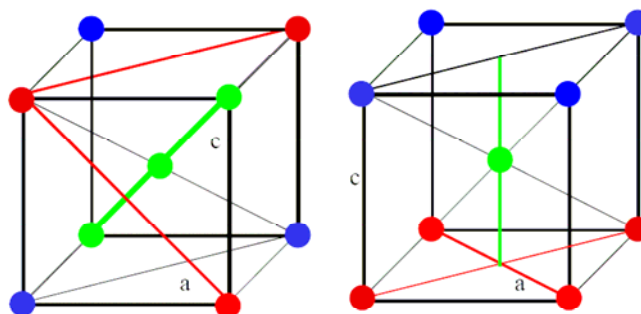

Fig. 5.6 The relationship between the orientations of oxygen bcc sublattice vectors and hp-quartz unit cell vectors (left) and hp-cristobalite unit cell vectors (right).

We then proceeded and studied the supercell consisting 216 SiO_2 formula units ($2\times2\times2$ Binggeli Cell) at different non-isotropic stress conditions, starting from hp-quartz at 30 GPa. As expected, a C2 crystal with oxygen fcc sublattice is obtained under a small tensile component along *[100]* [i.e. (27 GPa, 31.5 GPa, 31.5GPa) along the three Cartesian directions], along so

called Bain path. The Burgers path is activated at 36 GPa under a small compressive component along *[100]* [i.e. (39.6 GPa, 34.2 GPa, 34.2GPa)], which led to a monoclinic phase $P2_1$ (Z=6) with oxygen hcp sublattice. The phase has silicon in 1/3 4-fold and 2/3 6-fold coordination and transformed into another monoclinic phase with 2/3 5-fold and 1/3 6-fold silicon but with the same space group under hydrostatic pressure at 90 GPa. The $P2_1/c$ phase is obtained in our calculations by further compressing hydrostatically the $P2_1$ (Z=6) phase up to 120 GPa and 300 K (or 150 GPa and 0 K). The $P2_1/c$ has 100% oxygen hcp sublattice and 6-fold silicon coordination, and can be retained when recovered to 0GPa. The parameters at 0GPa are in excellent agreement with recently reported ab initio calculations [210]. At this point, it is important to remark that the present work differs with respect to the study by Badro et al., where a phase with 5-fold Si coordination was found, as the non-hydrostatic conditions are here imposed along different and well-defined directions relative to the oxygen sublattice.
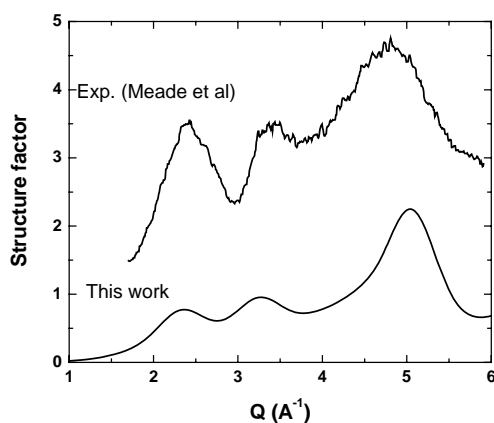

Fig.5.7 Comparison between the structure factor calculated at 40 GPa and the experimentally determined structure factor for compressed glass (at 40 GPa) [66]. The calculated structure factor has been broadened with an intrinsic width 0.25 Å.

5.3 Discussions

C2 and $P3_2$ have been assigned to quartz-II historically by theory according to previous simulations [200,202,203]. As shown in Figs. 5.1 and 5.2, hp-quartz shows the convergence of the (110) and (102) peaks, which was reported as an experimental evidence for quartz-II [4]. The new lines around 3.7 and 2.7 Å [92] have been suggested to originate from a different post-quartz
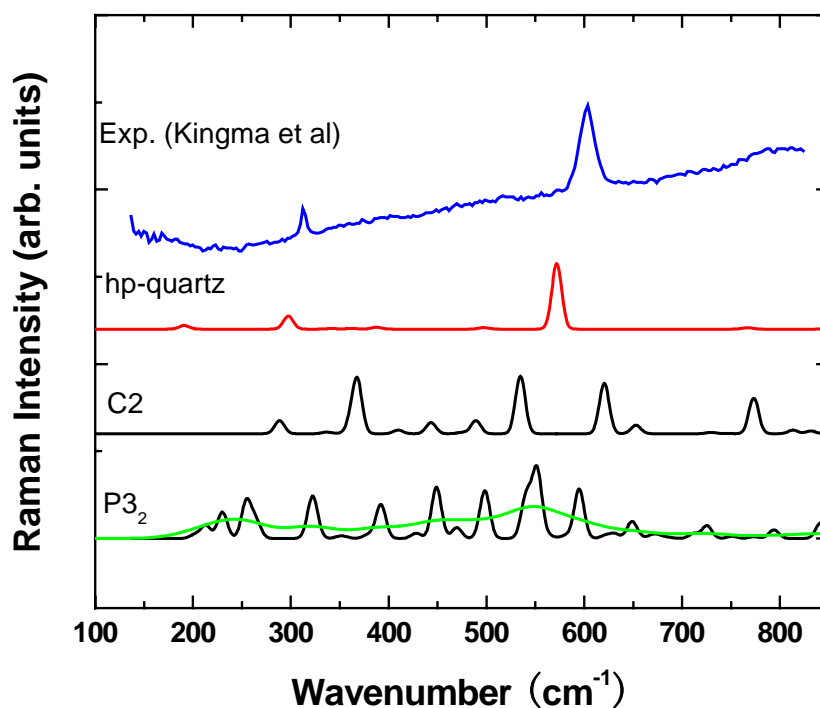
Fig.5.8 Calculated Raman spectra of hp-quartz, C2 and $P3_2$ at 24 ± 2 GPa, compared with experiments for quartz II at 24.5 GPa[38].

crystalline phases by Kingma et al. [92]. It is therefore reasonable to propose hp-quartz as a candidate for quartz-II. Because the comparison of calculated diffraction patterns for these model structures with the experimental patterns is problematic and does not yield a unique solution, Raman spectra, which have also been measured across the quartz collapse transition, are then calculated for all the possible phases, based on density functional perturbation theory [211]. Ab initio Raman caculations of the spectra of quartz and other tetrahedral silica phases at ambient pressure are known to yield excellent agreement with experiments [153]. In Fig. 5.8, we compare our calculated Raman spectra for all the three different phases (hp-quartz, C2 and $P3_2$) obtained with the same approximation used in [153], with experimental Raman spectra corresponding to quartz-II. It is clear that the C2 and $P3_2$ phases do not reproduce the Raman spectra of quartz-II. On the other hand, it seems that the spectrum calculation of hp-quartz is in excellent agreement with experiments. We therefore argue that the small changes observed with X-Ray diffraction across the quartz to quartz-II transition are simply a consequence of the "symmetrization" of the

oxygen sublattice in quartz at high pressure.

Our simulations offer some insights into the mechanisms leading to the amorphiztion of quartz. The amorphous sample in our simulations is characterized by a close packed oxygen sublattice (mixture of fcc and hcp), but appears under hydrostatic conditions from a phase ($P3_2$) where the oxygen packing is not complete. On the other hand, oxygen close packing is readily achieved directly from quartz with small non-hydrostatic components. We thus speculate that the amorphous phase produced experimentally from quartz results from the collapse of the oxygen sublattice into close packed arrangement induced by local inhomogeneous stress fields in the sample. This is consistent with the observation that the appearance of the amorphous phase is enhanced by the non-hydrostaticity of the pressure medium [7,179].

5.4 Conclusions

We have presented a comprehensive understanding of pressure-induced collapse of quartz based on extensive molecular dynamics simulations and enthalpy minimization, with the TS potential, and by performing ab initio Raman spectra calculations. We argue that quartz-II is not a distict phase, but simply a partial symmetrization of quartz. Pressure-induced (bulk) amorphization (in quartz) can be understood based on oxygen packing arguments. A pathway to transform quartz into the $P2_1/c$ phase is also shown to be connected with the oxygen sublattice packing.

Chapter 6

Compressed Silica Glass

By means of molecular dynamic simulations, the structural properties of compressed glass by cold compression at room temperature and by quenching the liquid are compared at selected pressures. The noticeable differences found below 10 GPa between the two results are interpreted in the context of the experimentally reported temperature-induced densification and of the speculated occurrence of a first-order transition between two distinct polyamorphs. Calculated X-Ray and neutron structure factors agree well with available experiments, and indicate that structural differences between annealed and cold-compressed forms take place at distances of 3.5-4 Å. In contrast, short-range order (atomic coordination, bond length and angular distribution functions) is identical in the two forms of silica glass. We conclude that the compressibility maximum does not require changes the tetrahedral network topology. We provide a unified picture of the compression mechanisms based on the pressure-induced appearance of unquenchable fivefold defects and find them to be responsible for the reduction of the mechanical strength and for permanent densification.

6.1 Introduction

SiO_2 glass is an important material in technological applications such as optical fibers and transistors, it is present in the Earth crust and mantle, and it is a prototypical example of a network-forming material like water. Contrary to ordinary solids, which are normally known to harden by compression, the compressibility of SiO_2 glass has a maximum at about 2-4 GPa [11-15], and its mechanical strength shows a minimum around 10 GPa [16]. At this pressure, the compression of silica glass undergoes a change from purely elastic to plastic, and samples recovered from above 10 GPa are found to be permanently densified [17-20]. As first noted by Roy and Cohen [23,24], recent in-situ measurements have confirmed that densification can also take place at lower pressures provided the glass is annealed to several hundred degrees [22,25-27].

The scope of this chapter is to elucidate the microscopic mechanisms of densification and plasiticity, based on molecular dynamics.
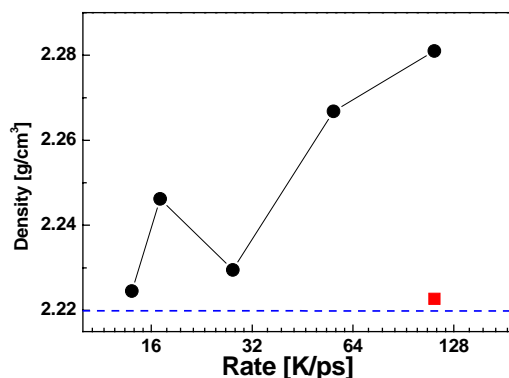

Fig. 6.1 Density after annealing vs cooling rate. Full circles: annealing at 0 GPa. Square: annealing at –2 GPa followed by cold recovery to 0 GPa. The horizontal line is the experimental value (2.22 g/cm^3) [17]

6.2 Preparation of Silica Glass at 0 GPa

With the TS potential a glass sample consisting of 192 SiO_2 formula units was generated by MD by quenching a liquid configuration from 3000 K down to 300 K at different rates. The structural properties of simulated glass samples quenched at ambient pressure are known to depend strongly on the quenching rate [79]. Fig. 6.1 shows the dependence of the final density of our samples on the quenching rate. A quenching rate of 14 K/ps is found to be enough to yield a glass sample with density in excellent agreement with the experimental value. Because samples generated with faster quenching rates systematically yield denser samples, a glass sample was obtained by first quenching with a fast rate but at negative pressure and then equilibrating at room pressure. This procedure yields a sample with density comparable to that of the slowest quenching rates at ambient pressure, but at a considerably faster rate, and thus with a considerably lower computational effort. This procedure to generate glass samples at ambient conditions was not explored further, but it is a route worth pursuing in future studies.

6.3 Temperature-induced densification below 10 GPa

The densification has been frequently connected with the hypothetical occurrence of

"polyamorphism" in amorphous silica, i.e. with the possibility that two distinct (e.g. by density) forms of amorphous silica could exist, separated by a first-order transition line, similarly to the low-density / high-density polyamorphism observed in amorphous ice [212]. That such a phenomenology could be relevant also for silica glass was suggested, for example, by molecular dynamic simulations [69]. Evidence for polyamorphism in silica glass is still controversial however. Mukherjee *et al* reported an apparently first-order phase transition at 3.6GPa and 680 °C [26], and El'kin *et al* indicated at least two pressure-induced phase transitions by in situ measurements [27]. However, more recent X-ray diffraction experiments support the existence of a single stable high pressure SiO_2 glass form, with no abrupt transitions [22]. The controversy stems from the very high viscosity of silica glass at ambient temperature and low pressure, which introduces a strong history dependence and hinders a proper comparison of the results obtained with different preparation and compression methods. The temperature-induced densification, for example, was shown to obey a sluggish logarithmic kinetics [15].

Addressing such issues with molecular dynamics (MD) simulations, where time scale rarely exceeds a few nanoseconds, would look, in this respect, meaningless. Yet, while MD would be totally inappropriate to study the kinetics of densification at the moderate temperatures considered in experiments, the pristine cold-compressed and the annealed densified forms of silica can be obtained by MD, separately, by following more amenable routes than the one followed experimentally. For example, the densified form can be obtained, in MD, by heating the glass up to the point where atomic diffusion becomes non negligible even on a nanosecond time scale. A similar procedure has been used to generate by MD densified amorphous ice samples, which displayed very good agreement with the available experimental data on ice [213,214].

To this aim, two different compression routes are employed in MD simulations: a cold compression route consisting of increasing pressure slowly at ambient temperature at a rate of 0.3 GPa/ps, followed, at each pressure, by an equilibration time of 20 ps, and a "quench-from-the-melt" procedure with a reasonable slow quenching rate, whereby the compressed glass was obtained by slow cooling of a compressed sample from a temperature where atomic diffusion is observable on the time scale of the MD simulation. By comparing the present results with the available experimental data on compressed glass, it is shown that the samples

obtained with the two procedures are representative of the cold-compressed and densified forms of glass, respectively, and the two microscopic structures is then analyzed by searching for differences in the local structural order at short and medium range [215].
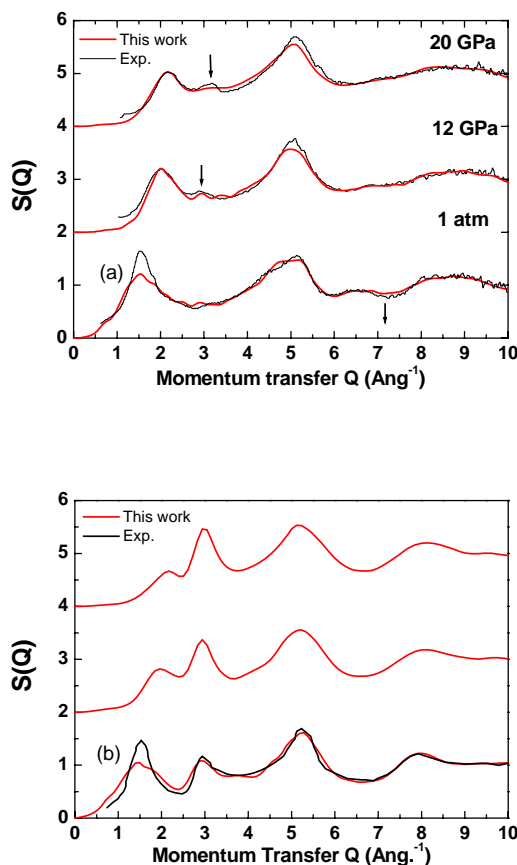

Fig.6.2 Calculated X-Ray structure factor (upper) and neutron scattering factor (lower) at 0 GPa, 12 GPa and 20 GPa, compared with experimental X-Ray diffraction [22] and neutron scattering data [140].

The temperature-induced densification of compressed silica is firstly analysed by considering temperature-induced changes in the X-ray structure factor and neutron scattering factor at constant pressure. The calculated structure factors agree well with the experimental data [22], as shown in Fig. 6.2. The present calculations also reproduce very well the pressure dependence of the position of the FSDP, as shown in Fig. 6.3. In particular, the results on samples quenched from the melt differ, with respect to the results of cold compression, by an amount very similar to the experimental difference between temperature-densified and cold-compressed samples, indicating

that the procedure of quenching the sample from a highly diffusive state yields a final state similar to the one obtained experimentally at milder temperatures. The difference between densified and cold-compressed samples reaches in both cases a maximum at about 6 GPa. The inset of Fig. 6.3 shows the calculated behavior of the second peak (at about ~3.0 Å^{-1}) in the structure factor of silica glass. This peak is very weak in the x-ray structure factor due to a cancellation of terms, but appears clearly in the neutron structure factor [149]. Its pressure dependence is extremely weak up to 10 GPa, indicating that the microscopic structure of glass at length scales of the order of 2 Å is unaffected in that pressure range. In Fig. 6.4 (a) we show the difference $\Delta V(P)$ between the SiO$_2$ unit volume before and after the heating, as a function of pressure. The experimental data of Trachenko et al. [25] are given in their paper in relative terms, as $-\Delta V(P)/V_{CC}(P)$, where $V_{CC}(P)$ is the volume obtained with cold compression. The present (calculated) value of $V_{CC}(P)$ was used to obtain the experimental $\Delta V(P)$. Data from the experiments by Inamura et al. are obtained from the position of the FSDP in their X-Ray structure factor [22], assuming that the peak position is linearly related to the density as in densified glass [216]. The experimental data are compared with the calculated values of $\Delta V(P)$, as obtained from cold compression and from quench from the melt at the same pressure P. For increasing pressure the volume difference $\Delta V(P)$ shows a maximum around 4-6 GPa, in good agreement with experiments [22, 25], and also with the results on the position of the FSDP shown in Fig. 6.3. The results of Figs.6.3 and 6.4 suggest that at pressures between 0 and 10 GPa a ``thermodynamical'' minimum (within the realm of disordered phases) is not reached upon "fast" cold compression. This is consistent with the results of strain-gauge experiments, which show that the volume of cold compressed samples relaxes to higher densities with a very slow logarithmic time dependence, confirming the metastable, long-lived nature of the samples obtained by cold compression [15]. Such a metastable behaviour becomes less pronounced at higher pressures, where, in fact, the densification kinetics is known to be much faster [15]. As shown later in this chapter, the faster kinetic is tightly associated to the appearance of network defects consisting in five-fold coordinated silicon atoms, above 8 GPa. Appearance of such defects activates atomic diffusion and lowers kinetic barriers for the reorganization of the network at intermediate distances.
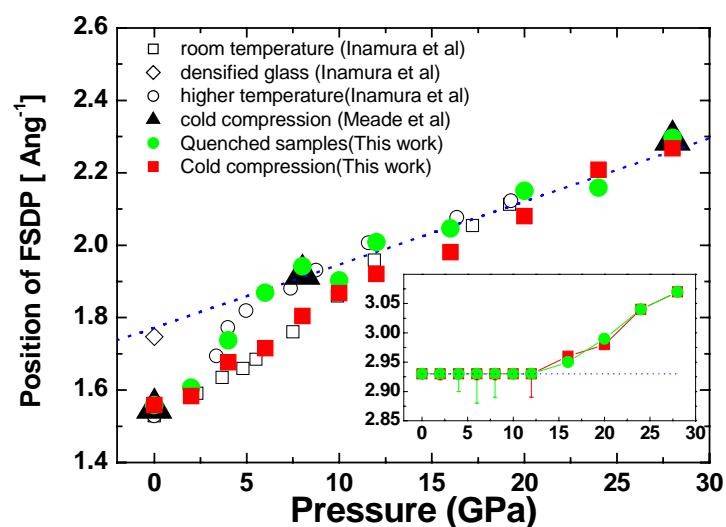
Fig.6.3 Position of the FSDP in the calculated X-Ray structure factor for cold-compressed and annealed glasses, as a function of pressure, compared with experiments [22]. Inset: position of the second sharp diffraction peak in the calculated neutron structure factor, as a function of pressure.

Inherent in the above considerations on the stability of two distinct forms of glass is the argument that the annealed state is thermodynamically more stable than the metastable state reached by fast cold compression. Fig. 6.4(b) shows the enthalpy difference between the annealed and the cold-compressed glasses, calculated at low temperature (300 K). The enthalpy of the annealed phase is always lower at least for the lowest cooling rates, at all pressures but for the very low-pressure region where the two phases are virtually identical (at 0 GPa they are identical by definition). This confirms that the cold-compressed phase is thermodynamically unstable towards the annealed phase, which can therefore be assumed to represent the room-temperature thermodynamical ground state within the realm of the disordered phase. Fig. 6.4(b) also shows that annealing causes an increase of the heat of formation of the glass up to about 0.12 eV/SiO_2 (at 8 GPa), which is even larger than typical heat of formation differences between tetrahedral crystalline phases, but smaller than the differences between tetrahedral and octahedral phases [130]. The current finding that annealed samples are thermodynamically more stable than cold-compressed ones at all pressures is in contrast with the result of Lacks [69], where a first-order transition between a low-density and a high-density form was proposed on the basis of
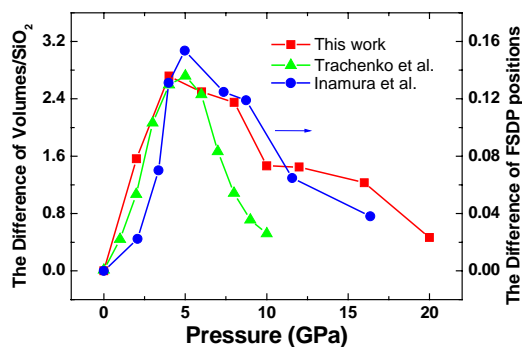
(a)
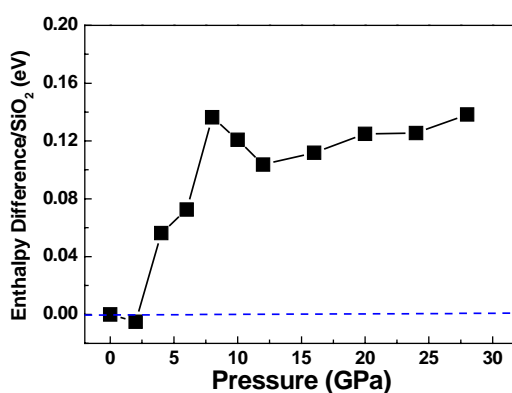
(b)

Fig. 6.4 (a) Volume difference between cold-compressed and annealed glasses, compared with experimental data up to 10 GPa [25]. Direct measurements of densities are not available on a wider pressure range, comparisons to the shifts of FSDP of X-Ray diffraction measurements [22] are shown (a linear relationship between shift and density is assumed as in Ref. [216]). (b) Enthalpy difference between the cold-compressed and annealed glass.

calculated enthalpy differences. The difference can be traced to the fact that in Ref. [69] enthalpies for the two forms were calculated on the basis of cold-compression and cold-decompression simulations, while evidence from our work and from Ref. [15, 22-24] suggest that the true thermodynamical minimum can only be reached by annealing. The equations of state (we will show it in Fig. 6.8) and the position of the FSDP of the annealed glass indicate that there is no abrupt "thermodynamic" transformation between distinct amorphous forms with pressure.

The structural differences between annealed and cold compressed forms of silica was then analyzed, in the hope of obtaining some insights into the microscopic reasons that lead to densification. The Si-O bond length remains identical to the zero pressure value of 1.61 Å up to at least 10 GPa (Fig. 6.5), in good agreement with the X-Ray diffraction measurements $(1.59 \pm 0.01\,\text{Å}$ at 0GPa and 8GPa)[66]. The Si-O coordination number is also essentially fixed to the value of 4, up to 10 GPa, with a percentage of five-fold defects ~ 4 % at the highest pressure of 10 GPa (Fig. 6.6). This is consistent with a number of different experiments [66,217,218], which provide no evidence for coordination different from 4 below 8-10 GPa. Notice that this is different from the behavior of liquid silica, where the large compressibility has been explained based on the appearance of coordination defects [67].

Susman et al. [140] suggested that glass densification could be explained by a reduction of the Si-O-Si angle (or Si-Si bond length, if the Si-O length is fixed). Fig.6.7(a) shows the distribution of the Si-O-Si angles at 6 GPa for annealed and cold compressed glass. No noticeable difference is found between the two distributions. The fact that we do observe densification rules out the reduction of the Si-O-Si angle as a microscopic fingerprint of densification. We also searched for differences in the ring distribution but found that at all pressures below 10 GPa, the ring size in densified and cold compressed glass has an average value around 6.58 with little fluctuations between samples. In order to obtain a clearer understanding of the length scale at which structural difference take place, the behaviour of the modified total pair correlation function $4\pi r^3 / 3(n(r) + 1)$ is shown in Fig. 6.5(b), where $n(r)$ is the total number of SiO_2 formula units within a radius r from any given Si atom, averaged over the tagged atom. At large radii the function tends to the volume per formula unit of the system. At distances shorter than 3.5 Å the curves for annealed and cold compressed glass are identical, which confirms their structural similarity at short range. The structural changes responsible for the density difference appear to occur in the short radius interval between 3.5 and 4 Å, above which the two curves show no noticeable differences in their approaching the asymptotic limit given by their respective densities. What Fig. 6.7(b) suggests is that the microscopic changes responsible for densification take place in a well-defined region of radius, which is consistent with the length scale indicated by the position of the FSDP.
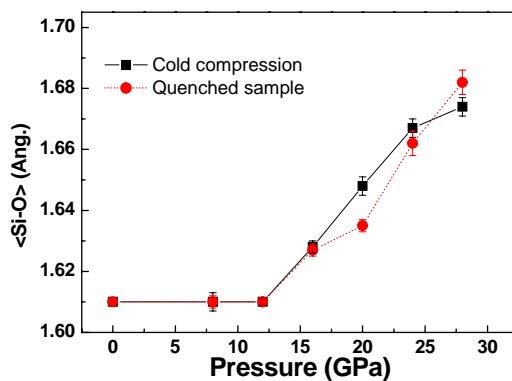
Fig.6.5 Average Si-O bond length as a function of pressure. The average is taken over the Si-O pair distribution function with a cutoff radius of 2.1Å. The error bar was evaluated by changing the cutoff distance with 0.1 Å.
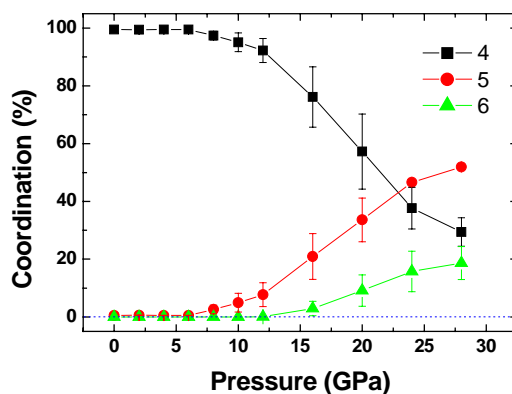

Fig.6.6 Percentages of Si atoms coordinated four (squares), five (circles), and six (triangles), to oxygen, as obtained by cold compression simulations (same results were obtained on samples quenched from the liquid).

In summary, the features of the temperature-induced densification of compressed glass in the pressure range 0-10 GPa, where the glass is known to retain a tetrahedral structure, can be reproduced by the new developed potential. It is shown that the annealed, densified form of glass corresponds to the thermodynamical minimum, within the realm of disordered phases, at all considered pressures. No abrupt changes in the properties of the annealed glass have been found, indicating that ideas of a possible polyamorphism, i.e. of a first-order transition between two distinct phases, may have to be revised for silica. It is found that cold-compressed and annealed glasses have similar short-range order (atomic coordination, bond length and angle distribution

function) and start to differ at distances of 3.5-4 Å. It is worthwhile to study in more details the microscopic nature of the structural difference between the two forms.
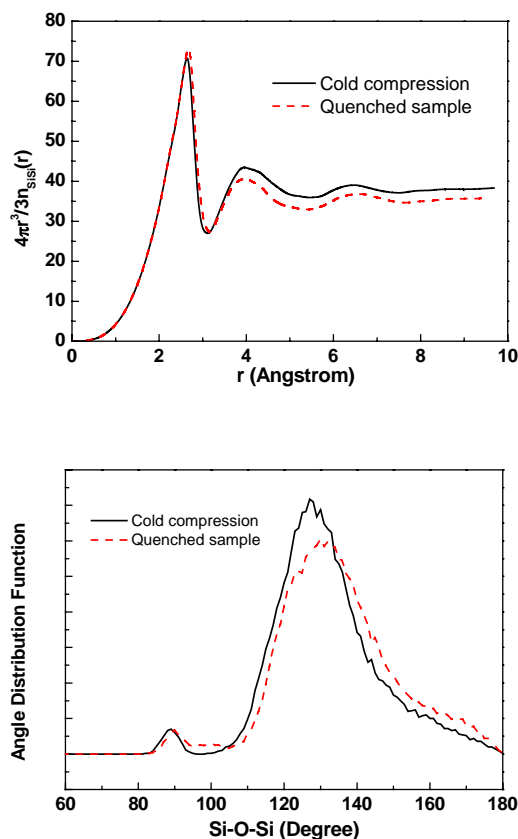

Fig. 6.7 Si-O-Si angle distribution function at 6 GPa for cold-compressed and annealed samples (upper); radial unit volume $4\pi r^3 / 3(n(r) + 1)$ vs radius (lower).

6.4 "Cold" Compressed Silica Glass

As mentioned above, compression of silica glass at room temperature leads to an unexpected mechanical weakening, with a reported minimum of the yield strength around 10 GPa [16], where the mechanical response changes from purely elastic to plastic, as first noted by Bridgman [17]. Samples recovered from pressures lower than 10 GPa appear indistinguishable from the original material, while compression above 10 GPa results in the recovery of a densified amorphous polymorph, with densities 10-20 % higher than the density of the starting material [17-20]. The compressibility of silica glass in the elastic region below 10 GPa is also anomalous, as it shows a maximum at about 2-4 GPa [11-15]. Despite the large pressure difference between the onset of the

two anomalies, microscopic theories have traditionally attempted to explain both anomalies with a single model, typically consisting in the pressure induced appearance of coordination defects triggering the activation of local rebonding events [25,71,72,139]. In particular, local displacive mechanisms involving six-fold coordinated Si defects have been proposed earlier on as an effective microscopic path to compression and densification [210]. Such models are seriously questioned however by the lack of evidence for coordination defects below 8-10 GPa (i.e. where the compressibility anomaly takes place), in NMR [220], X-Ray diffraction [66], Raman [217] and Infrared spectroscopy [218] experiments. Moreover, all models proposed so far for densified glass obtained from cold decompression at room temperature [71-74], contain sizable amounts of coordination defects, which are also not seen in experiments [20, 75]. In order to overcome this problem, models have been introduced which explicitly forbid coordination changes. While some of these models correctly reproduce the compressibility maximum [143], they obviously cannot account for the cold densification process, as this is known to be crucially affected by coordination defects [66,217,218]. More recently, an improved three-body potential has been successfully used to reproduce the elastic-to-plastic transition in shocked glass [145], however, more than 95% of the Si atoms were reported to be still in fourfold coordination at pressures exceeding 20 GPa, which is in contrast with the experimental observation of substantial coordination changes above 10 GPa [66]. Here we provide, using an improved interatomic potential for SiO_2, a unified theoretical model based on the pressure-induced appearance of five-fold coordinated silicon above 10 GPa, which describes all the observed phenomenology. Previously employed atomistic models for SiO_2 have been recently shown to fail to reproduce pressure-induced coordination changes in liquid SiO_2 [29], and some of them explicitly exclude them [20,143].

Fig. 6.8 shows the densities obtained as a function of pressure for the two cases. The two compression mechanisms lead to different results for pressures below 10 GPa, but start to converge to similar structures and densities above 10 GPa. This indicates that below 10 GPa a thermodynamical minimum is not reached upon cold compression at least on the time scale of several tens of picoseconds. This is in agreement with experimental data [15,22,25], where temperature annealing is shown to be necessary to bring the system to a state of higher density and, presumably, lower enthalpy, at pressures below about 10 GPa. Experiments also indicate that the

kinetics to reach thermodynamic equilibrium has a faster rate for increasing pressure [15,25], in agreement with our finding that at 10 GPa the two compression routes start to converge to similar results.
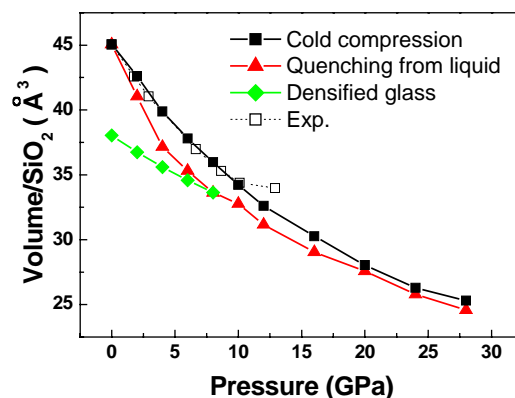

Fig.6.8 Equations of state of SiO_2 glass as obtained by cold compression (black squares), isobaric quenching from the liquid (red triangles), and cold decompression from 10 GPa (green diamonds). Experimental data obtained by cold compression (empty squares) are from Ref. [13], using our value (2.2295 g/cm^3) for the ambient pressure density (data in [13] are scaled to the ambient pressure volume).

A microscopic analysis of the average Si-O coordination number (Fig.6.6) shows that the silicon coordination number deviates significantly from the ideal value of four, characteristic of a perfect tetrahedral network, only above 10 GPa, in agreement with experiments on compressed glass [66,217,218]. It is verified that the network topology also did not change, up to 10 GPa. Such a rigidity of the network explains the elastic recovery of the samples below the threshold pressure. The calculated compressibility of the glass compressed up to 10 GPa displays a maximum at about 3-5 GPa (Fig.6.9), in fair agreement with experimental data on the compressibility [12-13,15] and on the sound velocity [14]. It's therefore concluded that the compressibility maximum is not a consequence of a change in the network topology -- as it would result, for example, in the case of an underlying kinetically hidden phase transition [68] --   nor of a change in Si coordination, as argued in Ref. [71].   Rather, it is the consequence of a continuously increasing number of Si-O-Si plane normal reversals (Fig.6.10), as already suggested by Huang and Kieffer [143], and first hypothesized by Vukcevich [11].
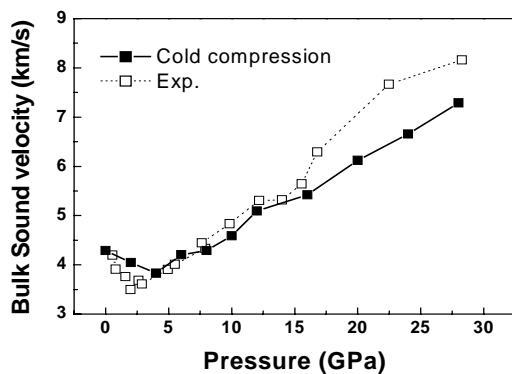
Fig.6.9 Bulk sound velocity as a function of pressure as obtained by cold compression simulations. The bulk sound velocity was calculated from the compressibility determined by small (1-2%) finite strains. Experimental data are from Ref. [14]
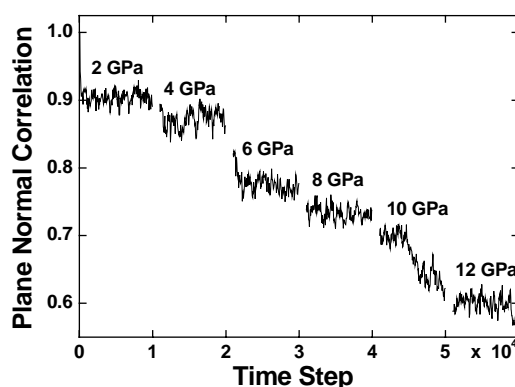

Fig. 6.10 The time-dependent average Si-O-Si plane normal correlation was calculated as in Ref. [143] by definining the vector normal $\hat{n} = (\vec{R}_1 \times \vec{R}_2)/|(\vec{R}_1 \times \vec{R}_2)|$, with $\vec{R}_1$ and $\vec{R}_2$ the Si-O vectors in the Si-O-Si plane, and constructing the time correlation function $C(t) = \langle \hat{n}(t) \cdot \hat{n}(0) \rangle$, where the average $\langle ... \rangle$ is taken over the different Si-O-Si in the sample. The time step was set to 0.72 fs throughout this work. The time origin ($t=0$) coincides with the last configuration of the 0 GPa simulation. For increasing pressure, a continuously increasing number of Si-O-Si planes switch their plane orientation, as already observed in [6], leading to a decay of the correlation function.
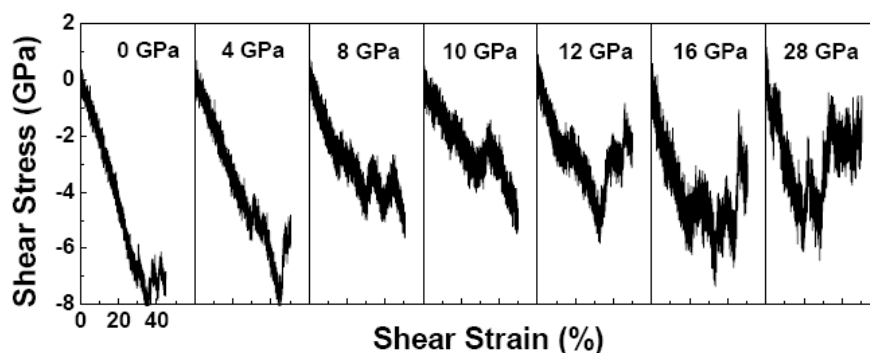
Fig. 6.11 Shear-stress versus strain curves obtained by subjecting the samples to strain rates of 10^{10} s^{-1}, at room temperature and different pressures.

Compression above 10 GPa results instead in important changes in the network topology and in irreversible densification. Topological changes of the network are tightly connected with the appearance of five-fold Si-O coordination defects (see Fig.6.5). The idea that coordination changes could be responsible for compression and densification of glasses above a critical pressure has been originally put forward by Stolper and Ahrens [219]. They suggested a displacive mechanism leading to the spontaneous formation of six-fold coordinated Si, which -they argued-could provide a microscopic path to the network reorganization required to obtain a densified recovered sample.   The present simulations show that six-fold coordinated Si only appears in significant amounts above 20 GPa, while coordination changes are essentially purely five-fold between 10 and 20 GPa. We thus infer that the plastic behaviour observed in glass above 10 GPa is a consequence of the pressure-induced appearance of five-fold defects. Five-fold defects are known to be responsible for the diffusivity maximum in silicate melts [76-77]. They have been also advocated among the possible transition states in the atomic migration mechanisms responsible for the high temperature growth of quartz from glass [70]. It seems that five-fold-Si activated diffusion is responsible for the minimum of the glass yield strength observed at about 10 GPa in mechanical strength measurements [16]. In order to corroborate such hypothesis, we carried out MD calculations of the yield strength of our samples by subjecting them to time-dependent shear strains, increasing at a constant rate, at different pressures. Due to the intrinsic time scale limitations of our MD approach, our strain rates, 1% per 1 ps, are much faster than any experimental rate. However, the stress-strain curves shown in Fig. 6.11 indicate not only

a qualitative agreement with the position of the observed minimum of the yield strength, but also, quite surprisingly, with the absolute values of the yield strength, indicating that the microscopic processes responsible for the strength of compressed glass can be activated on the time scale of our MD simulations. However, it cannot be excluded that other long-term processes longer than the time scale of our MD simulations may also contribute to the observed minimum. Fig. 6.12 shows that the plastic behavior is tightly correlated with the appearance of five-fold coordinated defects. Minimal six-fold coordination defects have been detected in the simulations of Fig. 6.12, indicating that octahedral units such as those proposed in Ref. [25] do not play any role in the plastic behavior of silica glass at the onset of densification. In order to support our speculation that fivefold defects drive the plastic events, we show in Fig. 6.13 the mean-squared displacement of Si atoms, separating the contribution due to Si atoms that have remained fourfold coordinated throughout the simulation from that due to Si atoms that have experienced a fivefold instantaneous coordination for at least one time step during the run. In order to remove the component of the elastic displacement due to the change in shape of the simulation cell we calculated all displacements in scaled coordinates, as defined in Ref. [134]. By doing so we highlight the component of the atomic displacements due to internal elastic relaxation and/or to bond breaking and reforming, which is responsible for the plasticbehavior. The results shown in Fig. 6.13 indicate that five-fold coordination enhances local rebonding and relaxation, and therefore plasticity.

The existence of fivefold coordination defects in silica glass is consistent with several experimental data. X-ray diffraction experiments indicate that the Si-O bond length elongates starting from a pressure of about 8–10 GPa [66]. Together with the lack of evidence for six-fold coordination below 17 GPa, from infrared experiments [218], this implies the appearance of a sizable proportion of fivefold defects between 10 and 17 GPa. Moreover, our simulations show that the appearance of fivefold defects is accompanied locally by the formation of small rings in the network, with units similar to those reported in electronic structure calculations [221]. For example, the number of three-membered rings doubles between 10 and 16 GPa. Such an increase is consistent with the interpretation of in situ high-pressure Raman experiments (Fig. 6.14) [217,222]. Finally, x-ray experiments on the analog system GeO_2 glass indicate that in the pressure

window 6–10 GPa Ge is fivefold coordinated to oxygen on average [223]. This could be equally

accounted for by an equal proportion of fourfold and sixfold coordination, however.
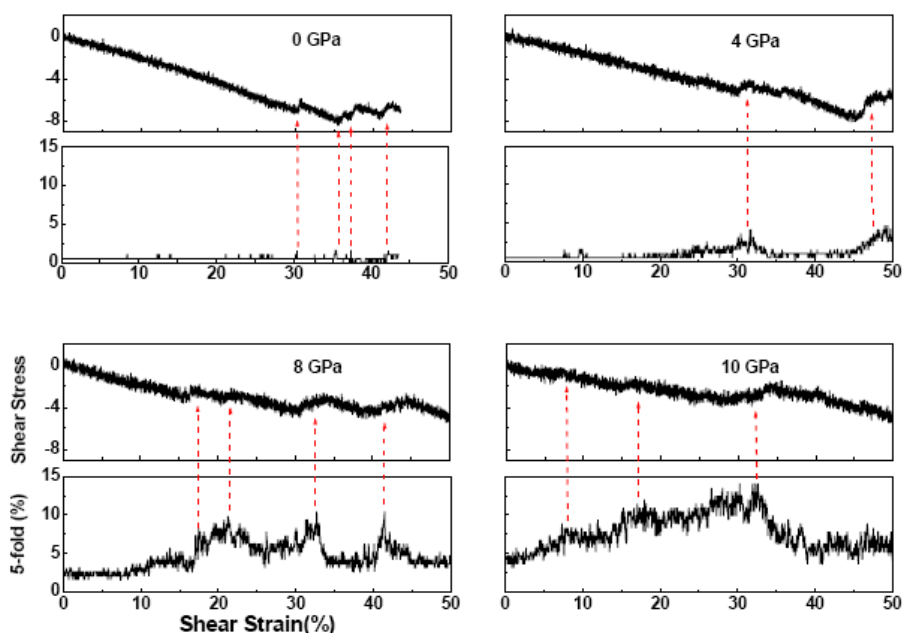

Fig.6.12 Percentages of five-fold coordinated Silicon during the runs described in Fig. 6.11. The

stress versus strain curves are those of Fig. 6.11 and are repeated here for clarity.   As in Fig. 6.10,

the time step is 0.72 fs. Notice the peaks in the concentration of five-fold coordinated Si in

connection with the onset of plastic events, as signalled by the sudden decrease of the shear stress.

At 0 GPa the concentration of five-fold defects during such events is small but non negligible (at

least 3 simultaneous occurrences out of 192 Si atoms).

Simulated glass samples recovered by cold compression from 10-28 GPa are found to have

densities in very good agreement with experimental data on densified glass, as shown in Fig. 6.15.

Both the threshold pressure and the range of densities agree well with the experimental data

[17-20]. It is important to stress that previous theoretical models for densified glass either

contained unrealistically large concentrations of coordination defects [71-74], or had to be

obtained by annealing [20], or by forcing four fold coordination [20, 144]. The capability of the

new developed interatomic potential to produce defect-free densified glass (within 1-2%) by

following the experimental route, is a further illustration of its accuracy.

In conclusion, the observed transition from elastic to plastic behaviour observed in

compressed glass, and the permanent densification, are due to the appearance of five-fold coordinated Si defects above a threshold pressure of about 10 GPa. Defects activate atomic diffusion and are responsible for plastic behaviour. NMR spectroscopy would be ideally suited to verify our findings experimentally, but experiments would have to be carried out in situ at high pressure, as five-fold defects are not quenchable to ambient conditions. It is also confirmed that the compressibility anomaly is a purely elastic phenomenon that does not require topology changes or hidden phase transitions.
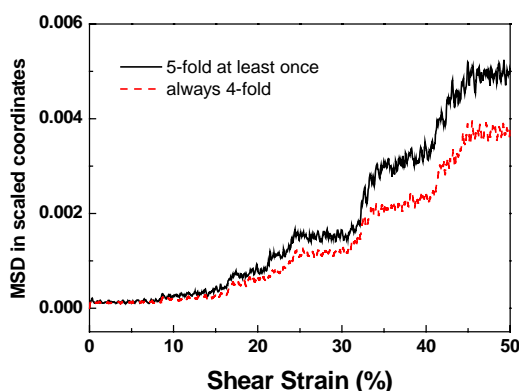

Fig.6.13 Mean squared displacement (MSD) of silicon atoms in scaled coordinates during the run descibed in Fig.5, at 8 GPa. Solid line: MSD averaged over those Si atoms that have been five-fold coordinated at least once during the run (75 atoms out of 192). Dashed line: MSD averaged over Si atoms always in four-fold coordination (117 out 192).
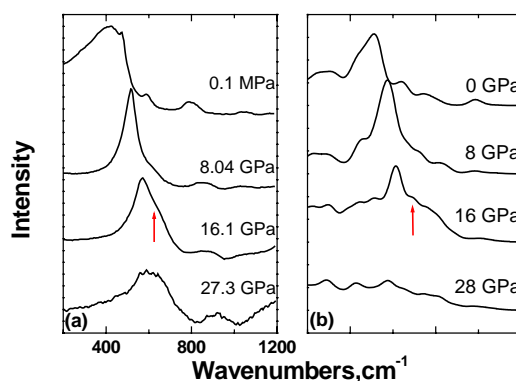

Fig.6.14 Calculate Raman spectra based on BP model (right) compared with experimental data (left) [217].
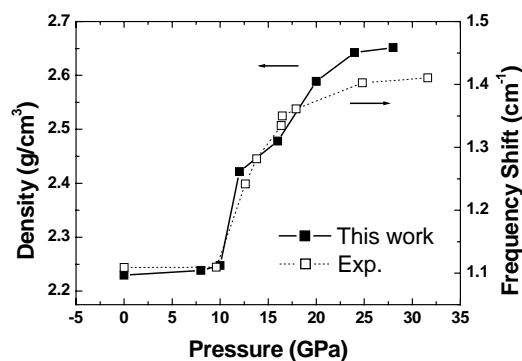
Fig.6.14 Density of the simulated densified glass as obtained by ambient temperature decompression from different pressures. Direct measurements of densities are not available on a wide pressure range, so comparison with Brillouin frequency shifts is shown, which are believed to be connected with density changes [19].

6.5 Conclusions

In summary, the TS potential can reproduce the features of the temperature-induced densification of compressed glass in the pressure range 0-10 GPa, where the glass is known to retain a tetrahedral structure. The annealed, densified form of glass corresponds to the thermodynamical minimum, within the realm of disordered phases, at all considered pressures. No abrupt changes in the properties of the annealed glass have been found, indicating that ideas of a possible polyamorphism, i.e. of a first-order transition between two distinct phases, may have to be revised for silica. The TS potential can reproduce the mechanical strength minimum and the onset of pressure-induced densification at 10 GPa and the bulk modulus minimum at 2-4 GPa. The compressibility maximum does not require changes of the tetrahedral network topology. The pressure induced appearance of unquenchable five-fold defects is responsible for the reduction of the mechanical strength and for permanent densification.

Chapter 7

Pressure-induced Amorphization of a Silica Clathrate

Melanophlogite, a low-pressure silica polymorph, has been extensively studied at different temperatures and pressures by molecular dynamics simulations. While the high-temperature form is confirmed as cubic, the low temperature phase is found to be slightly distorted, in agreement with experiments. With increasing pressure, the crystalline character is gradually lost, the topology changes and plastic behavior and permanent densification appears above ~12 GPa, triggered by Si coordination number changes.

7.1 Introduction

Melanophlogite is a rare mineral first described by Lasulx in 1876 [224], known from only five volcanic areas. The name melanophlogite describes the fact that mineral turns black when heated. Melanophlogite contains up to 8% C, H, O, N and S [225]. The role of these additional elements was not understood until Kamb concluded from X-Ray powder data that melanophlogite is isostructual with the cubic gas hydrates of type I (Fig.7.1) [226], in which there are two types of cage per unit cell: two pentagonal dodecahedra $[5^{12}]$ and 6 tetrakaidecahedra $[5^{12}6^2]$ cages with the guest molecules M^{12} (N_2, CH_4) and M^{14} (CO_2), respectively [225-227]. The guest molecules are
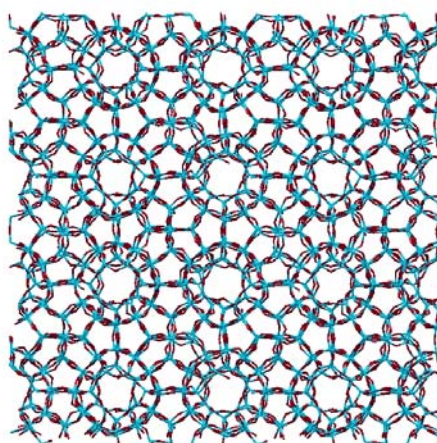

Fig. 7.1 A snapshot of the melanophlogite at 1000 K.

thought to act as templates during crystallization. Using a mixture of CO_2, CH_4 and N_2 as guest molecules, melanophlogite was first synthesized under hydrothermal conditions from aqueous silica solutions in 1982 [228]. Melanophlogite is known to distort slightly from cubic symmetry below around 80 ^{o}C [229-232]. By careful thermal treatment (e.g. heating to above 600 ^{o}C), the guest molecules can be removed [94,95,229,232-235]. While it is very interesting to investigate the guest molecules entrapped in the clathrates [236,237], and the interaction between guest and host framework [95], here we, as a first step, only focus on guest-free melanophlogite.

A crystalline-amorphous transition has been documented in melanophlogite very recently, primarily through a broadening and drop in intensity of the X-ray diffraction lines [94,95]. Amorphization in melanophlogite is observed at 8 GPa [94], much earlier than quartz and coesite, which is consistent with the fact that the starting crystal (melanophlogite) is already less dense than glass, and with similiar Gibbs free energy at 0GPa. In this chapter, we are going to study the atomic behavior during the amorphization.

7.2 Results and Discussions

We first present the results of simulations of the pressure-induced amorphiszation of guest-free melanophlogite. The simulations were carried out using the TS potential [29]. We started our molecular dynamics (MD) simulations from a cell consisting of 368 SiO_2 formula units ($2 \times 2 \times 2$ unit cells), which is obtained by first linearly inserting oxygen tatoms in the middle of two silicon atoms in Type I silicon clathrate and then relaxing the structure to 0 GPa and 0 K. The

MD time step was set to 0.72 fs (30 a.u.). We then studied the lattice and volume changes at different temperatures [Figs. 7.2 and 7.3]. It interesting to note that the volume is expanded very fast and then saturated at around 500 K, which is typical of α-β transition like in quartz and cristobalite [173]. Like quartz and cristobalite, melanophlogite shows the dynamic disorder of oxygen atoms above ~500K.. While the high-temperature form is found to be cubic, in agreement with experiments, the low temperature phase is found to be slightly distorted (Fig.7.3), which is also in agreement with experiments [229-232]. However, the experimental studies find the low temperature phase as tetragonal, whereas we find it with lower symmetry than tetragonal (see Fig. 7.3). Nevertheless, the distortion is small as mentioned by Yagi and others [95].
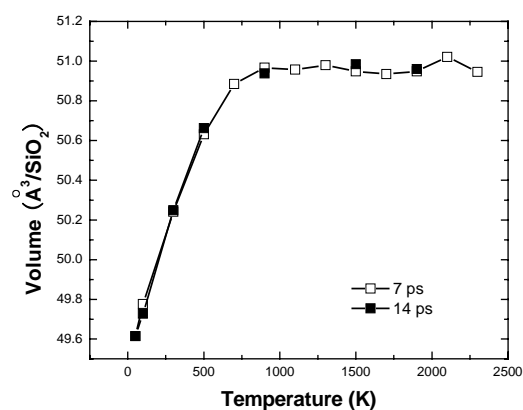
Fig.7.2 The volume as a function of temperature, initially 7 ps (open) is used and further 7 ps (solid) for checking convergence.
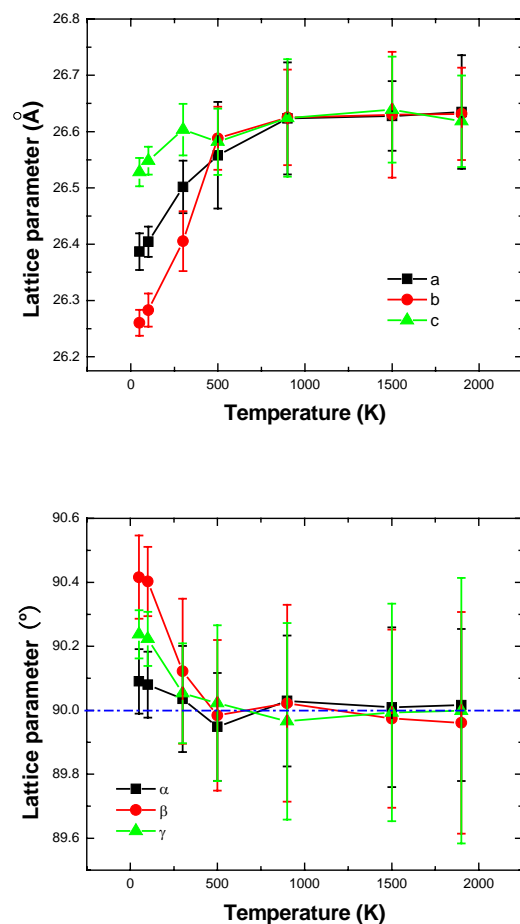

Fig. 7.3 Lattice parameter as a function of temperature obtained by taking the average of molecular dynamics trajectories.
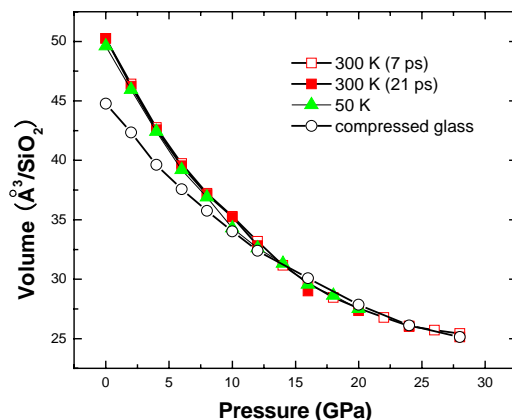
Fig.7.4 Equation of state of melanophlogite at 300 K, initial 7 ps (open square) and further 14 ps (solid square), at 50 K (triangle), and of cold compressed glass (circle) from Fig.6.8.
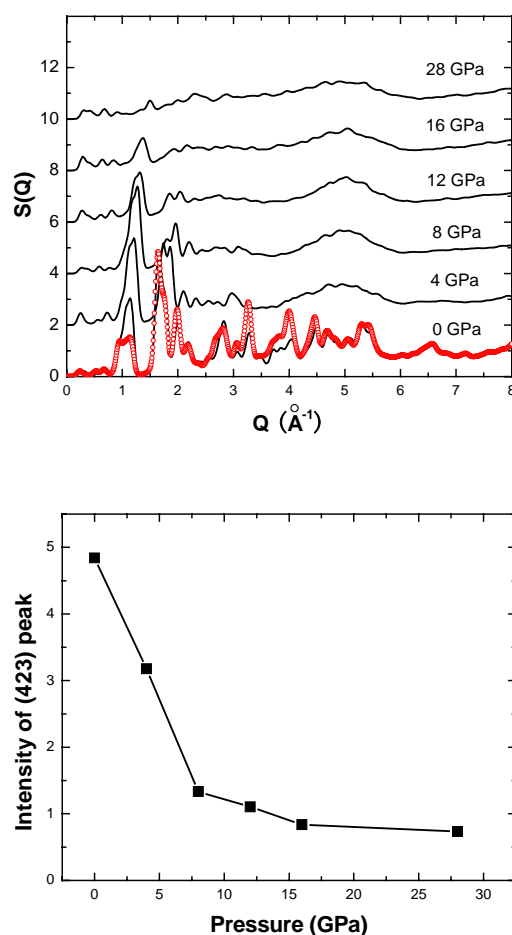

Fig. 7.5 Calculated X-ray structure factor at some selected pressures at 300 K (line) and 900 K (circle) (a) and the intensity of Bragg peak (423) varies at elevated pressure (b).
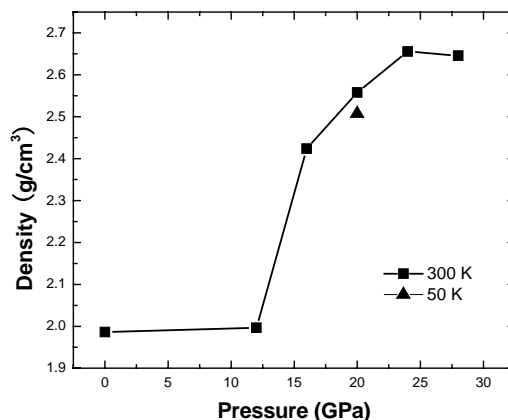
Fig.7.6 The density of the simulated densified glass (or a mixture with crystalline) at 0GPa as a function of subjected peak pressure.
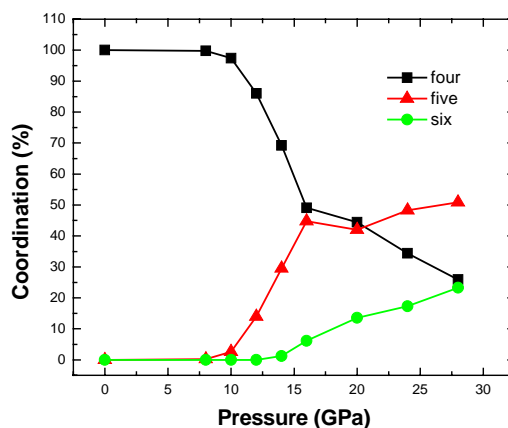

Fig.7.7 Percentages of Si atoms coordinated four (squares), five (circles), and six (triangles), to oxygen, at different pressures.
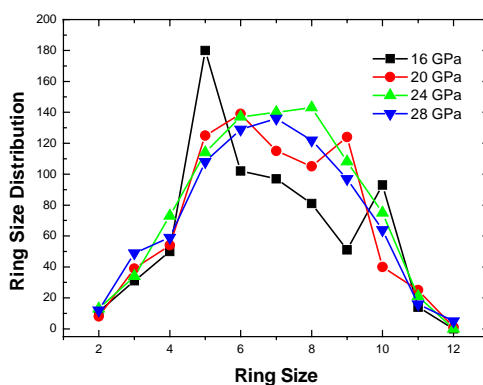

Fig. 7.8 The ring statistics of recovered sample from different subjected peak pressure.

Next, we applied a stepwise hydrostatic compression at 300 K and 50 K, with pressure

increments of 2 GPa, followed, at each pressure, by an equilibration time of 20 ps. No clear volume collapse can be identified in the equation of state, up to a pressure of 28 GPa (Fig. 7.4), with a negligible dependence on the compression rate. Melanophlogite has higher compressibility than glass in agreement with experiments [94,95], while the equation of states converge at pressures above 12 GPa. No first order transition has been found in the whole studied range. We compared the X-ray structure factor at different pressures in Fig. 7.5. At 0 GPa and room temperature, the diffraction pattern is consistent with the experimental data [94,95]. The relative intensity differs between different experimental reports. Our data show higher intensity in the second and third peaks (i.e. *[202]* and *[222]* on a basis of tetragonal unit cell [227]) than in Ref. [94], but similar to those of Ref. [95]. In any case, we agree with experiments on the fact that the strongest peak (423) and other peaks, shown in Fig.7.5(b), decrease in intensity with increasing pressure [94]. However, recovered sample only show densification above around 12 GPa (Fig.7.6), which suggest that the reduction of the Bragg peaks below 12 GPa is not a consequence of bonding changes. This is confrmed by the analysis of the coordination changes and ring statistics (Figs.7.7 and 7.8). The coordination increases only above ~12 GPa, and as a consequence, the topology changes to produce densified glass. In contrast, for pressures lower than 10-12 GPa, the compression takes place only through the reduction of Si-O-Si angles. At 10 GPa, the Si-O-Si ange is distributed around 120-124°, which pre-empts the Si coordination changes. The crystalline melanophlogite contains only 5-member, 6-member and 10-member rings. As can be seen in Fig. 7.8, the topology of recovered sample from 12 GPa has 2 five-member rings and 1 six-member ring less than the starting crystal. For the sample recovered from 16 GPa, the ring size distribution shows some memory of the crystal, with a maximum for 5-member rings and a second peak for 10-member rings. At high pressure, the densification process saturates and generates a ring statistics similar to that of densified glass. It is noteworthy that at higher subjected peak pressure the densification is saturated like normal glass behaves as shown in Chapter 6. We remark that the increase of small member ring with peak pressure is consistent with Raman experimental data [217].

7.3 Conclusions

To summarize, we have shown the TS potential can reproduce the experimentally reported transition from a low-temperature distorted structure to a high-temperature cubic structure in

melanophlogite. This is only one example for pure silica zeolite. The simulation on high-pressure melanphlogite doesn't show any first-order transition, but does show (gradual) amorphization and densification. The gradual changes, not collapse, make it possible to produce a glass less dense than normal glass ($2.22 g/cm^3$) [238].

Chapter 8

Conclusions and Perspectives

In this thesis, we have attempted to provide a comprehensive understanding of the phase transformations in silica polymorphs and glasses based on the microscopic analysis that emerges from molecular dynamics.

The simulations were carried out using an interatomic force field optimized by best fit on first-principles (density functional theory) calculations. The performance of the TS potential is very excellent when solving the problem listed in this thesis. We first calculated infrared and Raman spectra for quartz, cristobalite and stishovite and compared them with experiments, as well as with spectra obtained with other force fields, such as TTAM, BKS and an improved three-body potential. The reliability of the interaction potential in the calculation of IR and Raman spectra is validated by the excellent agreement with experimental data both in the peak positions and in the relative intensities. In particular, we were able to reproduce the relevant spectral changes mode in the α-β transition, which is generally considered to be highly non-harmonic. Our results suggest that the polarizable potential can be extended to the study of other temperature-induced transitions where the role of dynamical disorder and anharmonicities is predominant. The performance of the potential in octahedral structures was evaluated by calculating Raman spectra across the rutile-to-$CaCl_2$ transition at around 50GPa. The lowest frequency peak shows a softening behavior below ~50 GPa, which is consistent with experiments and other calculations. Regarding to Raman spectra by using direct approach (see Chapter 3), it is very challenging direction and certainly needs more efforts in future study.

Having established the reliability of the TS potential for the study of the very high-pressure phasesof silica, we have then turned our attention to the packing of oxygen in high-pressure silica phases. We have employed the pair analysis, a method widely used in the study of metals, for describing the geometry of the oxygen sublattice. We confirm that both cristobalite and quartz under high pressure can be described by oxygen bcc sublattice. The collapse of the tetrahedral

network in cristobalite (phase X-I) is concomitant with the collapse of the oxygen sublattice from a bcc-like to a close packed arrangement. We explain the large amount of conflicting experimental evidence regarding the dense phases of silica by invoking the important role of non hydrostatic stresses in driving the formation of different oxygen packing arrangements, including the appearance of the α-PbO$_2$-like phase which, so far, lacked a microscopic connection with the original cristobalite phase, and the suggestion that an anatase-like phase with a cubic close packed arrangement for the oxygen sublattice may be synthesized under appropriate stress conditions. We further presented a comprehensive understanding about the collapse of quartz under pressure. We argue that quartz-II is not a distinct phase, but simply a partial symmetrization of quartz. A pathway to transform from quartz to P2$_1$/c (Z=6) phase is well understood by following oxygen sublattice only. Pressure-induced bulk amorphization of quartz can also be understood based on oxygen packing arguments. We have also studied pressure-induced amorphization in a more complicated clathrate structures melanophlogite and found a gradual apparent amorphization before plastic deformation and densification.

The TS potential is shown to reproduce the features of the temperature-induced densification of compressed glass in the pressure range 0-10 GPa, where the glass is known to retain a tetrahedral structure. The annealed, densified form of glass corresponds to the thermodynamical minimum, within the realm of disordered phases, at all considered pressures. No abrupt changes in the properties of the annealed glass have been found. The TS potential can reproduce the mechanical strength minimum and the onset of pressure-induced densification at 10 GPa and the bulk modulus minimum at 2-4 GPa. The compressibility maximum does not require changes of the tetrahedral network topology. The pressure induced appearance of unquenchable five-fold defects is responsible for the reduction of the mechanical strength and for permanent densification. It is noteworthy that the intermediate phase between hp-cristobalite and α-PbO$_2$-like phase is 5-fold silicon crystalline phase. The concept of 5-fold silicon coordination in pure silica has only rarely been advocated so far, so our results call for an experimental confirmation.

We hope that our finding that a polarizable potential fitted to ab initio data can provide such a comprehensive picture of the silica phase diagram will stimulate further work towards the development of similar potentials for more complex systems, including silicates and other

minerals, as well as materials of practical interest such as zeolites and other nano- or meso-structureed silica-based materials.

Appendix

In Chapter 3, I've shown how to calculate infrared spectra based on the molecular dynamics by assuming the refractive index of the medium as a constant. However, in the most cases, the refractive index varies within the infrared frequency range. It's possible to treat explicitly refractive index by using Kramers-Kronig (KK) relationship.

A.1 The Formulations

By Fourier transforming the total polarization autocorrelation function, we are able to calculate the imaginary part $\varepsilon_2(\omega)$ of the dielectric constant in the classical limit [159]:

$$\varepsilon_2(\omega) = \frac{2\pi\omega}{3VK_BT} \int_0^\infty < \vec{M}(t) \cdot \vec{M}(0) > e^{-i\omega t} dt \tag{A.1}$$

where $\vec{M}$ is the total dipole moment, V is the volume of the sample, and K_B is Boltzmann's constant, respectively. The correlation functions in the above equations were obtained directly from our simulations and the use of KK relations [239-241] allow us to obtain the real part $\varepsilon_1(\omega)$ of the dielectric constant $\tilde{\varepsilon}(\omega)$ [242]:

$$\varepsilon_1(\omega) = \frac{2}{\pi} P \int_0^\infty \frac{\omega' \varepsilon_2(\omega)}{\omega'^2 - \omega^2} d\omega' + \varepsilon_\infty \tag{A.2}$$

where ε_∞ is the electric contribution. The complex refractive index $\tilde{n}$ and the complex dielectric function $\tilde{\varepsilon}$ by definition are following:

$$\tilde{n}(\omega) = n(\omega) + ik(\omega), \quad \tilde{\varepsilon}(\omega) = \varepsilon_1(\omega) + i\varepsilon_2(\omega) = \tilde{n}(\omega)^2 \tag{A.3}$$

The relationship between the optical functions and dielectric functions is thus as is obvious:

$$\varepsilon_1(\omega) = n(\omega)^2 - k(\omega)^2, \quad \varepsilon_2(\omega) = 2n(\omega)k(\omega) \tag{A.4}$$

Given an (infrared) wave propagation described by $\vec{E} = \vec{E}_0 \exp[i(\vec{q} \cdot \vec{r} - \omega t)]$, where $\vec{E}$ is the electric field strength, $\vec{q}$ is the wave vector, $\vec{r}$ is the space coordinate and t is the time; by using Maxwell's equation in dielectric material [239], the infrared absorption spectra $\alpha(\omega)$ can be obtained from the equation below

$$\alpha(\omega) = \frac{\omega \varepsilon_2(\omega)}{cn(\omega)} \tag{A.5}$$

We determine the reflectivity according to the equation

$$R(\omega) = \frac{(n(\omega)-1)^2 + k(\omega)^2}{(n(\omega)+1)^2 + k(\omega)^2} \tag{A.6}$$

In essence, our method involves calculating $\varepsilon_2(\omega)$ by the method described above with the MgO potential developed by Tangney and Scandolo [104], we then go on to determine the real part of the dielectric constant and finally using KK relations to obtain the optical functions and the absorption and reflection infrared spectra. With this approach, we are able to obtain results that agree with experimental results in MgO.

A.2 The Results on MgO

In Fig.A.1, we compare the optical properties from our simulations with the experiment results of Hofmeister and collaborators [243]. In Fig. A.1a, the peak in both the experiment and calculated dielectric functions occurred at the same point around 411 cm^{-1} although experiment has a wider base. We then use formula listed in Sec. A.1 to calculate the absorption and reflection infrared spectra shown in Fig. A. 1b. The overall agreement is very good, although the right shoulders of absorption and reflection reduces to zero earlier than experiments. A similar extent of agreement between experiment and theory are found in optical function in Fig.A.1c, we notice that the calculated static refractive index is underestimated and the width of the band is smaller than experiments.
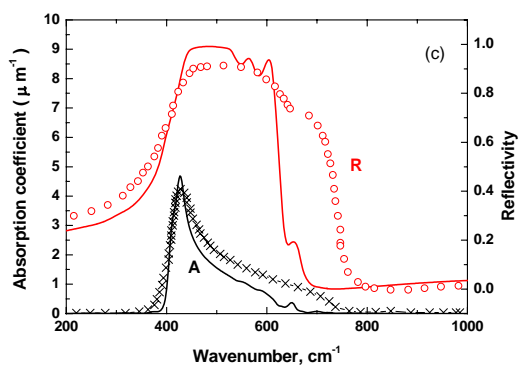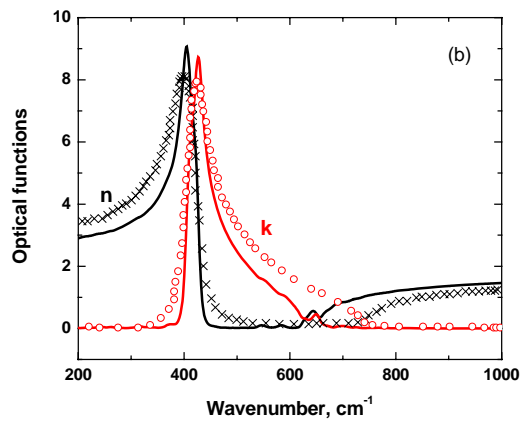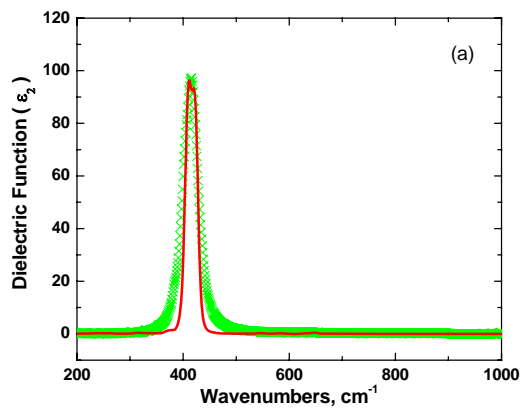
Fig.A.1 Calculated optical properties as compared with experiments. Solid lines are simulation results; scattered are from experiments [243].

Bibliography

[1] P. F. McMillan, Nature Materials **1**, 19 (2002).

[2] see e.g. H. K. Mao and R. J. Hemley, Rev. Mineral. **37**, 1 (1998).

[3] Y. Tsuchida and T. Yagi, Nature (London) **347**, 267 (1990).

[4] K. J. Kingma, R. J. Hemley, H. K. Mao, and D. R. Veblen, Phys. Rev. Lett. **70**, 3927(1993).

[5] L. S. Dubrovinsky et al., Chem. Phys. Lett. **333**, 264 (2001).

[6] N. A. Dubrovinskaia, L. S. Dubrovinsky, S. K. Saxena, F. Tutti, S. Rekhi   and T. Le Bihan, Eur. J. Mineral. **13**, 479 (2001).

[7] R. J. Hemley, A. P. Jephcoat, H. K. Mao, L. C. Ming and M. H. Manghnani, Nature (London) **334**, 52 (1988).

[8] O. Mishima, L. D. Calvert and E. Whalley, Nature (London) **310**, 393 (1984).

[9] P. Richet and P. Gillet, Eur. J. Mineral. **9**, 907 (1997).

[10] S. M. Sharma and S. K. Sikka, Progress in Materials Science **40**, 1 (1996).

[11] M. R. Vukcevich, J. Non-Cryst. Solids **11**, 25 (1972).

[12] K. I. Kondo, S. Lio, and A. Sawaoka, J. Appl. Phys. **52**, 2826 (1981).

[13] C. Meade and R. Jeanloz, Phys. Rev. B **35**, 236 (1987).

[14] C. S. Zha, R. J. Hemley, H. K. Mao, T. S. Duffy, and C. Meade, Phys. Rev. B **50**, 13105 (1994).

[15] O. B. Tsiok, V. V. Brazhkin, A. G. Lyapin, and L. G. Khvostantsev, Phys. Rev. Lett. **80**, 999 (1998).

[16] C. Meade and R. Jeanloz, Science **241**, 1072 (1988).

[17] P. W. Bridgman and I. Simon, J. Appl. Phys. **24**, 405 (1953).

[18] M. Grimsditch, Phys. Rev. Lett. **52**, 2379 (1984); Phys. Rev. B **34**, 4372 (1986).

[19] A. Polian and M. Grimsditch, Phys. Rev. B **41**, 6086 (1990).

[20] S. Susman, K. J. Volin, D. L. Price, M. Grimsditch, J. P. Rino, R. K. Kalia, P. Vashishta, G. Gwanmesia, Y. Wang, and R. C. Liebermann, Phys. Rev. B **43**, 1194 (1991).

[21] S. Sugai and A. Onodera, Phys. Rev. Lett. **77**, 4210 (1996).

[22] Y. Inamura, Y. Katayama, W. Utsumi and K. Funakoshi, Phys. Rev. Lett. **93**, 015501 (2004).

[23] R. Roy and H. M. Cohen, Nature (London) **190** 798 (1961).

[24] H. M. Cohen and R. Roy, Phys. Chem. Glasses **6** 149 (1965).

[25] K. Trachenko, M. T. Dove, V. Brazhkin, and F. S. El'kin, Phys. Rev. Lett. **93**, 135502 (2004).

[26] G. D. Mukherjee, S. N. Vaidya, and V. Sugandhi, Phys. Rev. Lett. **87**, 195501 (2001).

[27] F. S. El'kin, V. V. Brazhkin, L. G. Khvostantsev, O. B. Tsiok, and A. G. Lyapin, JETP Lett. **75**, 342 (2002).

[28] F. Ercolessi and J. B. Adams, Europhys. Lett. 26, 583 (1994).

[29] P. Tangney and S. Scandolo, J. Chem. Phys. **117**, 8898 (2002).

[30] A. El Goresy, L. S. Dubrovinsky, T. G. Sharp, S. K. Saxena and M. Chen, Science **288**,1632 (2000).

[31] S. K. Saxena et al., Science **274**,1357 (1996).

[32] S. K. Saxena, L. S. Dubrovinsky, P. Lazor and J. Hu, Eur. J. Mineral. **10**, 1275 (1998).

[33] T. G. Sharp, A. El Goresy, B. Wopenka and M. Chen, Science **284**, 1511(1999).

[34] P. Dera, C. T. Prewitt, N. Z. Boctor and R. J. Hemley, Am. Miner. **87**, 1018 (2002).

[35] L. W. Hobbs, C. E. Jesurum and B. Berger, in "*Structure and imperfections in amorphous and crystalline silicon dioxide*", edited by R. A. B. Devine, J. P. Duraud and E. Dooryhee, pp.3-, (John Wiley & Sons, 2000).

[36] R. J. Hemley, J. Badro and D. M. Teter, in "*Physics meets Mineralogy*", edited by H. Aoki, Y. Syono and R. J. Hemley, pp. 173-, (Cambridge, 2000).

[37] R. J. Hemley, C. T. Prewitt, and K. J. Kingma, in "*Silica: Physical Behavior, Geochemistry and Materials Application"s*, edited by P. J. Heaney, C. T. Prewitt, and G. V. Gibbs Vol. 29, p. 41- (Mineralogical Society of America, Washington, D.C., 1994).

[38] K. J. Kingma, C. Meade, R. J. Hemley, H. K. Mao, and D. R. Veblen, Science **259**, 569 (1993).

[39] J. Haines, J. M. Léger, F. Gorelli, and M. Hanfland, Phys. Rev. Lett. **87**, 155503 (2001).

[40] Y. Kuwayama, K. Hirose, N. Sata, and Y. Ohishi, Science **309**, 923 (2005).

[41] P. Umari, X. Gonze, and A. Pasquarello, Phys. Rev. Lett. **90**, 027401 (2003).

[42] P. Umari, A. Pasquarello, and A. Dal Corso, Phys. Rev. B **63**, 094305 (2001)

[43] K. J. Kingma, R. E. Cohen, R. J. Hemley and H. K. Mao, Nature (London) **374**, 243 (1995).

[44] D. Andrault, G. Fiquet, F. Guyot, and M. Hanfland, Science, **282**, 720 (1998).

[45] S. M. Stishov and S. V. Popova, Geochemistry **10**, 923 (1961).

[46] L. S. Dubrovinsky, S. K. Saxena, P. Lazor, R. Ahuja, O. Eriksson, J. M. Wills, and B. Johansson, Nature (London) **388**, 362 (1997).

[47] K. S. Finnie, J. G. Thompson, and R. L. Withers, J. Phys. Chem. Solids **55**, 23 (1994).

[48] P. Gillet, A. Le Cleach, and M. Madon, J. Geophys. Res. **95**, 21635 (1990).

[49] J. Bates, J. Chem. Phys. **57**, 4042 (1972).

[50] I. P. Swainson, M. T. Dove, and D. C. Palmer, Phys. Chem. Minerals **30**, 353 (2003).

[51] S. R. Shieh,T. S. Duffy and G. Shen, Earth Planet. Sci. Lett. **235**, 273 (2005).

[52] M. Murakami,K. Hirose, S. Ono and Y. Ohishi, Geophys. Res. Lett. **30**, 1207 (2003).

[53] B. B. Karki, M. C. Warren, L. Stixrude, G. J. Ackland and J. Crain, Phys. Rev. B **55**, 3465 (1997); **56, 2884 (1997)**.

[54] D. M. Teter, R. J. Hemley, G. Kresse, and J. Hafner, Phys. Rev. Lett. **80**, 2145 (1998).

[55] T. Tsuchiya, R. Caracas and J. Tsuchiya, Geophys. Res. Lett. **31**, L11610 (2004).

[56] A. R. Oganov, M. J. Gillan and G. D. Price, Phys. Rev. B **71**, 064104 (2005).

[57] L. S. Dubrovinsky et al., Phys. of the Earth and Planetary Interiors **143**, 231(2004).

[58] V. B. Prokopenko, L. S. Dubrovinsky,V. Dmitriev and H. P. Weber, J. Alloys and Compounds **327**, 87 (2001).

[59] V. B. Prakapenka, G. Shen, M. Rivers, S. Sutton and L. Dubrovinsky, J. Phys. Chem. Solids **65**, 1537 (2004).

[60] L. S. Dubrovinsky et al., High Press. Res. 23, 35 (2003).

[61] D. D. Klug, R. Rousseau, K. Uehara, M. Bernasconi,Y. Le Page and J. S. Tse, Phys. Rev. B **63**, 104106 (2001).

[62] L. P. Huang, M. Durandurdu and J. Kieffer, Nature Materials **5**, 977 (2006).

[63] S. Tsuneyuki,Y. Matsui,H. Aoki and M. Tsukada, Nature (London) **339**, 209 (1989).

[64] J. S. Tse and D. D. Klug, J. Chem. Phys. 95, 9176(1991).

[65] L. Stixrude and M. S. T. Bukowinski, Phys. Rev. B **44**, 2523 (1991).

[66] C. Meade, R. J. Hemley, and H. K. Mao, Phys. Rev. Lett. **69**, 1387 (1992).

[67] A. Trave, P. Tangney, S. Scandolo, A. Pasquarello, and R. Car, Phys. Rev. Lett. **89**, 245504 (2002).

[68] K. H. Smith, E. Shero, A. Chizmeshya, and G. H. Wolf, J. Chem. Phys. **102**, 6851 (1995).

[69] D. J. Lacks, Phys. Rev. Lett. **84**, 4629 (2000).

[70] M. J. Aziz, S. Circone, and C. B. Agee, Nature (London) **390**, 596 (1997).

[71] R. G. Della Valle and E. Venuti, Phys. Rev. B **54**, 3809 (1996).

[72] K. Trachenko and M. T. Dove, J. Phys.: Condens. Matter **14**, 7449 (2002).

[73] L. V. Woodcock, C. A. Angell, and P. Cheeseman, J. Chem. Phys. **65**, 1565 (1976)

[74] J. S. Tse, D. D. Klug, and Y. Le Page, Phys. Rev. B **46**, 5933 (1992).

[75] G. E. Walrafen and P. N. Krishnan, J. Chem. Phys. **74**, 5328 (1981); P. Mcmillan, B. Piriou, and R. Couty, ibid. **81**, 4234 (1984).

[76] C. A. Angell, P. A. Cheeseman, and S. Tamaddon, Science **218**, 885 (1982).

[77] S. Tsuneyuki and Y. Matsui, Phys. Rev. Lett. **74**, 3197 (1995).

[78] F. Wooten, K. Winer, and D. Weaire, Phys. Rev. Lett. **54**, 1392 (1985).

[79] K. Vollmayr, W. Kob, and K. Binder, Phys. Rev. B **54**, 15808 (1996).

[80] D. C. Palmer and L. W. Finger, Am. Miner. **79**, 1 (1994).

[81] R. T. Downs and D. C. Palmer, Am. Miner. **79**, 9 (1994).

[82] A. Onodera, et al., High Pressure Res. **15**, 307 (1997).

[83] M. T. Dove et al., Miner. Mag. **64**, 569 (2000).

[84] Y. Yahagi, T. Yagi, H. Yamawaki and K. Aoki, Solid State Communications. **89**, 945 (1994).

[85] D. C. Palmer, R. J. Hemley and C. T. Prewitt, Phys. Chem. Minerals. **21**, 481 (1994).

[86] K. D. Hammonds et al., Am. Miner. **81**, 1057 (1996).

[87] A. J. Gratz, L. D. DeLoach, T. M. Clough, and W. J. Nellis, Science **259**, 663 (1993).

[88] S.L. Chaplot and S.K. Sikka, Phys. Rev. B **47**, 5710 (1993).

[89] G.W. Watson and S. C. Parker, Phys. Rev. B **52**, 13306(1995)

[90] J.S. Tse and D.D. Klug, Phys. Rev. Lett. **67**, 3559(1991).

[91] N. Binggeli and J.R. Chelikowsky, Phys. Rev. Lett. **69**, 2220 (1992).

[92] K. J. Kingma et al., High Press. Res. 14, 363 (1996).

[93] J.S. Tse, D. D. Klug, J. A. Ripmeester, S. Desgreniers, and K. Lagerec, Nature (London) **369**, 724 (1994).

[94] H. W. Xu, J. Z. Zhang, Y. S. Zhao, G. D. Guthrie, D. D. Hickmott and A. Navrotsky, Am. Miner. **92**, 166 (2007).

[95] T. Yagi, E. Iida, H. Hirai, N. Miyajima, T. Kikegawa and M. Bunno, Phys. Rev. B **75**, 174115 (2007).

[96] T. Yagi and M. Yamakata, in "*Physics meets Mineralogy*", edited by Aoki, H., Syono, Y., & Hemley, R.J., pp. 242-, (Cambridge, 2000); M. Yamakata and T. Yagi, Proc. Japan Acad. B **73**, 85(1997).

[97] P. Gillet, R. J. Hemley and P. F. McMillan, Rev. Miner. Geochem. **37**, 525 (1998).

[98] R. Car and M. Parrinello, Phys. Rev. Lett. **55**, 2471 (1985).

[99] W. Kohn, Rev. Mod. Phys. **71**, 1253 (1999); W. Kohn and L. J. Sham, Phys. Rev. **140**, A1133 (1965); P. Hohenberg and W. Kohn, Phys. Rev. 136, B864 (1964); W. Kohn and L. J. Sham, Phys. Rev. **137**, A1697 (1965).

[100] P. Focher, Ph. D. Thesis, SISSA, Trieste (1994); A. Trave, Ph.D. Thesis, University of Geneva (2001).

[101] A. Laio, S. Bernard, G. L. Chiarotti, S. Scandolo, and E. Tosatti, Science **287**, 1027 (2000).

[102] A. Laio, Ph. D. Thesis, SISSA, Trieste (1999).

[103] P. Tangney, Ph. D. Thesis, SISSA, Trieste (2002).

[104] P. Tangney and S. Scandolo, J. Chem. Phys. **119**, 9673 (2003).

[105] M. Wilson, P. A. Madden, N. C. Pyper, and J. H. Harding, J. Chem. Phys. **104**, 8068 (1996).

[106] A. Rowley, P. Jemmer, M. Wilson, and P. A. Madden, J. Chem. Phys.**108**, 10209 (1998).

[107] A. Aguado, L. Bernasconi, and P. A. Madden, Chem. Phys. Lett. **356**, 437 (2002).

[108] A. Aguado, L. Bernasconi, and P. A. Madden, J. Chem. Phys. **118**, 5704 (2003).

[109] A. Aguado and P. A. Madden, J. Chem. Phys. **118**, 5718 (2003).

[110] A. Aguado, L. Bernasconi, S. Jahn, and P. A. Madden, Faraday Discuss. **124**, 171 (2003).

[111] A. Aguado and P. A. Madden, J. Chem. Phys. **119**, 7471 (2003).

[112] A. Aguado and P. A. Madden, Phys. Rev. B **70**, 245103 (2004).

[113] S. Jahn, P. A. Madden and M. Wilson, Phys. Rev. B 74, 024112 (2006)

[114] S. Jahn and P. A. Madden, Phys. of the Earth and Planetary Interiors, **162**, 129 (2007).

[115] L. P. Huang and J. Kieffer, J. Chem. Phys. **118**, 1487 (2003).

[116] E. Demiralp, T. Cagin, and William A. Goddard III, Phys. Rev. Lett. **82**, 1708 (1999).

[117] F. Zipoli, T. Laino, A. Laio, M. Bernasconi and M. Parrinello, J. Chem. Phys. **124**, 154707 (2006).

[118] D. Herzbach, K. Binder and M. H. Muser, J. Chem. Phys. **123**, 124711(2005); D. Herzbach, Ph.D. thesis, Mainz (2004).

[119] S. Kirkpatrick, C. D. Gelatt and M. P. Vecchi, Science **220**, 671 (1983).

[120] W. H. Press, B. P. Flannery, W. T. Vetterling and S. A. Teukolsky, "*Numerical Recipes in FORTRAN: The Art of Scientific and parral computing, 2nd Ed.*", (Cambridge, 1996).

[121] M. Born and J. E. Mayer, Z. Phys. **75**, 1 (1932).

[122] D. Frenkel and B. Smit, "*Understanding Molecular Simulation*". Academic Press (2001).

[123] W. Wang and R. D. Skeel, J. Chem. Phys. 123, 164107(2005).

[124] R. Chelli, A. Barducci, L. Bellucci, V. Schettino, and P. Procacci, J. Chem. Phys. 123, 194109 (2005).

[125] P. Vashishta et al. Phys. Rev. B **41**, 12197(1990).

[126] S. Tsuneyuki, M. Tsukada, A.Aoki, and Y. Matsui, Phys. Rev. Lett. **61**, 869(1988).

[127] B. W. H van Beest, G. J. Kramer, and R. A. van Santen, Phys. Rev. Lett. **64**, 1955(1990).

[128] M. Wilson, P. A. Madden, M. Hemmati, and C. A. Angell, Phys. Rev. Lett. **77**, 4023 (1996).

[129] D. Herzbach, K. Binder and M. H. Muser, J. Chem. Phys. **123**, 124711(2005).

[130] L. Stixrude, in "*Structure and imperfections in amorphous and crystalline silicon dioxide*", edited by R. A. B. Devine, J. P. Duraud and E. Dooryhee, pp.69-, (John Wiley & Sons, 2000).

[131] T. Demuth, Y. Jeanvoine, J. Hafner, and J. G. Ángyán, J. Phys.: Condens. Matter **11**, 3833

(1999).

[132] D. R. Hamann, Phys. Rev. Lett. **76**, 660 (1996).

[133] See, e.g. H. B. Yu and W. F. Van Gunsteren, Comp. Phys. Comm. **172**, 69 (2005).

[134] M. Parrinello and A. Rahman, Phys. Rev. Lett. **45**, 1196 (1980).

[135] M. Parrinello and A. Rahman, J. Chem. Phys. **76**, 2662 (1982).

[136] M. Parrinello in "*Molecular Dynamics Simulation of Statistical-Mechanical Systems*", edited by G. Ciccotti and W. G. Hoover pp. 204- (North Holland, 1986).

[137] M. Parrinello and A. Rahamn, J. Appl. Phys. **52**, 7182 (1981).

[138] See, e.g., M. F. Horstemeyer, M. I. Baskes, and S. J. Plimpton, Acta Mater. 49, 4363 (2001).

[139] K. Trachenko and M. T. Dove, Phys. Rev. B 67 064107 (2003).

[140] S. Susman, K. J. Volin, D. G. Montague and D. L. Price, Phys. Rev. B 43 11076(1991).

[141] W. Jin, R. K. Kalia, P. Vashishta, and J. P. Rino, Phys. Rev. Lett. 71, 3146 (1993),

[142] W. Jin, R. K. Kalia, P. Vashishta, and J. P. Rino, Phys. Rev. B 50, 118 (1994).

[143] L. Huang and J. Kieffer, Phys. Rev. B **69**, 224203 (2004).

[144] L. Huang and J. Kieffer, Phys. Rev. B **69**, 224204 (2004).

[145] L. P. Davila, M. J. Caturla, A. Kubota, B. Sadigh, T. Diaz de la Rubia, J. F. Shackelford, S. H. Risbud, and S. H. Garofalini, Phys. Rev. Lett. **91**, 205501 (2003).

[146] J. Horbach and W. Kob, Phys. Rev. B **60**, 3169 (1999).

[147] M. P. Allen and D. J. Tildesley, Computer Simulation of Liquids (Oxford: Clarendon, 1987).

[148] J. M. Holender and G. J. Morgan, J. Phys.: Condense. Matter **3,** 1947 (1991).

[149] A. C. Wright, J. Non-Cryst. Solids **179,** 84 (1994).

[150] The theoretical x-ray intensity patterns were evaluated using the atomic scattering factors from the International Tables of X-Ray Crystallography pp. 202-, (Kynoch Press, Birmingham, 1962). Available in the Internet: http://www.isis.rl.ac.uk/ISISPublic/reference/Xray_scatfac.htm.

[151] C. S. Marians and L. W. Hobbs, J. Non-Cryst. Solids **106** 309 (1988).

[152] A. Pasquarello and R. Car, Phys. Rev. Lett. **79**, 1766 (1997).

[153] M. Lazzeri and F. Mauri, Phys. Rev. Lett. **90**, 036401 (2003).

[154] P. F. Mcmillan, B.T. Poe, P. Gillet and B. Reynard, Geochimica et Cosmochimica Acta, **58**, 3653 (1994); P. Gillet, Phys. Chem. Minerals, **23**, 263-275.

[155] A. G. Kalampounias, S. N. Yannopoulos, and G. N. Papatheodorou, J. Chem. Phys. **124**, 014504 (2006).

[156] Y. Q. Wu, G. C. Jiang, J. L. You, H. Y. Hou, H. Chen, and K. D. Xu, J. Chem. Phys. **121**, 7883 (2004).

[157] B. J. Berne and R. Pecora, "*Dynamic Light Scattering*" (John Wiley& Sons, Inc., New York, 1976).

[158] A. Putrino and M. Parrinello, Phys. Rev. Lett. **88**, 176401 (2002).

[159] M. Sharma, R. Resta and R. Car, Phys. Rev. Lett. **95**, 187401 (2005); M. Bernasconi, P. L. Silvestrelli, and M. Parrinello, ibid. **81**, 1235 (1998); P. L. Silvestrelli et al., Chem. Phys. Lett. **277**, 478 (1997); A. Debernardi et al., Appl. Phys. Lett. **71**, 2692 (1997).

[160] R. Guido, D. Valle, and H. C. Anderson, J. Chem. Phys. **94**, 5056 (1991).

[161] D. Herzbach and M. H. Muser, Comp. Phys. Comm. **174**, 17 (2006).

[162] K. J. Kingma and R. J. Hemley, Am. Miner. **79**, 269(1994).

[163] J. Etchepare, M. Merin and L. Smetankine, J. Chem. Phys. **60**, 1873(1974).

[164] P. F. McMillan and A. C. Hess, Phys. Chem. Minerals **17**, 97(1990).

[164] F. Gervais and B. Pirious, Phys. Rev. B **11**, 3944 (1975).

[165] A. Rahmani, M. Benoit and C. Benoit, Phys. Rev. B **68**, 184202(2003).

[166] R. W. G. Wychoff, Crystal structures Second edition, Vol. 1 (Malabar, Florida, 1982). One useful website is: http://cst-www.nrl.navy.mil/lattice/

[167] M. Ocana, V. Fornes, J. V. Garcia-Ramos and C. J. Serna, Phys. Chem. Minerals **14**, 527 (1987).

[168] P. J. Heaney, Rev. Mineral. **29**, 1 (1994).

[169] A. M. Hofmeister, J. Xu and S. Akimoto, Am. Mineral. **75**, 951 (1990).

[170] Handbook of Minerals Raman Spectra, http://www.ens-lyon.fr/LST/Raman

[171] M. H. Muser and K.Binder, Phys. Chem. Minerals **28**, 746 (2001).

[172] M. G. Tucker, M. T. Dove, and D. A. Keen, J. Phys.: Condens. Matter **12**, L723(2000).

[173] L. P. Huang and J. Kieffer, Phys. Rev. Lett. **95**, 215901 (2005).

[174] S. Tsuneyuki, H. Aoki, M. Tsukada and Y. Matsui, Phys. Rev. Lett. **64**, 776(1990).

[175] F. Liu, S. H. Garofalini, R. D. King-Smith, and D. Vanderbilt, Phys. Rev. Lett. **70**, 2750 (1993).

[176] I. P. Swainson and M. T. Dove, Phys. Rev. Lett. **71**, 193(1993).

[177] M. B. Smirnov and A. P. Mirgorodsky, Phys. Rev. Lett. **78**, 2413(1997).

[178] H. Kimizuka, H. Kaburaki, and Y. Kogure, Phys. Rev. Lett. **84**, 5548(2000).

[179] R. J. Hemley, in "*High-Pressure Research in Mineral Physics*", edited by M. H. Manghani and Y. Syono, pp. 347-, AGU, Washington, D. C. (1987).

[180] R. J. Hemley et al., Solid State Comm. **114**, 527 (2000).

[181] C. Lee and X. Gonze, J. Phys.: Condens. Matter **7**, 3693(1995); Phys. Rev. B **56**, 7321(1997).

[182] M. O'Keefe, Acta Cryst. A **33**,924 (1977).

[183] H. Sowa, Z. Kristall. **184**, 257 (1988).

[184] R. M. Hazen, L. W. Finger, R. J. Hemley, and H. K. Mao, Solid State Comm., **72**, 507 (1989).

[185] N. Binggeli and J. R. Chelikowsky, Nature (London) **353**, 344 (1991).

[186] H. Aoki, in "*Physics meets Mineralogy*", edited by H. Aoki, Y. Syono and R. J. Hemley, pp. 259-, (Cambridge, 2000).

[187] E. Blaisten-Barojas, Kinam. **6A**, 71 (1984).

[188] J. D. Honeycutt and H. C. Andersen, J. Phys. Chem. **91**, 4950 (1987).

[189] S. F. Tsay and S. Wang, Phys. Rev. B **50**, 108 (1994);

[190] C. S. Liu, Z. G. Zhu, J. Xia, and D. Y. Sun, J. Phys.: Condens. Matter **13**, 1873 (2001).

[191] C. S. Liu, J. Xia, Z. G. Zhu, and D. Y. Sun, J. Chem. Phys. **114**, 7506 (2001).

[192] G. X. Li, Y. F. Liang, Z. G. Zhu and C. S. Liu, J. Phys.: Condens. Matter **15**, 2259 (2003).

[193] C. Zener, Phys. Rev. **71**, 846 (1947).

[194] F. Milstein and D. J. Rasky, Phys. Rev. B **54**, 7016 (1996).

[195] E. C. Bain, Trans. AIME **70**, 25 (1924).

[196] W. G. Burgers, Physica **1**, 561 (1934).

[197] determined by using KPLOT, see, for example, R. Hundt, et al., J. Appl. Cryst. **32**, 413 (1999).

[198] J. Badro, J.L. Barrat, and P. Gillet, Europhys. Lett. **42**, 643 (1998)

[199] M.S. Somayazulu, S.M. Sharma, N. Garg, S.L. Chaplot, S.K. Sikka, J. Phys.: Condens. Matter **5**, 6345 (1993); M.S. Somayazulu, S.M. Sharma, S.K. Sikka, Phys. Rev. Lett. **73**, 98 (1994).

[200] C. Campana, Martin H. Muser, J. S. Tse, D. Herzbach, and P. Schoffel, Phys. Rev. B **70**, 224101 (2004); J. S. Tse, D. D. Klug, Y. Le Page, and M. Bernasconi, Phys. Rev. B **56**, 10878 (1997).

[201] J. Badro, J.-L. Barrat, and P. Gillet, Phys. Rev. Lett. **76**, 772 (1996); J. Badro, D. M. Teter, R. T. Downs, P. Gillet, R. J. Hemley, and J.-L. Barrat, Phys. Rev. B **56**, 5797 (1997).

[202] R. M. Wentzcovitch, C. da Silva, J. R. Chelikowsky, and N. Bingelli, Phys. Rev. Lett. **80**, 2149 (1998).

[203] N. Choudhury and S. L. Chaplot, Phys. Rev. B **73**, 094304 (2006).

[204] A. Trave, S. Scandolo, A. Pasquarello and R. Car, (unpublished). The simulations were

performed with the Car-Parrinello method [98] on a sample of 24 SiO_2 formula units, starting from a fully equilibrated α-quartz at ambient conditions. The stress was controlled using the variable-cell algorithm [137]. Thermostats were used to control atomic as well as cell variables [205]. A generalized gradient approximation to density functional theory was employed [206], together with ultrasoft pseudopotentials [207], to describe the electronic states, which were expanded in plane waves (26 Ry energy cut-off) and assumed to have the periodicity of the simulation cell.

[205] S. Nose, Mol. Phys. 52, 255 (1984); G. J. Martyna, M. L. Klein, and M. Tuckerman, J. Chem. Phys. **97**, 2635 (1992).

[206] J.P. Perdew et al., Phys. Rev. B 46, 6671 (1992).

[207] D. Vanderbilt, Phys. Rev. B 41, 7892 (1990); A. Pasquarello, K. Laasonen, R. Car, C.Lee, and D. Vanderbilt, Phys. Rev. Lett. 69, 1982 (1992); K. Laasonen, A. Pasquarello,R. Car, C. Lee, and D. Vanderbilt, Phys. Rev. B 47, 10142 (1993).

[208] L. Levien, C. T. Prewitt and D. J. Weidner, Am. Miner. **65**, 920 (1980).

[209] The inset of Fig. 5.3 is done at room temperature. The analysis on the relaxed sample yields a quasi bcc oxygen sublattice at 2 GPa.

[210] R. Martonak, D. Donadio, A. R. Oganov, and M. Parrinello, Nature Materials **5**, 623 (2006).

[211] S. Baroni, S. de Gironcoli, A. Dal Corso and P. Giannozzi Rev. Mod. Phys. 73, 515 (2001); S. Baroni, A. Dal Corso, S. de Gironcoli, and P. Giannozzi, http://www.pwscf.org

[212] O. Mishima, L. D. Calvert and E. Whalley, Nature (London) **314** 76 (1985).

[213] R. Martonak, D. Donadio, and M. Parrinello, Phys. Rev. Lett. **92**, 225702 (2004).

[214] R. Martonak, D. Donadio, and M. Parrinello, J. Chem. Phys. **122**, 134501 (2005).

[215] S. R. Elliot, Nature (London) **354**, 445 (1991).

[216] Y. Inamura, et al., Physica B **241,** 903 (1998).

[217] R. J. Hemley, H. K. Mao, P. M. Bell, and B. O. Mysen, Phys. Rev. Lett. **57**, 747 (1986).

[218] Q. Williams and R. Jeanloz, Science **239**, 902 (1988).

[219] E. M. Stolper and T. J. Ahrens, Geophys. Res. Lett. **14**, 1231 (1987); R. Jeanloz, Nature (London) **332**, 207 (1988).

[220] X. Y. Xue, J. F. Stebbins, K. Masami, P. F. Mcmillan, and B. Poe, Am. Mineral. **76**, 8 (1991).

[221] N. S. O. Ekunwe and D. J. Lacks, Phys. Rev. B **66**, 212101 (2002).

[222] C. H. Polsky, K. H. Smith, and G. H. Wolf, J. Non-Cryst. Solids **248**, 159 (1999).

[223] M. Guthrie, C. A. Tulk, C. J. Benmore, J. Xu, J. L. Yarger, D. D. Klug, J. S. Tse, H.-K. Mao, and R. J. Hemley, Phys. Rev. Lett. **93**, 115502 (2004).

[224] A. L. Lasaulx, N. Jb. Miner. **1876**, 250 (1876).

[225] B. J. Skinner and D. E. Appleman, Am. Miner. **48**, 854 (1963).

[226] B. Kamb, Science **148**, 232 (1965).

[227] L. Žák, Am. Miner. **57**, 779(1972).

[228] H. Gies, H. Gerke and F. Liebau, Neues Jahrbuch für Mineralogie Monatshefte **3**, 119 (1982).

[229] H. Gies, Z. Kristallogr. **164**, 247 (1983).

[230] C. A. Fyfe and H. Gies, J. Inclusion Phenom. Mol. Recognit. Chem. **8**, 235 (1990).

[231] S. X. Liu, M. D. Welch and J. Klinowski, J. Phys. Chem. B **101**, 2811 (1997).

[232] T. Nakagawa, K. Kihara and K. Harada, Am. Miner. **86**, 1506 (2001).

[233] A. Navrotsky, H. W. Xu, E. C. Moloy and M. D. Welch, Am. Miner. **88**, 1612 (2003).

[234] T. Nakagawa, K. Kihara and S. Fujinami, J. Miner. & Petro. Sci. **100**, 247 (2005).

[235] T. Nakagawa and K. Kihara, J. Miner. & Petro. Sci. **101**, 14 (2006).

[236] B. A. Kolesov and C. A. Geiger, Am. Miner. **88**, 1364 (2003).

[237] J. Kortus, G. Irmer, J. Monecke and M. R. Pederson, Modelling Simul. Mater. Sci. Eng. **8**, 403 (2000).

[238] G. N. Greeves, F. Menau, A. Sapelkin, L. M. Colyer, I. Ap Gwynn, S. Wade and G. Sanker, Nature Materials **2**, 622 (2003).

[239] F. Wooten, "*Optical Properties of Solids*", Academic Press, Inc. New York (1972).

[240] R. de L. Kronig, J. Opt. Soc. Am. 12, 547 (1926).

[241] H.A. Kramers, in Atti del Congresso Internazionale dei Fisica, Vol.2, Zanichelli, Bologna (1927)

[242] V. Lucarini, J.J. Saarinen, K.-E. Peiponen and E.M. Vartiainen, "*Kramers-Kronig Relations in Optical Materials Research*", Springer-Verlag, (2005).

[243] A.M. Hofmeister, E. Keppel and A.K. Speck, Mon. Not. R. Astron. Sci. **345**, 16 (2003).